RCA Review

A technical journal published quarterly
by RCA Research and Engineering
in cooperation with the subsidiaries
and divisions of RCA.

Contents

185 Analysis of Transport Processes During Holographic Recording in Insulators
Juan J. Amodei

199 System Aspects of Electrophotographic Materials and Processing for Liquid Reversal Toning
E. C. Giaimo and H. Wielicki

221 High-Level Current Gain in Bipolar Power Transistors
J. Olmstead, W. Einthoven, S. Ponczak, and P. J. Kannam

247 Observation of the Influence of Base Widening Upon Beta and f_T
C. F. Wheatley

251 Systems and Technologies for Solid-State Image Sensors
Paul K. Weimer

263 Optical Techniques for Detecting Defects in Silicon-On-Insulator Devices
Richard A. Sunshine

279 Symmetrical Trough Wavequide Nonresonant Ferrite Isolators and Steerable Antenna
C. P. Wen

289 RF Sputtered Transparent Conductors II: The System In_2O_3-SnO_2
John L. Vossen

297 Contrast Thresholds of Image-Intensifier-Aided Eye at Low Field-Luminance Levels
Illes P. Csorba

306 A Technique for Selective Electroless Plating
N. Feldstein and T. S. Lancsek

311 The Ad-Conductor Cathode
Karl G. Hernqvist

319 Permanent-Holograms in Glass by RF Sputter Etching
J. J. Hanak and J. P. Russell

325 RCA Technical Papers

327 Patents

330 Authors

June 1971 Volume 32 Number 2

RCA Corporation

Robert W. Sarnoff Chairman of the Board and President

Editorial Advisory Board

Chairman, J. A. Rajchman RCA Laboratories
E. D. Becken RCA Global Communications
G. H. Brown RCA Patents and Licensing
G. D. Cody RCA Laboratories
A. L. Conrad RCA Services
H. L. Cooke, RCA Research and Engineering
A. N. Goldsmith Honorary Vice President, RCA
N. L. Gordon RCA Laboratories
G. B. Herzog RCA Laboratories
J. Hillier RCA Research and Engineering
E. O. Johnson RCA Solid-State Division
H. W. Leverenz RCA Patents and Licensing
D. S. McCoy RCA Laboratories
H. F. Olson RCA Laboratories
K. H. Powers RCA Laboratories
P. Rappaport RCA Laboratories
F. D. Rosi RCA Laboratories
L. A. Shotliff RCA International Licensing
T. O. Stanley RCA Laboratories
J. J. Tietjen RCA Laboratories
W. M. Webster RCA Laboratories
L. R. Weisberg RCA Laboratories

Secretary, Charles C. Foster RCA Research and Engineering

Editor Ralph F. Ciafone

Associate Editors

W. A. Chisholm RCA Limited
D. B. Dobson Aerospace System Division
M. G. Gander RCA Service Company
T. G. Greene Missile and Surface Radar Division
W. O. Hadlock RCA Research and Engineering
W. A. Howard National Broadcasting System
C. Hoyt Consumer Electronic Systems Division
C. A. Meyer RCA Electronic Components
M. G. Pietz Defense Engineering
C. W. Sall RCA Laboratories
I. M. Seideman Astro-Electronics Division
W. Varnum Commercial Electronic Systems Division

© RCA Corporation 1971 All Rights Reserved Printed in USA

Analysis of Transport Processes During Holographic Recording In Insulators*

Juan J. Amodei, RCA Laboratories, Princeton, N. J.

Abstract—This paper presents a discussion of drift and diffusion processes that give rise to charge migration in insulators exposed to spatially varying light patterns. The resulting fields and distribution of trapped charges are calculated for the case of sinusoidally varying interference patterns such as those corresponding to plane wave holograms. A comparison of the two processes shows that diffusion would dominate in holographic recording when the electric fields applied are less than 1600 V/cm and the fringe spacing less than 1 μm. The electric fields resulting from the two processes are spatially in quadrature. It is also shown that insufficient trap density could be a factor contributing to resolution limitations, and that diffusion length is not likely to be an important consideration in determining resolution.

Introduction

When free carriers are excited by light of nonuniform intensity distribution within an otherwise insulating material with an applied electric field, the carriers migrate and generate regions of unneutralized charge that persist after the light is removed. This type of phenomenon was proposed by Chen[1] to explain the "optical damage" effects in KTN and other electro-optic crystals following exposure to high-intensity laser beams.[2] Chen, LaMacchia, and Fraser[3] later reported the storage of high-efficiency holograms in $LiNbO_3$ through a similar "damage" effect that was attributed to the presence of polarization-induced internal fields in these ferroelectric crystals. A similar approach was taken by Thaxter[4] to record holographic patterns in strontium–barium niobate crystals by applying a strong electric field during exposure. The results of all these experiments were qualitatively explained on the basis of drift of excited carriers under the influence of the electric fields, inherent or applied. The space-charge fields generated by the

* Work supported in part by the Naval Air Development Center, Department of the Navy.

drift and subsequent retrapping modulate the index of refraction through the electro-optic effect, giving rise to a phase hologram. A similar effect can be obtained through thermal diffusion, even in the absence of an electric field.[5]

An alternative theory was presented by Johnston,[6] who proposed a light-generated polarization pattern to explain index damage effects in pyroelectric crystals and was used by Townsend and LaMacchia[7] to explain holographic storage effects in $BaTiO_3$. Johnston points out that the defects or traps in these crystals may contribute a macroscopic polarization along the c-axis, which would vary as the concentration of filled traps. He proposes that the drift field seen by Chen[1] is the result of the change in density of filled traps as electrons are excited to the conduction band. Because of the diffuse nature of the conduction-band states, he argues that these free electrons contribute no dipole moment so that the process gives rise to a net change in polarization in the illuminated region. Since the divergence of the polarization constitutes an effective space charge, he postulates that a drift field along the c-axis is generated in the illuminated region. This field is seen as the one responsible for the net drift of electrons out of the illuminated areas and into dark regions, causing a more permanent change in the dipole density. Johnston attributes the modulation of the index of refraction to these variations in polarization, which persist after the internal fields have relaxed. There are many conceptual difficulties with this model, such as the extremely high density of free electrons required to generate the large fields necessary to account for the observed effects. Nevertheless, it is conceivable that in some crystals with the proper concentrations of polar centers, these large changes in polarization could occur through transfer of charge between localized centers of different nature creating index changes *without* need for drift or migration. This possibility is discussed in more detail.

Regardless of the alternative mechanisms that can give rise to index variations, there is no question that transport processes, namely drift and diffusion, do take place in any material exposed to nonuniform illumination. It is also clear that the resulting migration may give rise to sufficient space-charge accumulation to explain the magnitude of the observed holographic storage effects, and that the effect may have other interesting applications. Therefore, it is the purpose of this paper to present a simple model to be used as foundation for quantitative analysis of drift and diffusion in holographic recording, to help evaluate the relative role of these two processes, and to guide the choice of the model best suited to explain the experimental results in a given

material. While some of the previously proposed models are restricted to pyroelectric crystals, the space-charge field formation due to diffusion or applied fields analyzed here constitutes a fundamental process that would take place in any insulator with traps regardless of crystal structure. The shape, magnitude, phase, and rate of development of these fields when the light intensity pattern is sinusoidal are the subject of this paper.

General Considerations

Since any arbitrary interference pattern can be decomposed into a superposition of sinusoidal intensity distributions, we can greatly simplify our treatment by dealing exclusively with sinusoidal patterns. Even though some of the phenomena to be discussed are nonlinear in nature, so that, strictly speaking, superposition can not be used to get the resultant field pattern, this treatment should provide a good first-order approximation over a rather wide operating range.

The interference pattern generated by two plane waves of light of wavelength λ intersecting at an angle θ is given by

$$I(x) = I_o(1 + m \cos Kx), \qquad [1]$$

where x is the direction in the plane of the two beams perpendicular to their bisector, m is the modulation ratio,

$$K = \frac{2\pi}{l},$$

$$l = \frac{\lambda}{2 \sin \theta/2} = \text{the wavelength of the interference pattern.}$$

Assume that this pattern is applied to a nearly transparent insulator that has a uniform distribution of trapped electrons that can be excited to the conduction band by light of this wavelength. (Although the word electron is used throughout, it is clear that the analysis applies equally well when holes or other charged particles are the carriers). For an optical absorption cross section of the trapped electron given by σ, a concentration N, and a light frequency ω, the volume generation rate $g(x)$ of free electrons can be written as

$$g(x) = \frac{I_o \sigma N}{\hbar\omega} [1 + m \cos Kx], \qquad [2]$$

where $\hbar$ is Planck's constant.

If the diffusion length of the free electron is substantially shorter than the wavelength of the interference pattern, l, the free carrier concentration would remain a faithful replica of the generation rate. In fact, if one assumes that the trapping time (τ), is not a function of concentration of free carriers, the free electron density $n(x)$ would be given by

$$n(x) \approx \tau g(x) = \frac{\tau I_o \sigma N}{\hbar \omega} [1 + m \cos Kx], \qquad [3]$$

or, defining a concentration, n_o, by

$$n_o = \frac{\tau I_o \sigma N}{\hbar \omega}, \qquad [4]$$

the concentration of free electrons can be written as

$$n(x) \approx n_o [1 + m \cos Kx]. \qquad [5]$$

It will be assumed in this analysis that the concentration of trapped electrons, N, is sufficiently large that the variations due to charge migration are negligibly small and leave the generation rate and trapping time essentially constant during the process. Thus, $n(x)$ will be assumed to be given by Eq. [5] for all times.

The above free-carrier distribution would give rise to inhomogeneous current densities via diffusion and drift, resulting in a net migration and retrapping of electrons away from regions of high-intensity light. The resulting trapped space charge gives rise to electric fields. In an electro-optic crystal these fields can modulate the index of refraction and thus generate a hologram. The contributions to the field due to local change in density of impurity dipoles will be neglected because, if one assumes the model proposed by Johnston, these contributions will be much smaller than those of the space charge.

Analysis of Field Build-up Through Drift and Diffusion Effects

If the material is isotropic or if the x direction is along one of the crystallographic axes, the spatial distribution of the current is given by the sum of the diffusion and drift components as

$$J(x) = qD_n \frac{dn}{dx} + qn\mu_n E(x), \qquad [6]$$

where q is the electronic charge

D_n is the diffusion constant for electrons,

μ_n is the mobility for electrons,

$E(x)$ is the total electric field, which is assumed to be in the x direction.

Now, the rate at which space-charge density, ρ, accumulates at any point is given by the continuity equation

$$\frac{d\rho}{dt} = -\nabla . J, \qquad [7]$$

which, for our one-dimensional case, reduces to

$$-\frac{d\rho}{dt} = \frac{dJ}{dx} = qD_n \frac{d^2n}{dx^2} + q\mu_n E \frac{dn}{dx} + q\mu_n n \frac{dE}{dx}. \qquad [8]$$

Hence, the build-up in charge density can be expressed formally by the integral

$$\rho(t) = -\int_o^t \frac{dJ}{dx} dt, \qquad [9]$$

which, in general, cannot be solved exactly for our problem.

Given the charge density, an expression for the electric field at any time can be calculated by

$$E(x) = \int \frac{\rho}{\epsilon} dx + E_o, \qquad [10]$$

where ϵ is the static dielectric constant of the material.

Quantitative results and better insight into the relative importance of drift and diffusion can be attained by considering two specific situations: (1) the case where there is a dc field high enough that the diffusion component of current can be neglected compared to the drift component, and (2) the case in which there is zero applied (or inherent) electric fields.

1. Constant Applied Electric Field Dominant

Assuming at first that we restrict our observation to times short enough that the varying portion of the field, which is due to the space charge, $E_\rho(x)$, is much smaller than the applied field itself, we can write

$$E(x) = E_\rho(x) + E_o \approx E_o.$$

For this situation,

$$\frac{dJ}{dx} \approx q\mu_n E_o \frac{dn}{dx}. \quad [11]$$

Assuming a sinusoidal pattern for $n(x)$ as given by Eq. [5], and using Eq. [9], one obtains an expression for the charge built up;

$$\rho(t) \approx (q\mu_n E_o n_o m K \sin Kx)t. \quad [12]$$

The spatially varying portion of the field would then be given by

$$E_\rho(x) = \int \frac{\rho}{\epsilon} dx = -\left[\frac{q\mu_n n_o E_o m}{\epsilon} \cos Kx\right] t. \quad [13]$$

That is, the net electron drift caused by a large uniform electric field applied to the material with a sinusoidal excited carrier distribution, would give rise to a *trapped* charge density that is also sinusoidal and 90° out of phase with the light intensity pattern. This charge density would initially give rise to a spatially sinusoidal electric field whose peaks occur at the high-intensity minima of the light interference pattern. It can also be seen from Eq. [13] that the factor determining the build-up rate of the field is the ratio of the photogenerated conductivity to the dielectric constant $q\mu_n n_o/\epsilon$, which constitutes the inverse of the RC time constant for the material at the given level of illumination. This is a simple quantity to determine experimentally.

As the inhomogeneity in the current density continues to build up space charge, the effect of the resulting field, $E_\rho(x)$, on the transport pattern can no longer be neglected, and Eq. [13] becomes a poor approximation. When the equilibrium distribution is actually reached, however, a simplified analysis can again be used to find the magnitude and spatial dependence of the field.

From an inspection of Eq. [9] it is apparent that steady-state con-

ditions will be reached when the current density becomes uniform; that is,

$$\frac{dJ}{dx} = 0. \qquad [14]$$

At equilibrium, therefore, it follows that

$$qD_n \frac{d^2n}{dx^2} + q\mu_n E \frac{dn}{dx} + q\mu_n n \frac{dE}{dx} = 0. \qquad [15]$$

Again, under the assumption of large applied electric field, Eq. [15] reduces to

$$E \frac{dn}{dx} + n \frac{dE}{dx} = 0, \qquad [16]$$

which may be integrated directly to yield

$$E(x) = \frac{E(0)(1+m)}{1 + m \cos Kx}, \qquad [17]$$

where $E(0)$ is the electric field at the edge of the sample ($x = 0$) and its value depends on the boundary conditions (i.e., whether the voltage across the sample is fixed or the charge density at the surface is fixed). Only for $m \ll 1$ does this expression give a sinusoidal field. For that case,

$$E(x) \approx -E(0) m \cos Kx. \qquad [18]$$

One should point out here again that the above assumes $n(x)$ to be given by Eq. [5] and to remain unchanged during the build-up to equilibrium, a condition that requires a large trapped-charge concentration. If during the rearrangement process one depletes most of the trapped electrons from the regions of high-intensity light, this assumption will not hold; in this case, the field will come to equilibrium at a lower value. This is discussed in more detail in the section on resolution. The above analysis also shows that, for the case of a drift-generated field, there is no distortion of the sinusoidal shape of the interference pattern being recorded only when $m \ll 1$ or when the re-

cording is stopped while the space-charge field, $E(x)$, is still much smaller than the applied field, E_o. The fact that the expression for $E(x)$ diverges for $m = 1$ is a consequence of the assumption of very short diffusion length; a finite diffusion length would decrease the effective value of m and would remove this anomaly.

2. Diffusion Only (No Applied Field)

If the initial applied field is taken to be zero, the only field present would be that generated by the unneutralized space charge, $\rho(x)$, so that the current will be given by

$$J(x) = qD_n \frac{dn}{dx} + qn\mu_n E_\rho(x). \qquad [19]$$

As explained in a previous paper,[5] the space charge will build up until the field is sufficient to cancel the diffusion component of the current everywhere. Hence, at equilibrium,

$$J(x) = 0,$$

and

$$E(x) = E_\rho(x) = \frac{D_n dn/dx}{\mu_n n} = \frac{kT dn/dx}{qn}, \qquad [20]$$

where we have used the Einstein relation between mobility and conductivity:

$$D_n = \frac{kT}{q} \mu_n$$

where k is the Boltzmann constant and T is the temperature.

Now, Eq. [5] was shown to give the correct distribution of free electrons for all times under the assumptions of very short diffusion length and large trapped-electron concentrations. For the *equilibrium* case

in question this expression is correct regardless of diffusion length. This follows because at equilibrium $J(x)$ is zero everywhere, and, hence, the free-electron density will conform exactly to the shape of the generation rate, $g(x)$, (still assuming that the recombination rate is constant everywhere). Therefore, using Eq. [5], we obtain an expression for the equilibrium field, $E(x)$;

$$E(x) = \left(\frac{kT}{q}\right)\left(\frac{Km \sin Kx}{1 + m \cos Kx}\right). \qquad [21]$$

This diffusion-generated field is seen to be sinusoidal only for small values of m, as was the case with that generated through drift. Also, if Eq. [21] is expanded in a Fourier series, the only component that would contribute to the diffraction efficiency is the fundamental, whose magnitude is $E_m = (kT/q)(Km/\sqrt{1-m^2})$. The peaks of this fundamental sinusoid are displaced by about one quarter of the spatial wavelength, l, relative to those of the drift-generated pattern. Another difference between the two processes is that the diffusion-generated field is proportional to the spatial frequency of the interference pattern, K, while the drift induced field is not, so that diffusion becomes especially important when the fringe spacing is very short.

For a sinusoidal excitation with a given applied field, the relative importance of drift and diffusion in building up the unneutralized charge can be estimated by the initial peak value of the divergence of the current associated with each process. Since $E(x) = E_o$ initially, the ratio of peak diffusion current divergence, dJ_D/dx, to that of drift current, dJ_E/dx, can be calculated to be

$$R = \frac{dJ_D/dx}{dJ_E/dx} = \left(\frac{kT}{q}\right)\frac{K}{E_o}. \qquad [22]$$

At room temperature this may be written as

$$R \approx \frac{0.16}{E_o l} \qquad (E_o \text{ in V/cm}). \qquad [23]$$

For example, with a fringe spacing of $l = 10^{-4}$ cm, the two processes will be equally important ($R = 1$) when the applied field is $E_o = 1600$ V/cm. It is important to note that this result is independent of material parameters or type of carriers.

Thermally and Optically Induced Decay

We now turn our attention to the reverse process, that of thermal or optical erasure of the field pattern that has been generated in the manner discussed above.

For simplicity we assume that the recorded field pattern is a perfect sinusoid;

$$E = E_m \cos Kx, \tag{24}$$

corresponding to a space charge density

$$\rho = -\epsilon K E_m \sin Kx. \tag{25}$$

Now, the initial trapped electron distribution throughout the material will be

$$n_t = N - \frac{\rho}{q}. \tag{26}$$

The excitation rate, whether it be thermal or optical, would be directly proportional to the trapped electron concentration so that still assuming a very short diffusion length and following the reasoning that was used to arrive at Eq. [3], the free carrier concentration may be written as

$$n \approx A n_t = A\left(N - \frac{\epsilon K E_m}{q} \sin Kx\right), \tag{27}$$

where $A = I_o \sigma \tau / (\hbar \omega)$ for the case where optical excitation dominates. An approximate solution can be easily obtained for the case where $N \gg n_t$, for which the free carrier concentration can be assumed to be nearly uniform. For this case, the main contribution to the decay of the pattern would come from the drift of the optically or thermally excited electrons. The current density, under these assumptions, would be given by

$$J \approx qAN\mu_n E = qAN\mu_n E_m \cos Kx. \tag{28}$$

Using Eq. [7],

$$\frac{dJ}{dx} = -qAN\mu_n K E_m \sin Kx = -\frac{d\rho}{dt}. \tag{29}$$

Therefore, assuming that the field distribution remains sinusoidal during decay, and using Eq. [25], we obtain

$$\frac{dE_m}{dt} = -\frac{qAN\mu_n}{\epsilon} E_m, \quad [30]$$

and

$$E_m(t) = E_m(0)e^{-t/\tau_{RC}}, \quad [31]$$

where $\tau_{RC} = \epsilon(qAN\mu_n)$ can be recognized as the RC time constant of the material at the given temperature and illumination level. This result is to be expected because our assumption of large trap concentration amounts to spatially uniform conductivity.

One might note that storage times of about one month in materials with relative dielectric constants of 30, such as $LiNbO_3$, imply dark resistivities of 10^{18} ohm-cm. This value is many orders of magnitude higher than was measured by Johnston[7] but is consistent with our conductivity measurements at elevated temperatures. Also, in a heavily reduced sample with resistivities in the range of 10^{10} ohm-cm, the observed decay times of the holograms agree with the room-temperature measured values of conductivity.

Effect of Trap Density on Resolution

Under the assumptions made in the above analysis there are no apparent limitations to the spatial wavelength of the field grating that can be induced into an insulator by a light-interference pattern. However, it should be clear that the magnitude of the field can be limited by the available trap density in the material. This can be seen by an examination of Eq. [25], which shows that the unneutralized charge density, ρ, required to produce a given field amplitude, E_m, increases linearly with the spatial frequency, K. From Eq. [25], the peak charge density, ρ_m, can be written in terms of the peak field, E_m, as

$$\rho_m = \epsilon K E_m = \frac{2\pi\epsilon E_m}{l}. \quad [32]$$

Thus, the maximum field for a given trap density, N, can be written as

$$E_m = \frac{qNl}{2\pi\epsilon}. \quad [33]$$

For a trap density of 10^{16} cm^{-3}, a relative dielectric constant of 30, and a fringe spacing of 10^{-4} cm, the peak field that can be induced would be 10^4 V/cm. This should be more than sufficient to produce high diffraction efficiency in good electro-optic materials. However, a factor of ten lower value in the trap density could pose a serious limitation in resolution capabilities.

Discussion of Impurity Polarization Effects

It is interesting to discuss the polarization model proposed to explain optically induced changes of index of refraction in $LiNbO_3$ in the light of the results obtained from the above analysis. The model proposed by Johnston[6] assumes that the local dipole moment of the cell containing the defect changes positively when the defect loses its normally trapped electron and negatively when it traps a second electron. Thus, after allumination and before dielectric relaxation takes place, the light-induced change in dipole density, n_d, would equal the local space charge divided by the electronic charge;

$$n_d = \frac{\rho}{q}. \quad [34]$$

The polarization induced by this model is

$$P = qn_d\delta = \rho\delta, \quad [35]$$

where δ is an equivalent dipole length, which must be of the order of the unit cell dimension. Assuming, therefore, that we have a sinusoidal distribution of space charge,

$$\rho(x) = \rho_m \sin Kx. \quad [36]$$

The accompanying polarization would be given by

$$P_\rho(x) = \delta\rho_m \sin Kx. \quad [37]$$

But the peak field created by the above space charge (neglecting $\nabla .P$, which, from Eq. [37], can be seen to be much smaller than ρ) would be

$$E_m = \frac{\rho_m}{\epsilon K}. \quad [38]$$

Now, the peak value of the field-induced polarization (that which occurs through distortion of the lattice by this space charge field) can be written as

$$P_{E_m} = (\epsilon - \epsilon_o) E_m = \frac{\epsilon - \epsilon_o}{\epsilon} \frac{\rho_m}{K} . \quad [39]$$

Thus the ratio of the peak value of polarization due to space-charge generated field and that due to dipole formation as a result of charge migration is

$$\frac{P_{E_m}}{P_m} = \frac{\epsilon - \epsilon_o}{\epsilon} \frac{l}{2\pi\delta} . \quad [40]$$

Since $(\epsilon - \epsilon_o)/\epsilon \approx 1$ and $l/\delta \sim 10^3$, we see that the dipole concentration generated by this process would have a negligible effect on the total change in polarization compared to that of the space-charge-generated field. Thus it appears that, *as long as the model requires the transfer of charge* in order to change the net local dipole density, the polarization model is not valid. It simply requires the transfer of orders of magnitude more charge to achieve the same effect. A modification of Johnston's model where there is a transfer of charge between polar centers of different dipole moment requiring no net migration of carriers (drift or diffusion) presents an additional possibility that should be considered. In a material obeying this model, transport processes and accompanying space-charge-field formation may well occur, but they are completely unnecessary to achieve the index changes and are thus not relevant to the model. This type of process, which may take place in some materials, becomes simply a polarization version of the photochromic phenomenon. Thus the dynamics of the recording behavior will follow the well-understood dynamics of photochromic switching, and the experimental results should be explainable on this basis.

Johnston also proposes that there is a light-induced change in polarization due to the excitation of electrons into the conduction band, and suggests that this may give rise to the large drift fields observed by Chen. As was mentioned in the introduction, the concentration of free electrons that would be needed to account for fields of this magnitude are nearly impossible to achieve. However, Johnston's hypothesis of a light-generated polarization field is extremely interesting, and could well contribute to the formation of large fields in some materials. In particular, if the material possessed a large number of shallow

traps with short life times, it would appear that a rapid transfer of electrons from the deep traps to these centers could create the effect envisioned by Johnston with much larger changes in polarization now being possible.

Conclusions

In summary, the very complex and diverse behavior of the materials used for holographic storage might not be explainable by any single model, and no such claim is made for the transport processes discussed here. The results of the simplified analysis presented in this paper are meant to give a quantitative picture of the magnitude of the fields that would be generated due to light-induced space charge, their spatial distribution, and the phase relationship between these fields and the light pattern inducing them. The latter is an important consideration on the hologram recording dynamics, because it affects the light intensity distribution during the growth of the hologram.[8] These transport effects are of a most fundamental nature in that they would be present to a greater or lesser extent in any insulator with traps. Whether or not all of the observed index changes in electro-optic crystals follow exclusively the transport model remains to be seen. Evidence to date suggests that holographic recording in nominally pure $LiNbO_3$ involves this type of process, while some of the heavily doped samples may not.[8]

Acknowledgments

The author is indebted to Richard Williams and David Staebler for the many helpful discussions, suggestions, and contributions that they have made in the course of this work and to Albert Rose and Dietrich Meyerhofer for critical review of the manuscript.

References

[1] F. S. Chen, "A Laser-Induced Inhomogeneity of Refractive Indices in KTN," **J. Appl. Physics,** Vol. 38, p. 3418 (1967); "Optically Induced Change of Refractive Indices in $LiNbO_3$ and $LiTaO_3$" **J. Appl. Phys.,** Vol. 40, p. 3389 (1969).

[2] A. Ashkin, et al, "Optically-induced Refractive Index Inhomogeneities in $LiNbO^3$ and $LiTaO_3$," **Appl. Phys. Letters,,** Vol. 9, p. 72 (1966).

[3] F. S. Chen, J. T. LaMacchia, and D. B. Fraser, "Holographic Storage in Lithium Niobate," **Appl. Phys. Letters,** Vol. 13, p. 223 (1968).

[4] J. B. Thaxter, "Electrical Control of Holographic Storage in Strontium-Barium Niobate," **Appl. Phys. Letters,** Vol. 15, p. 210 (1969).

[5] J. J. Amodei, "Electron Diffusion Effects During Hologram Recording in Crystals," **Appl. Phys. Letters,** Vol. 18, p. 22 (1971).

[6] W. D. Johnston, Jr., "Optical Index Damage in $LiNbO_3$ and Other Pyroelectric Insulators," **J. Appl. Phys.,** Vol. 41, p. 3280 (1970).

[7] R. L. Townsend and J. T. LaMacchia, "Optically Induced Refractive Index Change in $BaTiO_3$," J. Appl. Phys., Vol. 41, No. 13, Dec. 1970.

[8] D. L. Staebler and J. J. Amodei (unpublished).

System Aspects of Electrophotographic Materials and Processing for Liquid Reversal Toning

E. C. Giaimo and H. Wielicki
RCA Laboratories, Princeton, N. J.

Abstract—Electrophotographic materials and processing techniques have been adapted to a system in which image reversal using liquid toner is required from a cathode-ray exposure device. It was found that image quality is dependent not only on materials but also upon the restraints imposed by the overall system. Compacting of the processing machine leads to electrical interactions between the corona charger and the toning process as a result of lateral conduction in the copy paper. The machine design is intimately associated with the composition of the paper used. The reversal toning also imposes higher quality standards on ZnO-resin coatings and base-paper substrates that are not normally found in office copier papers currently available.

An equivalent circuit representation has been made that clarifies the relationship of the ZnO-resin paper, the liquid reversal developer, and the external electrical field applied at the development site. The transient electrical currents flowing during development show the time dependent nature of the toning phenomenon and its interrelation with the toning time imposed by the toning unit configuration and overall system restraints.

Development of Concepts

Some of the special requirements of the electrophotographic printer for use with the Homefax system have been described by Houghton.[1] In this paper, the evolution of the image developing system is described in greater detail.

At the time when the first prototype models of Homefax printers were being planned, the (Electrofax*) electrophotographic office copier industry was already a commercial reality and the adaptation of available materials and technology appeared to be the most logical and expeditious course to pursue. However, as shall be seen, problems unique to the design of this printer arose which could not be solved with existing materials and technology.

---

* Registered trademark of the RCA Corporation

Two commercially successful methods of electrophotographic image development were available to choose from: liquid development and dry-powder development. In liquid development, which was and still is the most popular among copier manufacturers, the charged and exposed sheet is passed through a trough or roller system that applies developer liquid (toner) to the copy surface and then removes the excess. The developer liquid is comprised of pigment particles (such as carbon black) having a size range of 0.1 to 0.5 μm dispersed (with the aid of suitable surface active agents) in a liquid hydrocarbon. Depending upon the charge that has been imparted to the pigment (developer) particles by the surface active agent, the particles are deposited on either the charged or the light-discharged areas of the print. The hydrocarbon is electrically insulating (at least 1×10^{11} ohm-cm resistivity), chemically quite inert, and has a boiling point of approximately 350°F and a flash point (Tag Closed Cup) of 125°F. An example of such a liquid is the isoparaffinic solvent marketed under the trade name Isopar H by Humble Oil and Refining Company. A low-temperature heat source in conjunction with a low-velocity blower is frequently used to dry the paper and fix the image.

In dry-powder development, as the name implies, the image is made visible by brushing dry pigmented resin particles on the charged image. Depending upon the charge on the powder particles, which is determined by the composition of the powder, they adhere either to the charged or the light-discharged areas of the paper. Heat is then used to melt the resin component of the particles, thus fusing them to the paper and fixing the image.

Liquid development was selected for the Homefax printer for essentially the same reasons that it is preferred in office copiers, namely, (1) the developed image is essentially self-fixing and does not require a high wattage heat source to fuse the toner, (2) toner replenishment is easier in a liquid system, (3) there is no problem of dust or grit getting into the various parts of the printer mechanism, and (4) a liquid development system can be built more compactly than a dry-powder system.

A variation of liquid development referred to as hot-melt development was also tried. Hot-melt development is essentially the same as liquid development, but actual development is performed at an elevated temperature (80° to 110°C). In this method, a paraffin wax or a microcrystalline wax is used as a diluent or carrier for the pigment instead of a liquid hydrocarbon. The unused portion of the developer is stored as a solid cake, bar, or pellets; a small quantity is melted as needed for image development.

In the preceding discussion, reference has been made to two different models of electrophotographic image developing—one in which the developer particles (be they in a dry or a liquid medium) are attracted to the charged areas of the image and another in which the developer particles are attracted to the light discharged areas of the image. The former is generally called direct positive development and the latter is called reversal development.

The advantages of reversal development in conjunction with the thin-window CRT exposure method were well-known before the Homefax project started,[2,3] but even reasonably stable and reliable liquid reversal developers were nonexistent at that time. Thus, liquid direct positive developing was used at first, then hot-melt direct positive developing was investigated. Not long thereafter a hot-melt reversal developer was formulated; finally, when the problems encountered in handling a hot paraffin wax system could not be solved easily in the time allotted, a usable liquid reversal developer was formulated.

Shortly thereafter, a halogenated hydrocarbon, trichlorotrifluoroethane (marketed under the tradenames Freon-TF and Genesolv-D by DuPont and Allied Chemical Company, respectively) was substituted for the isoparaffinic hydrocarbon because it provided the rapid drying and non-flammability considered necessary for use in a home instrument. This led to the design of a fountain developing mechanism.[4]

System Interactions

This paper is concerned in part with the processing of ZnO–resin coated paper as the hard-copy output medium of an experimental processing unit using cathode-ray-tube exposure. In order to conserve the life of the cathode-ray-tube phosphor, the reversal printing mode is used. In the reversal printing mode, toner is deposited in the exposed areas of a previously uniformly charged sheet. The exposure is such as to either reduce the charge to zero or reduce it considerably below the charge density remaining in the surrounding regions where no light was allowed to fall. During the developing interval, an electric field is impressed, by means of electrodes, across both the paper and the developing fluid. By making the electric field variable, one is able to control print density, fill in large exposed areas, and control contrast ratio and spurious background toner deposition. Data, in addition to that published previously,[5] is presented showing the toning behavior of ZnO–resin coated paper under the above mode of operation.

During the course of our investigation, it became evident that the

processing of the ZnO–resin coated paper and the design of the processing unit must be approached as a system. It was found that certain machine design parameters dictated by the overall Homefax system in which the Electrofax process was to operate influenced the processing and was reflected in the quality of the output copy. Parameters such as paper speed and compacting of the overall mechanism and its components to arrive at a physically small machine can influence all three steps (charging, exposure, and toning) needed to process electrophotographic paper. The interdependence of the machine configuration and the functioning of the processing units will be treated in more detail subsequently.

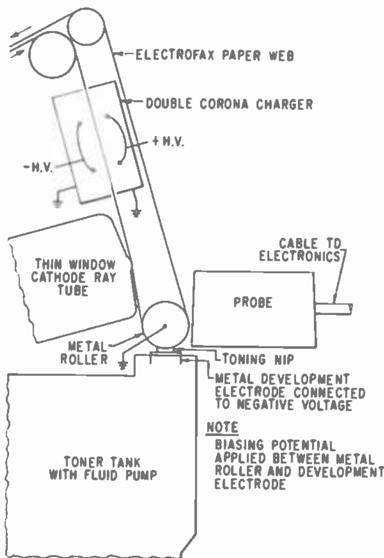

Fig. 1a—Experimental printer.

Although the experimental printer shown in Fig. 1a, b, c was used to investigate the reversal printing characteristics of photosensitive paper and toners, it should be considered in a more general sense. In the general sense, this machine is a device for transporting a web of the paper through a charging device, past an exposure station and then through liquid toner which contacts only the ZnO–resin coating of the paper web. In addition, the machine has each of the processing functions in close proximity to one another. Further, the paper web travels at the relatively slow rate of 0.3 to 0.6 inches per second.

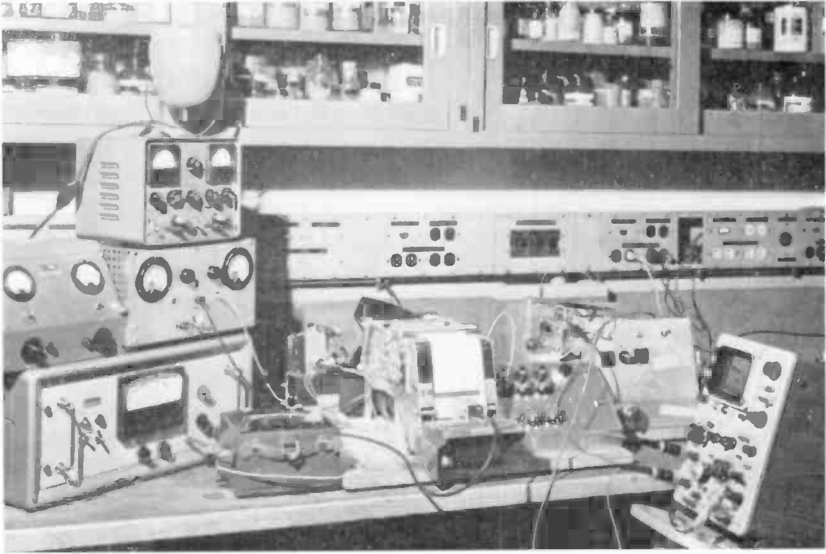

Fig. 1b—Experimental apparatus overall view.

Fig. 1c—Experimental apparatus showing electrostatic probe location.

Charging

During the course of our investigation of reversal toning of ZnO–resin coated paper, it was found that a spurious toner deposit was present in the background areas of the output copy. This was traced to electrical breakdown of the charge retaining layer. The breakdown resulting in nonuniform charge density is introduced during the charging interval because of the low paper speed of the device. The low paper speed is a requirement imposed by the overall system and is related to the repetition rate of the line scan exposure. In order to overcome the overcharging difficulty, controlled charging was used wherein the corona unit was intermittently energized with high voltage. It was found that intermittent charging having a duty cycle of about 10% yielded maximum charge with a reduced number of breakdown spots and reduced spurious toner deposits in the reversal prints.

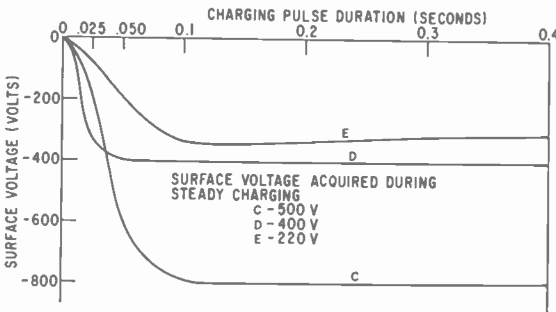

Fig. 2—Intermittent charging (pulse repetition interval 1 second; paper speed 0.3 inch/second.

In the series of tests on three commercial papers, it was found that maximum surface potential could be obtained using 0.1-second pulses of high voltage direct current applied to the corona unit at one-second intervals. Intermediate surface potentials could be obtained by applying shorter pulses. The data obtained is shown in Fig. 2. Included on the graph are the voltages obtained with steady charging with the paper moving at 0.3 inch per second. The data clearly shows that a lower surface potential occurs with steady charging at low paper speeds in the device shown in Fig. 1a.

The curves show that control of the surface potential can be obtained using the intermittent mode of charging. Surface potentials less than maximum can be obtained by changing the pulse duration and/or duty cycle. It can be seen from the curves of Fig. 2 that the

charging characteristics of the three papers tested are different. In a given device with a given paper, the intermittent charging can be used to control the surface potential below the maximum attainable. The corona potential cannot be reduced below the voltage required to produce a corona discharge, thus a lower limit is set on the surface potential.

A series of tests were made to determine the surface potential of a commercial paper as a function of paper speed when steady charging is used. It was found that maximum potential occurs at 0.4 in/sec. The data is shown in Fig. 3. At paper speeds of 0.3 in/sec and 0.6 in/sec, it appears that over- and under-charging occurs, respectively. For this part of the investigation, the corona voltages were set at +4kV on the positive corona wires and −4.5kV on the negative corona wires.

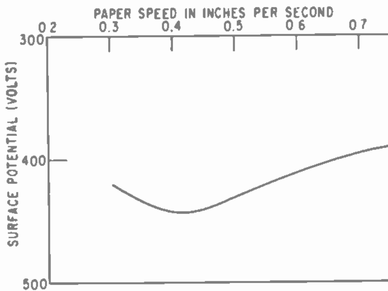

Fig. 3—Surface potential of commercial electrophotographic paper as a function of paper speed with steady charging.

The values of steady corona voltage chosen were derived experimentally for the test printer. The data is shown in Fig. 4. The use of intermittent charging appears to be of value for controlling surface potential where low fixed paper speeds are required in the processing device.

In the Homefax system for which this work was done, intermittent charging was found to be ideal for minimizing corona interference with the television input signals. Details of the circuitry and the synchronization of the pulses to minimize interferences will be treated elsewhere.[6]

A second area of corona charger interaction with the system results from compacting the processing functions, using papers having conductive layers, and applying arbitrary voltages to a double corona charger.

As a result of compacting the processing functions and using ZnO–resin coated paper in the form of a paper web, it was found that current originating in the corona charger flows along the paper and gives rise to potentials in the developing unit. Such potentials can drastically modify the toning process. The electrical coupling between the charger and the toning device is not unique with a machine using a paper web. The same conditions can also arise in a machine using paper sheets where the spacing of the charging and toning functions allows different areas of the sheet to be in both locations simultaneously.

A detailed diagram of the processor is shown in Fig. 5. An electrical equivalent circuit of the device is shown in Fig. 6. From Fig. 6, it is apparent that point A (the interface between the coating and the substrate), which represents the area immediately under the double charger, should be maintained at ground potential to prevent a potential from appearing across the paper base due to current flow along the paper web in those instances where conductive surface treatments are given to the base stock. This condition can be arrived at by adjusting the corona potentials and/or spacings from the paper surfaces so that a ground plane is maintained at point A. Other electrical

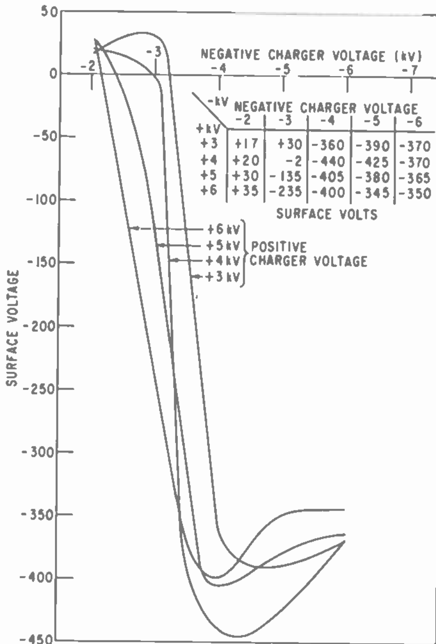

+kV \ -kV NEGATIVE CHARGER VOLTAGE	-2	-3	-4	-5	-6
+3	+17	+30	-360	-390	-370
+4	+20	-2	-440	-425	-370
+5	+30	-135	-405	-380	-365
+6	+35	-235	-400	-345	-350

SURFACE VOLTS

Fig. 4—Surface voltage vs. charger voltage for steady charging.

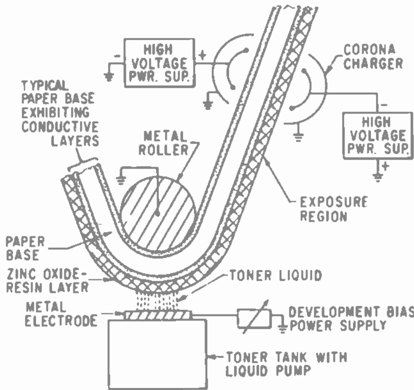

Fig. 5—Detailed diagram of processor.

solutions are also possible. Adjustment of the corona potentials and/or spacing can be determined by nulling the current flow from ground to the electrode contacting the back side of the paper at the developer unit.

Other solutions to this electrical interaction are involved with the design of the paper substrate. These include elimination of electrically floating conductive layers and decreasing the through resistance of the paper base. Specific resistance values are difficult to specify because the potentials appearing at point B which modify the toning process are unique with the machine design, the corona operating conditions, and the deposition characteristics of the toning liquids. In addition, variation of the lateral conductivity of the paper web with relative humidity must also be considered.

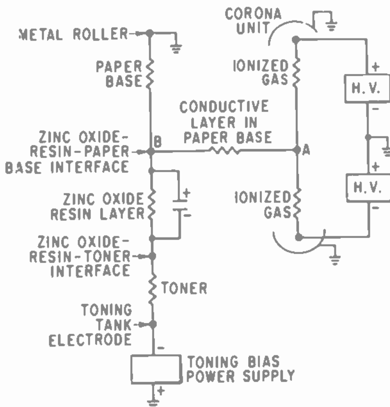

Fig. 6—Equivalent electrical circuit existing in processor where paper web electrically connects charger to toning device.

Exposure

The exposure of the photosensitive paper in the test device is in the form of a line scan occuring at a repetition rate of 60 per second. The paper is run in optical contact with a thin-window cathode ray tube having a 0.0005 inch clear protective Mylar film between the tube and the paper surface. In the plane of the paper, the line of light is in the order of 0.010 inch wide and 4 inches long; the spot travels the 4-inch distance in about 50 μsec. A modified P11 phosphor is used.

The exposure characteristics of the paper were studied in the device using actual tube exposure, so that sensitization could be optimized with respect to the spectral output of the phosphor. This was done by mounting an electrometer probe on the device and plotting the surface potential as a function of the beam current of the cathode-ray

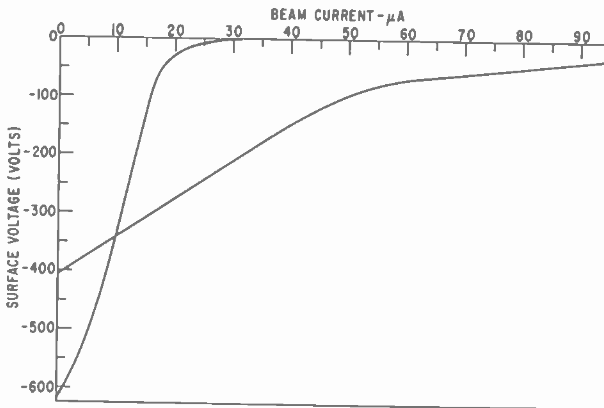

Fig. 7—Surface voltage vs. beam current as influenced by different dispersion methods.

tube. Typical sensitivity curves are shown in Fig. 7 for two experimental papers. Paper coating formulations were sought that yielded high initial surface potential and zero surface potential at low beam currents. Complete exposure coincides with zero surface voltage and gave a means for calibrating our exposure of a given paper during the reversal toning studies.

Liquid Reversal Toning

During the early stages of operation of the processing device, an external electric field, due to corona interaction as described earlier,

was not recognized as being present during toning. Considerable variation in print quality was experienced with different papers and with various corona charger voltage settings of the high-voltage power supplies. Once the corona interaction was recognized and the corona chargers were adjusted to reduce the interaction, reproducible reversal development was obtained by applying an adjustable known external electric field across the paper and the toning liquid during the development interval.

A study was initiated in an attempt to understand liquid reversal toning of ZnO–resin coated paper. In order to obtain quantitative information, an electrometer was attached to the device so that surface potentials could be measured. The potential applied between the back of the paper and an electrode immersed in the toner was also measured. In the study, both the steady-state and transient currents flowing in the development electrode were observed.

From this study, an equivalent circuit was derived that closely follows the behavior of the paper and toner under the action of an external field during development. The equivalent circuit has led to a better understanding of the transient nature of the reversal toning process. It has helped to emphasize the time-dependent aspects of reversal toning and its interdependence on the charge decay and charge uniformity on the surface as it proceeds through the liquid toning region.

In the development of both direct and reverse electrophotographic images, energy is expended during development. With no bias electrodes, the energy is obtained from that stored in the charged regions and should be roughly proportional to the surface area of the charged regions, others factors being equal. The energy is expended in moving charged toner particles either through a viscous carrier fluid or by stripping them from a solid carrier. During the development process, electrical current flows between the toned side of the photoconductive insulating layer and the opposite side of the layer either through the external circuit or through conductive paths existing as conducting imperfections, which extend through the bulk of the layer from one side to the other, or as conducting regions created where the layer is exposed to light.

In the case of direct development, no toning difficulty is experienced with the energy balance provided the layer can be charged to a sufficiently high potential while providing the necessary front to back electrical connections at the time of development.

In the case of reversal development, depending on the ratio of the charged to discharged areas, the energy remaining after exposure

may be insufficient to obtain complete development. In the extreme case of attempting the reversal development of a sheet of uncharged electrophotographic paper by simple immersion in toning fluid, no development at all occurs. Effective reversal toning for all ratios of charged to uncharged areas requires the use of an additional energy source for development. The energy difference can be supplied from an external electrical source by means of electrodes connected to the toning fluid and one side of the electrophotographic layer. Such an arrangement is shown in Fig. 8.

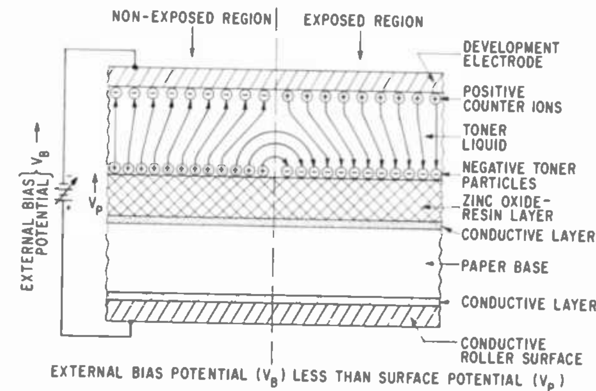

Fig. 8—Toning with external electric field.

Ideally, in reversal toning, no energy need be extracted from the charged areas when the external bias potential equals the potential across the layer. This results in a field-free region in the toning fluid. In practice, this can not be achieved due to the necessary toning electrode spacing and laterial current paths in the toning fluid at the edges separating the charged and discharged regions. The current paths are introduced intentionally with exposure or exist as inherent layer imperfections or charge non-uniformities introduced during charging as discussed previously.

The reversal toning solutions considered here are electrically neutral, and consist of negative toner particles with an equal number of positive counter-ions. During the toning process, there is a simultaneous deposition of each charged species on the oppositely charged electrode. The current in the toner represents the drift of negative toner particles to regions of greatest positive potential.

Considerable data was taken on a commercial electrophotographic paper, designated #A, which provided means for developing our

measuring techniques. During this time, coatings were being made at the Laboratories aimed at low background density and high image density. A representative coating of the later type is #B, which exhibits acceptable light sensitivity, low background density, non-critical adjustment of bias potential, and high image density.

A comparison of reflection density vs. bias potential for papers #A and #B is shown in Fig. 9. From this plot, one can see the difference between the two papers in terms of image quality for black-and-white prints.

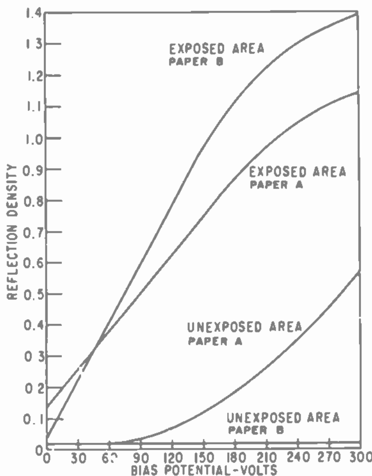

Fig. 9—Reflection density vs. bias potential.

In order to simplify our experimental analysis of the toning process, two conditions that correspond to high contrast images were chosen for our initial study. These correspond to fully charged unexposed areas and areas exposed just sufficiently to reduce the charge to zero. Intermediate exposures leading to continuous-tone production capabilities of various papers were also investigated, but are not reported here.

From the experimental data, it appears that the behavior of the photosensitive paper in the reversal mode of printing using an external electric field during development can be represented by the equivalent circuit shown in Fig. 10. The equivalent circuit is suggested for the following reasons:

1. Essentially linear relation of surface potential of unexposed areas after emerging from development unit as a function of development

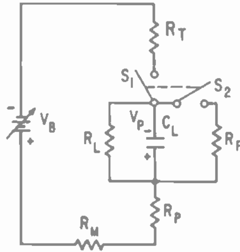

Fig. 10—Equivalent circuit of ZnO–resin coated paper and liquid toner during reversal toning with an external potential.

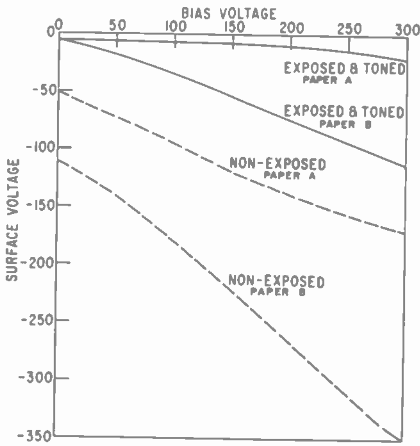

Fig. 11—Surface potential of electrophotographic papers after emerging from toner vs. bias potential.

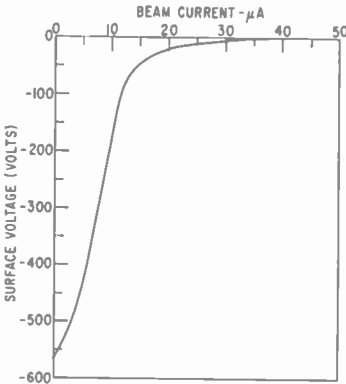

Fig. 12—Charge decay vs. beam current (paper #B).

voltage (bias) as shown in Fig. 11. Fig. 11 is a plot of surface potential in the exposed and nonexposed areas versus bias voltage.

2. Essentially linear relation of surface potential of exposed areas after emerging from development unit as a function of development voltage as shown in Fig. 11. We have observed a recharging of the layer with deposition of toner. The layer was exposed to light from a thin window CRT with a beam current of 37.5 μA, which corresponds to the light needed to completely discharge the #B layer as shown in Fig. 12.
3. Studies of the transient current flow during development shown in Fig. 13, (a) through (i), indicate that during development, negatively charged toner particles move from the paper to the development electrode and constitute a current flow in the external circuit, tending to discharge the layer if the potential of the development electrode is less than that of the surface of the layer with respect to the contact made to the back of the paper by the metal roller over which it passes. This is not only seen from plots of the transient current but also as a toner deposit on the development electrode. When the potential of the paper is less than the external bias, the toner current is in the direction of the paper.

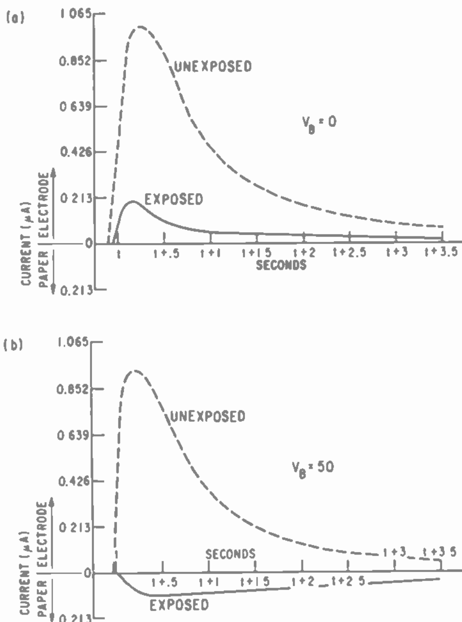

Fig. 13(a-b)—Toner current versus time (paper #B): (a) $V_B = 0$ and (b) $V_B = 50$.

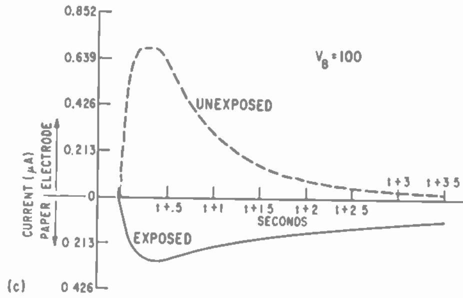

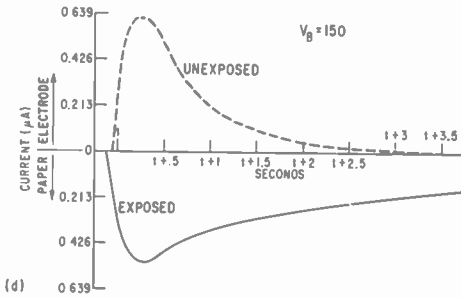

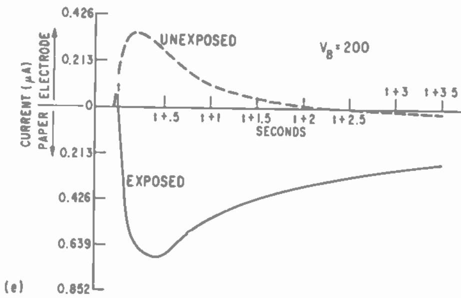

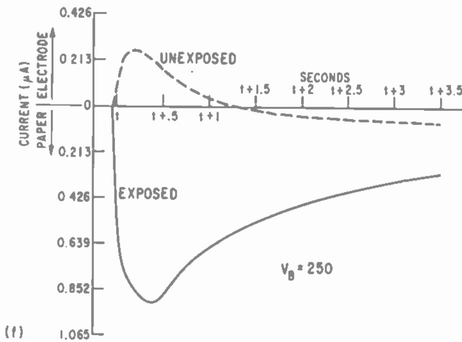

Fig. 13(c-f)—Toner current versus time (paper #B): (c) $V_B = 100$, (d) $V_B = 150$, (e) $V_B = 200$, and (f) $V_B = 250$.

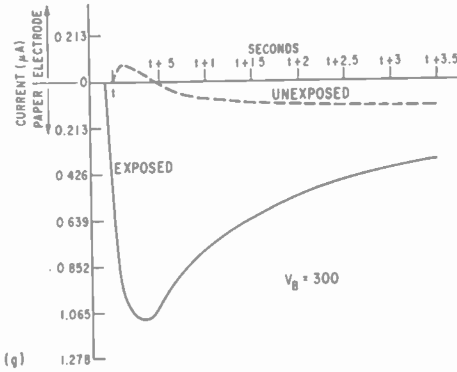

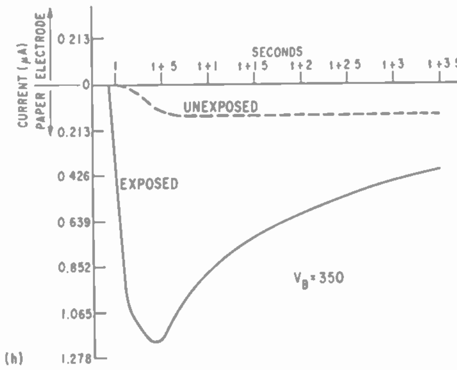

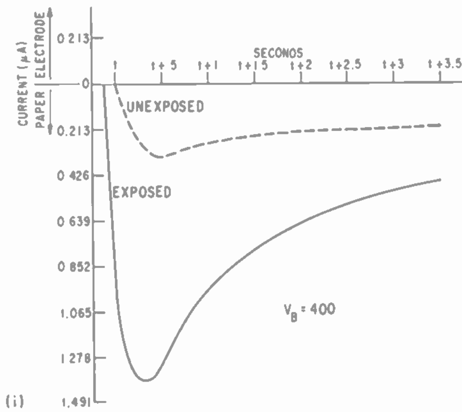

Fig. 13(g-i)—Toner current versus time (paper #B): (g) $V_B = 300$, (h) $V_B = 350$, (i) $V_B = 400$.

In the equivalent circuit, the ZnO–resin layer before it is contacted by the toning fluid is represented by the charged capacitor C_1 shunted by the light responsive resistor R_1. At the instant the toner contacts the ZnO–resin surface, switches S_1 and S_2 close. R_f represents conductive paths through the layer either as inherent defects, corona charger induced defects such as breakdown spots, or solvent action of the toner carrier on the coating resin. R_t represents the toner resistance and is dependent on toner composition. R_p represents the base paper resistance. In order to measure the transient currents flowing in the external bias circuit, a small resistor R_m can be inserted and connected to a fast response display such as an oscilloscope. Values for the above parameters are given in Ref. (5).

When either a charged or discharged area is contacted by the toner, a transient current can be observed in the external circuit. The curves shown in Figs. 13(a) through (i), are similar to the charging and discharging of an RC network. The initial rounding of the curves is due to the experimental procedure used. The toner was mechanically pumped against the surface of the paper. Instantaneous electrical contact could not be made.

Figs. 13(a) through (i), shows the effect of increasing the external bias potential for a uniformly processed sample.

The layers were first charged to approximately 600 volts negative and then either exposed or unexposed before being brought in contact with the toning fluid with various external biases applied. When the external bias is less than the surface potential of the layer, the negative toner particle current is toward the development electrode. When the external bias is greater than the surface potential, the current is toward the paper.

Although an attempt was made to obtain complete exposure, Fig. 13(a) appears to indicate that some residual potential after exposure was present in the zero bias case shown.

The curves of Figs. (13(d) through (g), show a current reversal during the measuring interval. The current transient crosses the axis in shorter and shorter times as the bias is raised. In effect, the transient current provides a means for dynamically observing toner deposition. The upper curve of Fig. 13(d) indicates that, at 150 volts bias, the maximum development time that can be tolerated before the toner starts being deposited in the unexposed areas is 3.5 seconds. By selecting a shorter development interval, the external bias can be raised before toner begins to be deposited in the unexposed areas. Fig. 13(g) indicates that, with this paper and toner, the development time of 0.5

second and 300 volts bias is the lower bound on development interval and the upper bound on the bias respectively.

The data of Figs. 13(a) through (i), shows that the development time interval for externally biased reversal development and the bias potential for maintaining toner rejection from background areas are intimately related. Further, maximum image density must also be realized in the specified time interval determined by toner deposition in background areas. The area under the current curve for exposed paper is related to the quantity of toner deposited and should be directly related to the product of the number of toner particles and the charge per particle.

The decay of current during the toning of the exposed area indicates the build-up of a blocking contact in the toned areas. The blocking contact is further indicated by the surface voltage measured with a probe and plotted in Fig. 11 for exposed and toned areas. The potential existing on the surface after toning can be brought to zero by exposing the toned area to a bright light.

Imaging Materials

Several of the requirements of the imaging materials—the paper and the developer—intended for use in the Homefax-type of printer have been mentioned in the preceding discussion. The various essential characteristics are summarized and elaborated upon in more detail below.

ZnO-Resin Paper

It is well known that the image that will be obtained depends upon the two main structural components of the sheet—the substrate and the electrophotographic layer or coating. However, the Homefax system required a combination of characteristics not found in any one of the many office copier papers checked. These characteristics are described below.

Substrate

Probably the most important requirement is sufficiently high bulk electrical conductivity (conductivity through the thickness of the sheet) so that enough current flows at the developing site to deposit toner uniformly in large areas intended to be filled in completely. Only base paper manufactured by a special process[7] has been found usable. The paper conductivity preferably should not be function of the moisture

content of the paper because the moisture content depends upon the ambient relative humidity, which may vary considerably over a period of time. At the same time, the substrate should not have an electrically "floating" layer through which current can flow from the charger to the developing site and cause the extraneous deposition of toner. In addition, the solvent barriers coating normally applied to these substrates should be effective enough to prevent solvent "strike-through" (penetration of zinc oxide coating mix vehicle through pinhole size areas), which cause the zinc oxide coating to develop microscopic pimples as it dries. These pimples have an oxide to resin binder ratio different from that of the surrounding coating, and this results not only in a different charge acceptance in the pimple, but also in different electrical conductivity through the coating and the substrate in the pimple site. This, in turn, may result in extraneous deposition of toner during development.

Also desirable is a smooth substrate with little or no paper fiber structure. Such structure may result in an Electrofax coating that mechanically traps toner particles in unwanted areas.

Photoconductive Coating

A fundamental requirement of any electrophotographic coating is that its spectral response match the spectral output of the exposure source. Because office-copier papers are generally intended for use with incandescent lights, they lack sensitivity to the rather narrow-band output of the thin-window CRT phosphor.

The spectral sensivity of zinc oxide coatings is generally adjusted by absorbing certain dyes onto the ZnO particles.[8,9] Fluorescein disodium salt was the only dye known that would sensitize the ZnO close to the spectral emission of the modified P-11 phosphor. The degree of sensitization was governed by compromising between the degree of off-white color acceptable in the final document or print and the maximum beam current that could be used, together with the paper speed through the machine.

In the course of making coatings, it was observed that the sensitivity (expressed as beam current required to reach zero surface voltage, not spectral sensivity) was governed to a significant extent by the ZnO dispersion technique that had been utilized in making the coating mix. Those dispersion techniques that tended to least encapsulate the ZnO particles produced the coatings in which the surface voltage could be most quickly reduced to zero by exposure to light.

The curves in Fig. 7 illustrate how the zinc oxide dispersion method

used in preparing the coating mix affects the sensivity of the ZnO–binder layer. The ZnO dispersion method used in preparing the coating, that accepts a high surface voltage (620 volts) and requires a beam current of only 30 μA to discharge it to zero, has very little tendency to encapsulate the ZnO particles with resin binder. On the other hand, the ZnO dispersion technique used in preparing the coating, that accepts a surface voltage of just over 400 volts and requires well over 90 μA to discharge it to zero, tends to throughly wet and encapsulate the ZnO particles with resin binder. Encapsulation of the ZnO particles with resin is believed to electrically insulate the particles from each other.

High charge acceptance (600 volts or higher) is another characteristic of the ZnO coating regarded to be essential for obtaining high quality images. A high charge that is retained through the developing period repels developer particles in nonexposed areas of the image, thus producing clean background. The retention of the charge in the developing liquid is a function of the solubility of the resin binder in the developer liquid and the degree of encapsulation of the ZnO particles by the resin binder. The encapsulation of the ZnO, in turn, is governed by the ZnO-to-resin ratio and the method by which the dispersion is prepared.

Probably the most vexing problem encountered in electrophotographic imaging is the presence of pinpoint-sized areas on the zinc oxide coating that, prior to development, are usually undetectable. However, in direct positive development, they appear as tiny white specks in areas that should be solidly toned. In reversal development, these same areas become evident as extraneous deposits of developer pigment in areas that should be completely free of toning. These areas (referred to as pinholes) are attributed to several causes (some unknown). Two remedies have reduced their number substantially: (1) the use of certain selected zinc oxides,[10] and (2) the zinc oxide dispersion technique used in preparing the coating mix.

Developer Liquid

To elaborate upon the intricacies of reversal developer formulation is beyond the scope of this discussion,[11] but it should be said that the prime consideration in formulating a liquid developer for home use was safety. The liquid had to be nonflammable and no more toxic than the various substances generally used in the home and still develop high-quality images. At the same time, the developer liquid had to

fulfill other essential requirements, namely:

1. Be fast drying and self-fixing so that the developed print could be handled within seconds after it had been made.
2. Have high developing capacity, that is, be capable of developing a large number of prints of uniform quality per given volume of liquid so that replenishment or replacement of the developer is reduced to a minimum.
3. Be low cost.

Acknowledgments

The authors wish to thank L. Korsakoff for assisting in coating the paper, G. L. Bradshaw for obtaining the experimental data during our exposure and toning studies, and E. C. Hutter for his contributions in the development of the equivalent circuit concept. Further, we wish to acknowledge the support of D. A. Ross during the course of the work.

References:

[1] W. D. Houghton, "Homefax—A Consumer Information System," Fall Technical Conf., SMPTE, N.Y., N.Y., Oct. 6, 1970.

[2] Olden, R. G., "A Thin Window Cathode-Ray Tube for High-Speed Printing with Electrofax," **RCA Review**, Vol. XVIII, No. 3, Sept. 1957.

[3] Olden, R. G., "High Speed Printing on Electrofax," **RCA Review**, Vol. XXII, No. 3, Sept. 1961.

[4] M. Leedom, U.S. Patent 3507252.

[5] Hutter, E. C., Giaimo, E. C., "Charge Transfer in Electrofax Development by Reversal Liquid Toning," **Photographic Science and Engineering**, Vol. 14, No. 3, May-June 1970.

[6] W. Bruce's Report on Homefax Electronics, **RCA Review.** Submitted for publication.

[7] Lucken, T. C., U. S. Patent 3,293,115 (1966).

[8] Greig, H. C., U. S. Patent 3,052,540 (1962).

[9] Giaimo, E. C., "A Spectrophotometric Investigation of Dye-Sensitized Photoconductive Zinc Oxide-Resin Layers Used in the Electrofax Process," **RCA Review,** Vol. XXIII, No. 1, March 1962.

[10] Unpublished results of E. C. Giaimo and S. Larach.

[11] Lozier, G. S., "Liquid Toners for Reversal Development of Electrofax Layers," Preprints of Paper Summaries, 23rd Annual Conference on Photographic Science and Engineering, May 1970.

High-Level Current Gain In Bipolar Power Transistors

J. Olmstead, W. Einthoven, S. Ponczak, and P. J. Kannam
RCA Electronic Components, Somerville, N. J.

Summary—This paper discusses the phenomena of base widening and emitter-current crowding as they affect the high-level, low-voltage current gain in bipolar power transistors. Base widening is analyzed by solving for the ohmic and space-charge widths in the collector region as functions of collector-current density, collector resistivity, and the applied collector-to-base voltage. Emitter-current crowding is handled by developing expressions for an effective emitter width under which injection is reasonably uniform. Two expressions result for high- and low-injection modes of operation. Base-conductivity-modulation effects are included in the analysis. It is shown that the product of collector current I_C and current gain h_{FE} for non-crowded n^+-p-n^+ (or p^+-n-p^+) structures is given by $h_{FE}\, I_C =$ constant. When severe emitter-current crowding exists, the product approaches $h_{FE}\, I_C^2 =$ constant.

In n^+-p-n-n^+ (or p^+-n-p-p^+) devices, base-widening effects are described by the equation:

$$h_{FE} \approx \frac{K_E}{J_C\left(W_{BM} - \dfrac{V_{CB}}{J_C \rho_{n^-}}\right)^2}$$

where K_E is a proportionality constant, J_C is the collector-current density, W_{BM} is the total width of the base and n^- regions, V_{CB} is the collector-to-base voltage, and ρ_{n^-} is the resistivity of the n^- region.

As a test of the validity of the theory, experimental structures were fabricated and the collector-current–current-gain characteristics were measured. Special ring-emitter geometries of varying widths were employed to evaluate current-crowding effects. The agreement between analysis and experiments is excellent for the base-widening theory and is within 20% for emitter-current crowding.

Introduction

A bipolar power transistor is designed to deliver appreciable power to a load with a reasonable input drive current at low collector-to-emitter voltages so that a minimum of power is dissipated internally. The high-level current gain at low collector-to-emitter voltages must, therefore, be optimized, consistent with other major parameters such as voltage, power, second breakdown, switching speed, and cost requirements. To date, this optimization has been accomplished primarily by empirical trial-and-error techniques. Theory has been used to provide directional guidelines, rather than absolute design values, because power transistors seldom operate in the well analyzed low-injection mode. In addition, they are particularly sensitive to emitter-current-crowding (emitter-debiasing or emitter-pinchout) and base-widening effects, and these phenomena are difficult to analyze theoretically.

High-injection-level phenomena have been analyzed by Webster[1] and Fletcher.[2,3] Essentially, conductivity modulation of the base results in an increased base-defect current and decreased emitter efficiency. As the base is conductivity modulated, drift fields established by doping gradients are swamped out and the net result is approximately a doubling of the injected-carrier diffusion constant.

Emitter-current-crowding effects are caused by the imperfect (resistive) character of the base region beneath the emitter. The resistance beneath the emitter allows the emitter–base junction to be more forward biased at the edges than at the center. Although several authors have analyzed this phenomenon,[3-6] most of the analyses were based on the assumption of an ideal transistor, which severely limits the applicability of the resulting models for device design.

Base widening is a phenomenon that results from large injected-carrier densities in the collector–base depletion region. Early[7] and Kirk[8] treated the effect, assuming a saturated-carrier velocity. Middlebrook[9,10] considered both unsaturated and saturated velocity effects. The influence of base widening on the deterioration of the saturation characteristic was recognized by Hahn.[11] Base widening has also been analyzed by computer techniques.[12-14]

In this paper, the phenomena of base widening and emitter-current crowding are treated as they affect the high-level, low-voltage current gain in power transistors. Because the derivations are not rigorously correct, the results are only approximate; their value lies in their simplicity and ease of application. First, a general expression relating current density and current gain at high injection levels is developed. Base widening is then treated, and the general expression is modified

for the varying base width as a function of collector-to-base voltage and collector-current density. Finally, an analysis of emitter-current crowding is presented that yields two equations for an effective emitter width, the applicable equation being determined by the injection-level condition.

The paper also presents experimental data supporting the theory. In general, the agreement between theory and practice is satisfactory. In many cases, the verification is well within the experimental error of the structure and resistivity determination.

The analysis and the experimental work were performed on n-p-n devices, and all of the equations presented are in n-p-n nomenclature. With appropriate changes, however, the theory is also applicable to p-n-p structures.

Current-Gain Fall-Off at High Currents

The following section develops an approximate, but extremely convenient, equation relating current gain and collector current in the fall-off region that applies to a non-current-crowded transistor free of base widening. The development is based on Webster's work.[1] The starting point is the dc relationship between the common-emitter current gain h_{FE} and the common-base current gain h_{FB}, as follows:

$$h_{FE} = \frac{h_{FB}}{1 - h_{FB}} = \frac{\beta^* \gamma}{1 - \beta^* \gamma}, \qquad [1]$$

where β^* is the base transport factor and γ is the emitter-current injection efficiency. Space charge and surface recombination currents have been neglected. The base transport factor β^* and the emitter-efficiency factor γ may, in turn, be expressed as follows:

$$\beta^* = 1 - \delta \qquad [2]$$

$$\gamma = 1/(1 + \xi) \qquad [3]$$

where δ is the base recombination defect factor and ξ is the base injection defect factor. Substitution of these relationships in Eq. [1] yields the following expression for h_{FE}:

$$h_{FE} = \frac{1}{\delta + \xi} - \frac{\delta}{\delta + \xi}. \qquad [4]$$

If it is assumed that the transistor has perfect injection efficiency ($\xi = 0$) and a beta of ten, the base defect factor has a maximum value of 0.09. In the case of a transistor with less than perfect injection efficiency and the same gain, the base defect factor becomes even smaller. Thus, a very good approximation of h_{FE} is given by

$$h_{FE} = \frac{1}{\delta + \xi}. \qquad [5]$$

The base defect term δ is given by

$$\delta = \frac{W_B{}^2}{2(L_{nB}')^2}, \qquad [6]$$

where W_B is the base width, and L_{nB}' is the effective diffusion length of electrons in the base.

The base injection term ξ is given by

$$\xi = \frac{\dfrac{qp_E D_{pE}'}{L_{pE}'}}{\dfrac{qn_B D_{nB}'}{W_B}}, \qquad [7]$$

where q is the electron charge, p_E is the density of holes in the emitter, n_B is the density of electrons in the base, D_{pE}' and D_{nB}' are the effective diffusion constants of holes in the emitter and electrons in the base, respectively, L_{pE}' is the effective diffusion length of holes in the emitter, and W_B is the base width. This equation can be rearranged as follows:

$$\xi = \left(\frac{D_{pE}'}{D_{nB}'}\right)\left(\frac{Q_{BO}}{Q_{EO}}\right), \qquad [8]$$

where Q_{BO} and Q_{EO} are the charges due to ionized impurities in the base and emitter, respectively, at equilibrium.

Eq. [8] shows that ξ is simply the ratio of injection capabilities of the base (to inject into the emitter) and the emitter (to inject into the base). These capabilities are directly related to the available majority-carrier charges (Q_{BO} and Q_{EO}) within the appropriate length on both sides (W_B and L_{pE}') and their abilities to move by diffusion (D_{nB}' and

D_{pE}'). Eq. [8] can be used to show the effect of conductivity modulation. When an electron is injected into the base, a hole also flows into the base to preserve local charge neutrality. As a result, the majority-carrier charge Q_B is increased. Similarly, a hole from the base injected into the emitter increases Q_E. In the presence of conductivity modulation, therefore, the ξ term is given by

$$\xi = \left(\frac{D_{pE}'}{D_{nB}'}\right)\left(\frac{Q_{BO}+\Delta Q_B}{Q_{EO}+\Delta Q_E}\right), \quad [9]$$

where ΔQ_B and ΔQ_E are the incremental changes of total charge in the base and emitter, respectively. In most cases, $Q_{EO} \gg \Delta Q_E$; therefore, Eq. [9] becomes

$$\xi = \left(\frac{D_{pE}'}{D_{nB}'}\right)\left(\frac{Q_B+\Delta Q_B}{Q_{EO}}\right). \quad [10]$$

The change of total charge in the base ΔQ_B is easily related to the collector current I_C, as follows:

$$I_C = \frac{\Delta Q_B}{\tau_B} = \frac{2D_{nB}'\Delta Q_B}{W_B^2}, \quad [11]$$

where τ_B is the transit time in the base.

Substitution of Eqs. [6], [10], and [11] in Eq. [5] provides the following expression for h_{FE}:

$$h_{FE} = \frac{1}{\dfrac{W_B^2}{2L_{nB}'} + \left(\dfrac{D_{pE}'}{D_{nB}'}\right)\left(\dfrac{Q_{BO}}{Q_{EO}}\right) + \left(\dfrac{D_{pE}'}{D_{nB}'}\right)\left(\dfrac{W_B^2 I_C}{2D_{nB}'Q_{EO}}\right)}. \quad [12]$$

In the current-gain fall-off region, this expression reduces to

$$h_{FE} \approx \frac{1}{\dfrac{D_{pE}'W_B^2 I_C}{2(D_{nB}')^2 Q_{EO}}}, \quad [13]$$

or

$$h_{FE} I_C = \frac{2(D_{nB}')^2 Q_{EO}}{D_{pE}' W_B^2}. \qquad [14]$$

Eq. [14] is valid only for high-injection-level conditions. Under these conditions, the electron injection from the emitter into the more lightly doped base is significant and causes the effective diffusion constant D_{nB}' to become $2D_{nB}$. In contrast, the smaller hole injection from the base into the heavily doped emitter has a negligible effect on D_{pE}'. Thus, if the base width W_B remains constant, the product of collector current and current gain is a constant. If it is assumed that the injected electron current does not diverge in flowing to the highly doped collector, Eq. [14] can be rewritten in terms of collector-current density J_C and an experimentally determined constant K_E, as follows:

$$W_B^2 h_{FE} J_C = K_E. \qquad [15]$$

Eq. [15] is used as the basis for subsequent work.

Base Widening

Bipolar power transistors of n+-p-n−-n+ variety suffer a degradation in current gain at high currents as the collector voltage is reduced and approaches the true saturation voltage. This condition is illustrated in Fig. 1. Because the degradation causes a saturation-like effect at higher-than-normal saturation collector voltages, the degraded-beta region is referred to as the quasi-saturation region. The condition illustrated in Fig. 1 is a severe case and is characteristic of devices with wide, lightly doped n− regions.

The quasi-saturation region arises because the base widens into the lightly doped collector n− region at low collector voltages and high collector currents. As the base widens into the collector n− region, injection efficiency γ and base transport factor β^* deteriorate and decrease current gain.

The collector-to-base voltage profile of an n+-p-n−-n+ structure is illustrated in Fig. 2. A small current flow J_1 through this region has three effects. First, the mobile carriers (electrons) on the base side of the collector depletion region act to terminate the collector field so that fewer acceptor sites are uncovered. The second effect of the mobile electrons moving through the depletion region is to modify the depletion region on the collector side. In this case, the mobile charge subtracts from the fixed-donor-site charge and, therefore, causes the

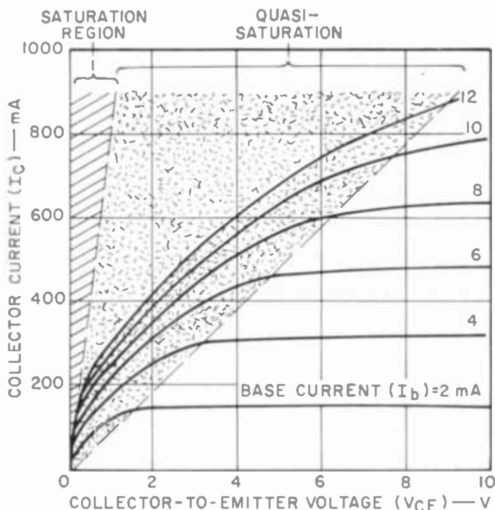

Fig. 1—Illustration of quasi-saturation in an n+-p-n−-n+ transistor.

depletion region to expand in order to uncover the required terminating charge. The third effect of the current flow in the collector of the transistor is to introduce an ohmic voltage drop in the undepleted portion of the collector n− region. Because this voltage subtracts from

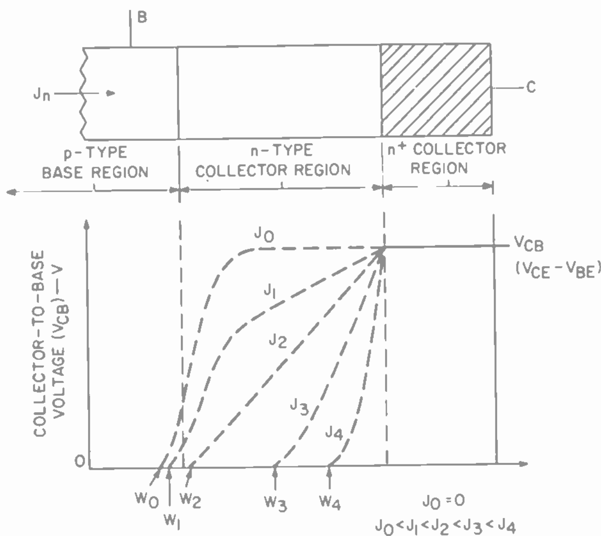

Fig. 2—Base-collector voltage distribution for various collector-current densities J_n.

the applied collector-to-base potential, less voltage is available for the depletion region. As a result of the current flow J_1, the base moves somewhat toward the collector and begins to widen. If the current is increased to a larger value J_2, the potential profile is markedly changed. Almost the full collector-to-base voltage is dropped across the ohmic n^- region and the base widens to approximately the metallurgical junction.

If the collector-current density is further increased, the base widens rapidly, as illustrated in Fig. 2 by the curves for current densities J_3 and J_4. In these situations, the ohmic drop in the full n^- region is larger than the applied collector-to-base voltage. Because this condition is impossible, the width of the ohmic n^- region adjusts itself (shrinks) so that the ohmic voltage drop approximately equals the applied V_{CB}. The remaining portion of the n^- region, which abuts the base, does not have any appreciable electric field and, therefore, must possess local charge neutrality (or nearly so). If the electric field is low, the mobile charge density must be high to pass the required current density. The region maintains local charge neutrality with a high electron density by allowing holes from the base to move into the region along with the electrons, which in effect is forward biasing the metallurgical base–collector junction. The metallurgical junction cannot prevent the holes from entering the n^- region because the mobile charge densities are so large that the fixed donor and acceptor densities forming the dipole layer are swamped out.[15] The portion of the n^- region that has a low electric field, a large density of mobile charge, and charge neutrality is really an extension of the base. In the plasma-like region, the carriers move by a combination of drift and diffusion as they do in the base. Furthermore, the potential of the plasma-like region is determined by the potential of the base rather than that of the collector. In effect, a region that was originally a portion of the collector becomes conductivity modulated and serves as an extension of the base.*

An approximate solution for severe base widening can be obtained as follows: First, the widths of the ohmic portion of the n^- region W_o and space-charge region W_{sc}, which matches the ohmic region to the base plasma, are determined, as shown in Fig. 3. The sum of these two regions, when subtracted from the n^--region metallurgical width, yields the width of the extended-base region ΔW_B;

$$\Delta W_B = W_{n^-} - W_{sc} - W_o. \qquad [16]$$

* The definitions of the base and collector used here are functional definitions, rather than metallurgical.

In determining the width of ohmic region, it is necessary to realize that it is a region in which the injected mobile charge density n does not exceed the fixed positive donor-site density N_D, and local charge neutrality is preserved. The collector-current density in the ohmic region is given by

$$J_C = q\mu_n N_D E_o = \frac{E_o}{\rho_{n-}}, \quad [17]$$

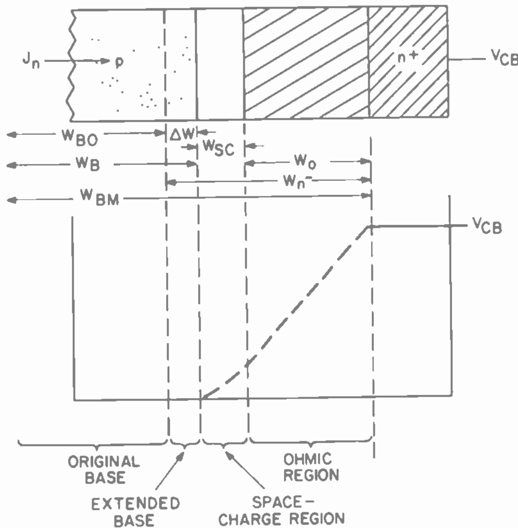

Fig. 3—Diagram illustrating a severe case of base widening ($J_n > J_s$).

where μ_n is the mobility of electrons in the collector and E_o is the electric field in the ohmic n− region. The electric field E_o is thus given by

$$E_o = J_C \rho_{n-}. \quad [18]$$

This electric field must be matched to the low value which exists in the extended-base region; this matching is accomplished by a space-charge region, as discussed in Appendix A.

In most high-voltage power transistors, base widening resulting from the ohmic voltage drop is so dominant that it alone limits the maximum collector-current densities to low values. At low collector-current densities, the voltage drop and the width of the space-charge region are small and a further simplification can be made by totally

neglecting it. In this case, the amount that the base widens is given by

$$\Delta W_B = (W_{n-}) - (V_{CB}/J_C\rho_{n-}) . \quad [19]$$

Despite its simplicity, Eq. [19] predicts the quasi-saturation curves of high-voltage devices quite well. It is important to note that the onset of base widening V_{CB}' is given by

$$V_{CB}' = (\rho_{n-})(W_{n-})(J_C) . \quad [20]$$

This equation indicates that the locus of the critical voltage as a function of collector current is simply the n^--region resistance.

The relationship developed earlier between collector current I_C and current gain h_{FE} (Eq. [15]) can be combined with the base-widening analysis. If the device is free of emitter-current crowding, the constant K_E is given by

$$W_B{}^2 h_{FE} J_C = K_E . \quad [21]$$

The amount of base widening ΔW_B is given by

$$\Delta W_B = (W_{n-}) - (V_{CB}/J_C\rho_{n-}) . \quad [22]$$

Addition of Eq. [22] to the original base width W_{BO} gives

$$W_B = W_{BO} + W_{n-} - (V_{CB}/J_C\rho_{n-}) . \quad [23]$$

Eq. [21] can then be rewritten as follows:

$$\left(W_{BM} - \frac{V_{CB}}{J_C\rho_{n-}} \right)^2 J_C h_{FE} = K_E , \quad [24]$$

where W_{BM} is the sum of the base and n^- regions, as follows:

$$W_{BM} = W_{BO} + W_{n-} . \quad [25]$$

The gain in the quasi-saturation region is thus given by

$$h_{FE} = \frac{K_E}{J_C \left(W_{BM} - \frac{V_{CB}}{J_C\rho_{n-}} \right)^2} . \quad [26]$$

At $V_{CB} \approx 0$, the base width is W_{BM}, and h_{FE} becomes

$$h_{FE} \approx \frac{K_E}{W_{BM}^2 J_C}. \qquad [27]$$

The transistor then acts as an n+-p-n+ structure with a wide base.

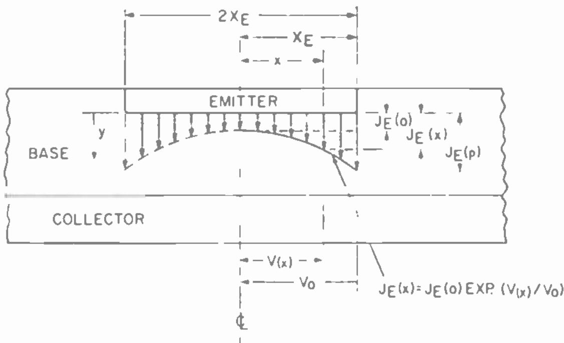

Fig. 4—Diagram illustrating injection distribution beneath the emitter.

Emitter-Current Crowding

The tendency for the emitter current to be concentrated near the emitter edges is significant in most power transistors and is caused by the voltage drop in the base beneath the emitter, which results in de-biasing at the emitter center.* The effect is most troublesome at high injection levels at which the base injection current is large. An exact solution of the problem is difficult and is complicated by the multiplicity of effects occurring simultaneously (base-width widening, base-conductivity modulation, and non-uniformity of current gain h_{FB} beneath the emitter). Actually, analysis of a severely crowded design is not what is desired. Instead, the device engineer wishes to know how to design a device reasonably free of crowding. Analysis for the latter condition is much simpler and is the approach followed in this paper. As shown in Fig. 4, the emitter-current density $J_E(x)$ is given by

$$J_E(x) = J_E(o) \exp [V(x)/V_o] \qquad [28]$$

* Emitter-current crowding is also known as emitter de-biasing or emitter "pinchout".

where $J_E(o)$ is the emitter-current density at the center of the emitter, $V(x)$ is the voltage in the base beneath the emitter, and V_o has a value of 26×10^{-3} volt at 300°K. For this analysis, a device is defined to be free of current crowding if the maximum value of $V(x)$ is equal to $V_o/2$. Under this condition, the average current density $\overline{J}_E$ is 0.81 times the peak value, J_{Ep} and $J_E(o)$ is 0.6 times the peak value.

Eq. [28] can be expanded (with only the first two terms retained), as follows:

$$J_E(x) = J_E(o)\left[1 + V(x)/V_o\right] \quad [29]$$

In the base region under the emitter, the voltage drop resulting from base current is assumed to be only ohmic, and the base resistivity is initially treated as a general term independent of x. This assumption is possible because the analysis is restricted to a device relatively free of current crowding rather than any device in general. This limitation allows the modulated base resistivity to be included in the final result. Thus, the differential voltage drop in the base is given by

$$\frac{dV(x)}{dx} = \rho_b J_b(x) \quad [30]$$

It can be shown that an elementary transistor contained in a distance dx satisfies the following equation:

$$\frac{dJ_b}{dx} = \frac{1 - h_{FB}}{W_B} J_E(x) \quad [31]$$

Combination of Eqs. [29], [30], and [31] yields

$$\frac{d^2V(x)}{dx^2} = \rho_b \frac{(1 - h_{FB})}{W_B} J_E(o)\left[1 + V(x)/V_o\right], \quad [32]$$

which has the following solution:

$$x = \left[\frac{W_B V_o}{(1 - h_{FB})\rho_B J_E(o)}\right]^{1/2} \cosh^{-1}\left[1 + V(x)/V_o\right]. \quad [33]$$

Substitution of $V(x) = 0.5\ V_o$ into Eq. [33] yields an effective emitter

half-width X_E given by

$$X_E = \left[\frac{W_B V_o}{(1 - h_{FB})\rho_B J_{Ep}}\right]^{1/2}. \qquad [34]$$

The effective emitter half-width carrying the average emitter current then becomes

$$X_E = \left[\frac{W_B V_o}{(1 - h_{FB})\rho_B\, 1.23\, \bar{J}_E}\right]^{1/2}, \qquad [35]$$

or

$$X_E = 0.9\left[\frac{W_B V_o}{(1 - h_{FB})\rho_b \bar{J}_E}\right]^{1/2}. \qquad [36]$$

Eq. [36] can be rewritten

$$X_E = 0.9\left[\frac{V_o}{\rho_{BS}\bar{J}_B}\right]^{1/2}, \qquad [37]$$

where ρ_{BS} is the base sheet resistance. Eqs. [36] and [37] are applicable for low-level-injection conditions. If these equations are modified to include base-conductivity modulation, the results should be valid for high-level-injection conditions. Eq. [36] can be rewritten

$$X_E = 0.9\left[\frac{W_B V_o h_{FE}}{\rho_B \bar{J}_E}\right]^{1/2}. \qquad [38]$$

Under conditions of heavy base-resistivity modulation, the contribution of ionized impurities may be neglected in the base; the average base resistivity ρ_B can then be expressed

$$\rho_B = \frac{1}{q(\mu_n n + \mu_p p)} = \frac{0.7}{q\mu_n n(\text{average})}, \qquad [39]$$

where $n = p$ and $\mu_n = 2.5\mu_p$, and it is safe to assume that over a large portion of the base region the current satisfies the following condition:

$$J_E = 2qD_{nb}\frac{dn}{dy} \quad [40]$$

or

$$J_E \approx \frac{2qD_{nb}n_b(o)}{W_B}. \quad [41]$$

The average density of electrons in the base n_b is then given by

$$n_b \approx \frac{J_E W_B}{2qD_{nb}} \quad [42]$$

so the average resistivity ρ_B is,

$$\rho_b \approx \frac{2.8\ V_o}{J_E W_B}. \quad [43]$$

Substitution of Eq. [43] into Eq. [38] yields the following expression for the effective emitter half-width:

$$X_E \approx 0.54 W_B (h_{FE})^{1/2} \quad [44]$$

Eqs. [44] and [15] may be combined to show that (see Appendix B) the current-gain fall-off exceeds a −1 slope and approaches a −2 slope under severe current-crowding conditions.

Experimental Work

As a test of the validity of the theoretical predictions of h_{FE} fall-off, measurements were made on three groups of transistors: (1) single-diffused n+-p-n+ transistors, (2) double-diffused n+-p-p−-n+ transistors, and (3) double-diffused n+-p-n−-n+ transistors. Fig. 5 shows an example of the results obtained on transistors in the first group. These devices had ballasting and an interdigitated emitter geometry and were reasonably free of emitter-current crowding and edge injection. They also had negligible base widening. The measured results agree quite well with the theory, showing the −1 slope predicted. These data were taken by use of pulse technique to minimize thermal effects.

Fig. 6 shows typical results obtained on double-diffused transistors. The simplified theory described in this paper predicts that, at very low

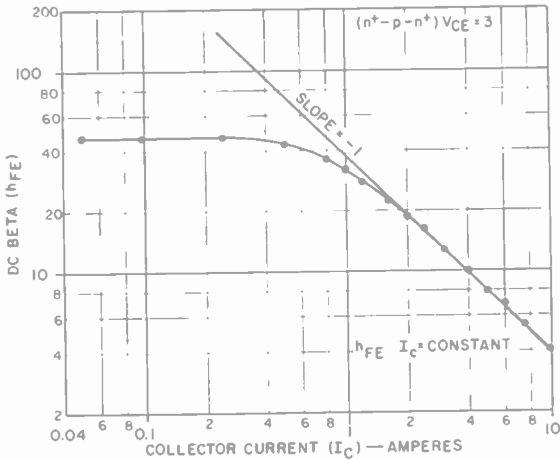

Fig. 5—Gain fall-off in a special single-diffused transistor.

collector-to-base voltages, the base widens to the n−-n+ collector junction. As a result, n+-p-n−-n+ and n+-p-p−-n+ transistors of the same geometry and structural dimensions should behave alike at high currents. Fig. 6 shows that the results on the two types of transistors are similar and that the current-gain fall-off is as predicted.

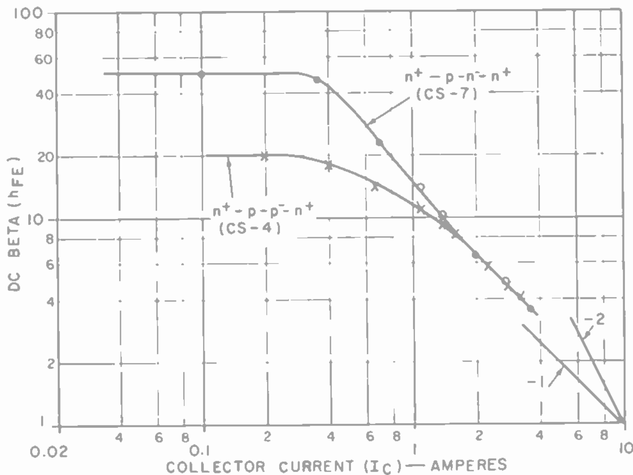

Fig. 6—Comparison of the performance of n+-p-p−-n+ and n+-p-n−-n+ transistors with identical geometry and structural dimensions.

The theory also predicts that the locus of the onset of base widening and quasi-saturation is given by Eq. [20]. Fig. 7 shows curves of collector current in the common-emitter configuration for an experimental high-voltage transistor. In this device, the collector n^{-}-region resistivity and thickness were carefully controlled. The curves show good agreement with the predicted locus at low to medium current densities. Similar observations were made by Hahn.[7] At high current densities, the agreement is less satisfactory because fields in the ohmic region of this particular transistor reach values where the velocity begins to saturate. The use of field-dependent mobilities yields a better agreement.

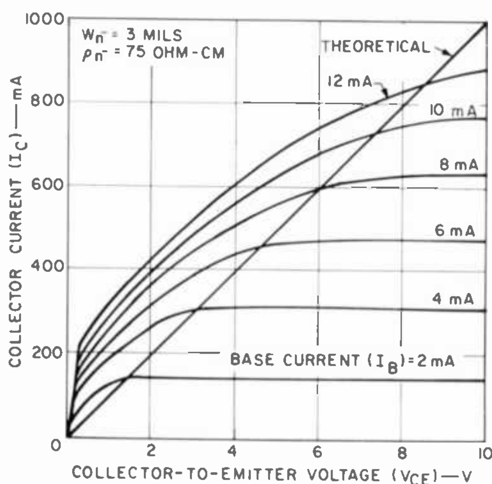

Fig. 7—Onset of quasi-saturation.

Eq. [26] has also been used to predict the beta fall-off for a number of different double-diffused power transistors. Experimental and theoretical results for two of these transistors are shown in Figs. 8 and 9. Because the collector-to-base voltage was held constant in the computations, while the collector-to-emitter voltage was held constant in the experimental measurements, some disagreement is noted at the lower voltages. Better agreement is obtained in Fig. 9, if the following relationship is used:

$$V_{CE} = V_{CB} + V_{BE}. \quad [45]$$

For experimental verification of the theory developed on current

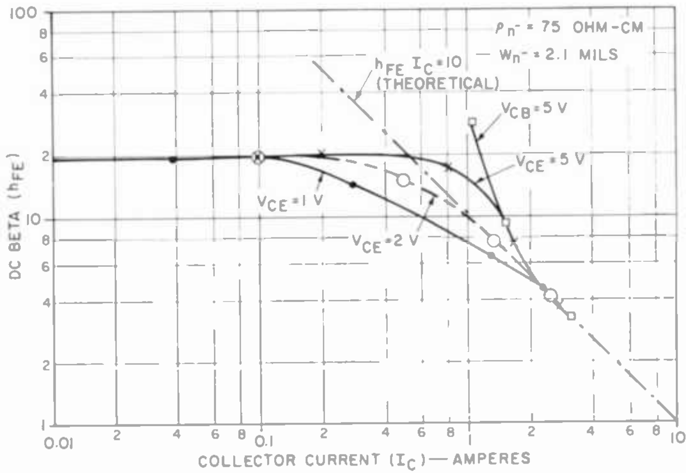

Fig. 8—High-gain fall-off of double-diffused transistor (example 1).

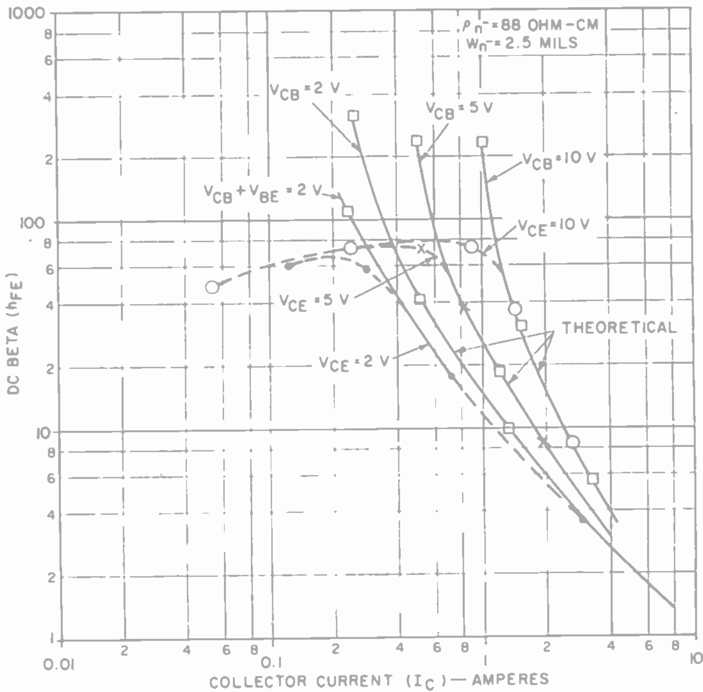

Fig. 9—High-gain fall-off of double-diffused transistor (example 2).

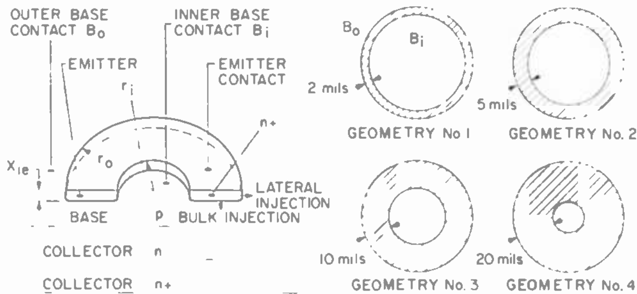

Fig. 10—Current-crowding experimental vehicles.

crowding, four ring-emitter geometries were employed. These four geometries were grouped on the masks, as shown in Fig. 10, so that a given wafer contained groups of transistors of each geometry. The ring-emitter geometry was selected because it allows both direct measurement of the base sheet resistance beneath the emitter and application of base drive to one or both base contacts. Figs. 11 through 14 show typical sets of current-times-current-gain characteristics for the four geometries. Each figure shows the influence of base drive point. The following effects should be noted:

[1] The peak current gain is greatest for the 20-mil-wide emitter and decreases as the emitter width decreases.

[2] Application of base drive to both of the base contacts results in the best high-current performance. The difference is

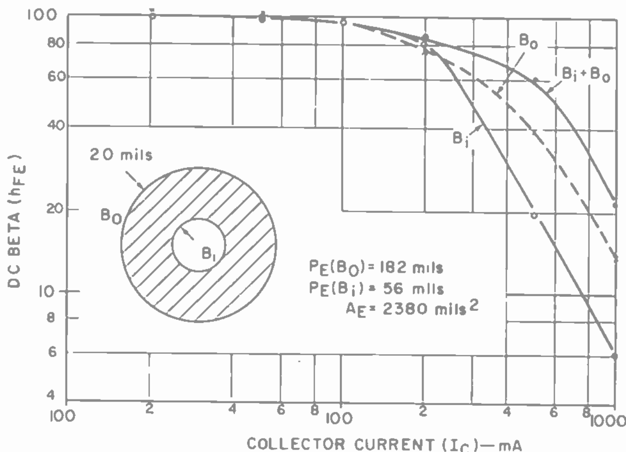

Fig. 11—High-current performance of geometry No. 4 in Fig. 10.

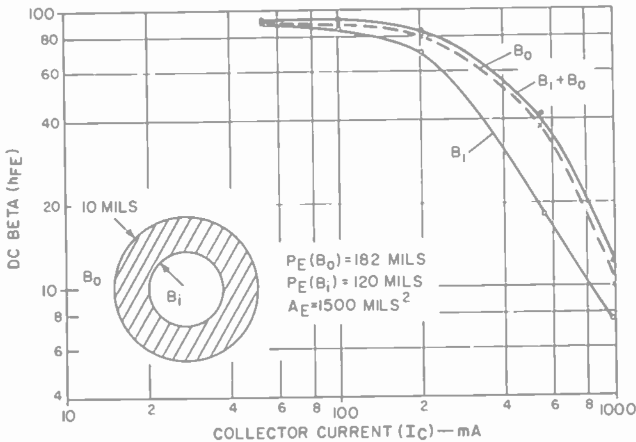

Fig. 12—High-current performance of geometry No. 3 in Fig. 10.

less pronounced as the emitters become narrower. Very little difference in drive points is observed in the 2-mil-wide emitter.

[3] The rate of current-gain fall-off approaches the ideal (−1) slope in the 2-mil-wide emitter. Faster fall-off is observed as the emitter width increases.

The sheet resistance beneath the emitter was measured in a conventional manner. Interestingly, the actual emitter-mask opening sizes, without lateral diffusion correction, had to be used in the calculations to obtain consistent data. For the devices discussed, the measured sheet resistance was 2000 ohms per square.

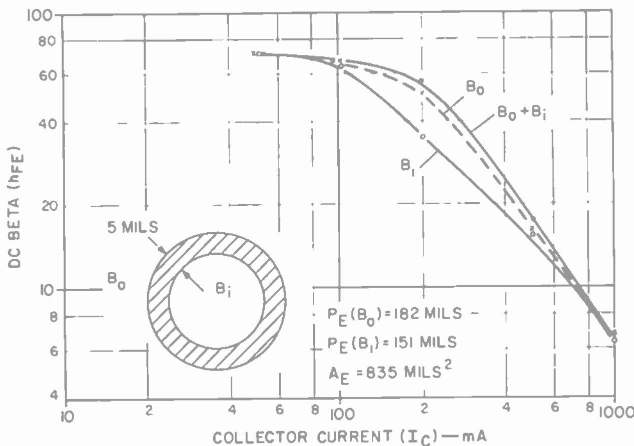

Fig. 13—High-current performance of geometry No. 2 in Fig. 10.

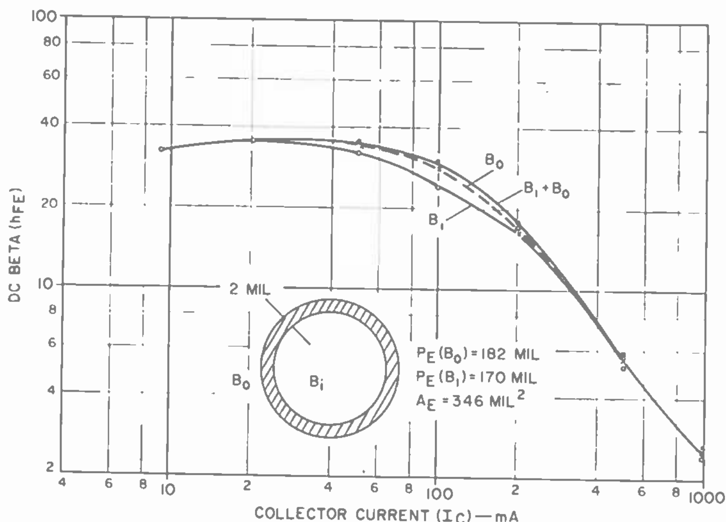

Fig. 14—High-current performance of geometry No. 1 in Fig. 10.

As noted, the peak gain value decreases as the emitters become narrower. This effect is explained as follows: A fraction of the injection from the emitter edge contributes to base current but not to collector current. The situation is illustrated by the diagram in Fig. 10. A simple analysis shows that with uniform injection (at low collector currents) the measured h_{FE} of the device is given by

$$h_{FE} = \frac{h_{FE}(\text{max})}{1 + \dfrac{KP_E}{A_E}} \quad [46]$$

where A_E is the emitter injection area and P_E is the emitter periphery. In this expression, the ratio of the excess edge to useful bulk base current is assumed to be proportional to emitter periphery and emitter width, respectively. The data fit this equation reasonably well when the actual emitter mask opening is used for A_E. From this calculation, the maximum current gain $h_{FE}(\text{max})$ for all of the geometries is 110 and occurs at collector-current densities of approximately 10 amperes per square centimeter. Fig. 15 shows current-gain curves for the four geometries with outer base drive and the edge-injection component removed. If the collector currents in Fig. 15 are divided by the appro-

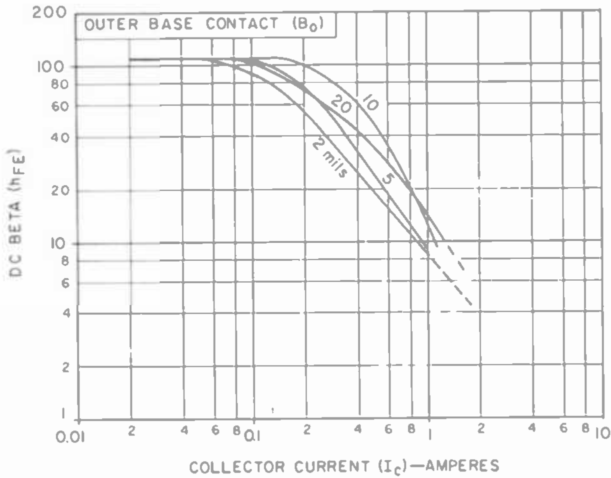

Fig. 15—High-current performance of the four geometries shown in Fig. 10 with a bulk injection component.

priate emitter areas, curves of gain as a function of average collector-current density are obtained, as shown in Fig. 16. These curves clearly show the superiority of the 2-mil-wide emitter geometry. In this geometry, the fall-off slope is (−1) at an h_{FE} of about 50. At h_{FE} values lower than 50, the slope is greater than the ideal (−1).

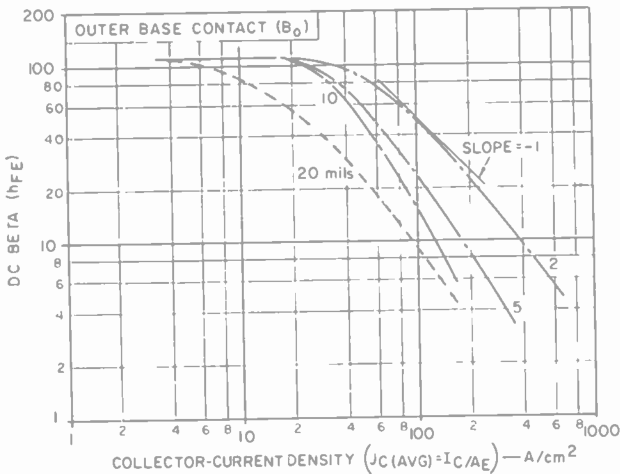

Fig. 16—High-level gain of the four geometries shown in Fig. 10 as a function of collector-current density.

Discussion

The equation developed previously relating current gain and collector current at high injection levels is basic to the base-widening and emitter-current-crowding discussions of this paper. The derivation of this equation is admittedly simplified by the following assumptions. (1) The drift field in the base caused by the doping-impurity gradient is swamped out and replaced by a field that effectively doubles the minority-carrier diffusion constant. This assumption is standard at high injection levels. (2) The drift field in the emitter remains constant and is not affected by injection from the base back into the emitter. This assumption is also standard but should be questioned at very high current levels where the current gain is less than 10. (3) The current flow in the base and collector regions does not diverge. This assumption depends on the dimensions (aspect ratio) of the device under consideration and is usually reasonable for power transistors.

The derived relationship between the collector current and current gain is experimentally substantiated in three different ways. First, the gain fall-off slope of a transistor with reasonably constant base width and emitter-injection area is shown to agree very well with the theory. When the equation is modified to include base widening, the experimental results again correlate well with the theory. Finally, when emitter geometries are varied, the slope is shown to approach the theoretical value of (−1) as the emitter width approaches the non-crowded case.

The high-level-gain equation developed for devices with base widening is also simplified, but also seems to fit the experimental data quite well. A key experiment in support of the base-widening theory is the comparison of similar n+-p-n−-n+ and n+-p-p−-n+ transistors. Fig. 6 shows that the peak current gains for the two devices are different. This difference is expected, since β^* is the controlling factor at lower currents. The current gain of the n+-p-n−-n+ device falls off as the collector current increases due to base widening and the resulting additional recombination loss (controlled by the lifetime and width of the extended base region). At a certain collector current the base approaches the n+ collector region and the transport factor ceases to change appreciably. Above this current, injection efficiency becomes the controlling factor in the current gain. Thus, at these current levels the performance of the two structures should be identical as the data show. It can also be stated (although no experimental data is presented) that f_T contour curves correlate well with the calculated widened base widths.[18]

The derivation of an effective emitter width is, like the other equations, simplified and perhaps the least accurate. The ring-emitter experiments indicate that, for the structure studied, a 2-mil-wide emitter is the most efficient and reasonably free of crowding. This structure has a gain fall-off slope, when driven from the outside base, less than that of the wider emitters (ignoring the anomalous 20-mil-wide emitter ring temporarily), and the slope approaches the ideal (−1). At a gain of approximately 50, the slope is (−1). Insertion of this gain value and the measured base width of 0.7 mil in the developed equation yields an effective half-emitter width of 2.5 mils, which is in reasonable agreement with the theory. Similar checks on the other geometries could not be made because of thermal problems or because the (−1) slope appears too close to the peak current gain and the equations are not applicable.

The 20-mil-wide emitter is quite different from the others. Its behavior is explained as follows: The 20-mil emitter is so wide that the injection is crowded at the edge even at low average current densities. As a result, the edge portion of the emitter reaches gain fall-off current densities much earlier than the center region. The resultant gain fall-off curve is a composite of the constant-gain areas and areas in which the gain is decreasing. It can be easily demonstrated that such behavior yields the type of gain fall-off shape observed. The theoretical equation for the effective emitter half-width at low injection levels supports this explanation because it yields a half-width of 4 mils at a current density of 10 amperes per square centimeter.

Summary

Theoretical equations have been developed to describe the low-voltage, high-current behavior of power transistors. It is shown that these devices ideally should display a constant current-gain-times-collector-current product at high injection levels. If the performance differs from this ideal, then base-widening and/or emitter-current-crowding effects are present. The approximate equations developed allow the calculation of these effects as they modify the current-gain-times-current product. The validity of the approach is established by direct measurements on a variety of transistor geometries and structures.

Acknowledgments

The authors thank A. Blicher, C. F. Wheatley, J. Scott, M. Polinsky, and J. Ollendorf for their many stimulating discussions on portions of this work and C. Sickles and B. Upton for fabricating the test vehicles.

Appendix A—The Space-Charge Region

The space-charge region is a region very similar to the sheath that develops in a gas tube at a plasma-to-electrode interface. The solid-state problem is complicated by the fixed charges in the lattice. Poisson's equation for this region is

$$\frac{dE}{dx} = \frac{q}{\epsilon_r \epsilon_o} [N_D - n(x)]. \quad [45]$$

If it is assumed that the carriers move entirely by drift and the fixed donor charge is neglected, an approximate result valid throughout most of the space-charge region is easily obtained. Actually, because the neglected diffusion phenomena and the positive charge at the donor sites both act to aid in the conduction process through the space-charge region, the simplified computation is pessimistic. Eq. [45] then becomes

$$\frac{dE}{dx} = -\frac{q}{\epsilon_r \epsilon_o} n(x) = \frac{J_C}{\epsilon_r \epsilon_o \mu_n E(x)} \quad [46]$$

where the field varies from the value at the edge of the extended base to that which exists in the ohmic region (Eq. [18]). Usually the field in the base region is sufficiently low so that no great error is introduced by the assumption that it is zero. With this assumption, the width of the space-charge region is given by

$$W_{sc} = \frac{\epsilon_r \epsilon_o J_C}{2q^2 \mu_n N_D{}^2}. \quad [47]$$

The voltage drop across the space-charge region is given by

$$V_{sc} = \left(\frac{8}{9} \frac{J_C}{\epsilon_r \epsilon_o \mu_n} \right)^{1/2} (W_{sc})^{3/2} \quad [48]$$

Eq. [48] is the well-known expression for space-charge current flow.

By use of the space-charge and ohmic-region relationships, the following equation can be developed for the total width of both regions:

$$W_o + W_{sc} = (V_{CB}/J_C \rho_{n-}) + (1/6)\, J_C \rho_{n-}{}^2 \epsilon_r \epsilon_o \mu_n. \quad [49]$$

This width, when subtracted from the width of the $n-$ region, yields the amount of base widening (Eq. [16]). This equation is valid only for the following condition:

$$W_{n-} > W_{sc} + W_o. \quad [50]$$

Appendix B

If all of injection is assumed to take place within X_E, then the collector current density can be expressed

$$J_C = I_C / X_E P_E, \quad [51]$$

where P_E is the emitter perphery. Substitution of Eq. [51] in Eq. [21] yields

$$W_B{}^2 h_{FE} \left(\frac{I_C}{X_E P_E} \right) = K_E. \quad [52]$$

Combination with Eq. [44] then gives

$$W_B{}^2 h_{FE} \frac{I_C}{0.54 W_B (h_{FE})^{1/2} P_E} = K_E, \quad [53]$$

or

$$h_{FE} I_C{}^2 = \text{constant}. \quad [54]$$

Equation [54] indicates that the current-gain fall-off under current-crowded conditions assumes a -2 slope on a log h_{FE}-log I_C plot. It should be recognized that Eq. [54] is very approximate and is included only to show the effect of severe current crowding on the collector-current–current-gain product. In practice, transistors free of base widening and subject to emitter current crowding show gain fall-off slopes that approach this condition only at extreme currents.

References:

[1] W. M. Webster, "On The Variation of Junction-Transistor Current-Amplification Factor with Emitter Current," **Proc. IRE,** Vol. 42, p. 914, 1954.

[2] N. H. Fletcher, "The High Current Limit for Semiconductor Junction Devices," **Proc. IRE,** Vol. 45, p. 862, 1957.

[3] N. H. Fletcher, "Some Aspects of the Design of Power Transistors," **Proc. IRE,** Vol. 43, p. 551, 1955.

[4] R. Emeis, A. Herlet, and E. Spenke, "The Effective Emitter Area of Power Transistors," **Proc. IRE, Vol. 46,** p. 1220, 1958.

[5] J. R. Hauser, "The Effect of Distributed Base Potential on Emitter-Current Injection Density and Effective Base Resistance of Stripe Transistor Geometrics," **IEEE Trans. Electron Devices**, p. 238, 1964.

[6] R. D. Thornton, D. DeWitt, P. Gray, and E. R. Chenette, "Characteristics and Limitations of Transistors," **SEEC**, Vol. 4, Chapter 1, John Wiley and Sons, 1966.

[7] J. M. Early, "Maximum Rapidly-Switchable Power Density in Junction Triodes," **IRE Trans. Electron Devices**, Vol. ED-6, p. 322, July 1959.

[8] C. T. Kirk, Jr., "A Theory of Transistor Cut-off Frequency ($f_{(t)}$) Fall-off at High Current Densities," **IRE Trans. Electron Devices**, Vol. 9, p. 164, 1962.

[9] R. D. Middlebrook, "Effects of Modified Collector Boundary Conditions On The Basic Properties of a Transistor," **Solid State Electronics**, Vol. 6, p. 573, 1963.

[10] R. D. Middlebrook, "Conditions at a P-N Junction in the Presence of Collected Current", **Solid State Electronics**, Vol. 6, p. 555, 1963.

[11] L. A. Hahn, "The Saturation Characteristics of High Voltage Transistors," **Proc. IEEE**, Vol. 55, No. 8, p. 1384, Aug. 1967.

[12] D. P. Kennedy and R. R. O'Brien, "On The Mathematical Theory of the Linear-Graded P-N Junction," **IBM Journal**, p. 252, 1967.

[13] H. Gummel, H. C. Poon, and D. L. Sharfetter, "High Injection in Epitaxial Transistors," (to be published).

[14] R. Shilling, "Computer Aided Device Analysis and Design," Report EP-2, Seminar Proceedings, Stevens Institute of Technology, Ed. by G. J. Herskowitz, May 26, 1969.

[15] A. Herlet and K. Raithel, "Forward Characteristics of Thyristors in the Fired State," **Solid State Electronics**, Vol. 9, p. 1089, 1966.

[16] A. vanderZiel and D. Agouridis, "The Cutoff Frequency Falloff in UHF Transistors at High Currents," **Proc. IEEE**, Vol. 54, p. 411, March 1966.

[17] R. J. Wittier and D. A. Tremere, "Current Gain and Cutoff Frequency Falloff at High Currents," **IEEE Trans. Electron Devices**, Vol. ED-16, No. 1, p. 39, Jan. 1969.

[18] C. F. Wheatley, "Observation of the influence of Base Widening Upon Beta and f_T," **RCA Review**, Vol. 32, p. 247, June 1971.

Observation of the Influence of Base Widening Upon Beta and f_T

C. F. Wheatley, RCA Solid State Division, Somerville, N. J.

Abstract—The quasi-saturation region of a bipolar transistor operating at low voltages and high current densities has been analyzed by use of a base-widening model. If the model is correct, it appears that both current gain (beta) and gain-bandwidth product (f_T) begin to decrease with the onset of base widening. Because this behavior is difficult to verify for most power devices as a result of the distributed nature of large transistors, small transistors were used for experimental verification of these influences.

The transistors evaluated were fabricated by an integrated-circuit process and had the structure shown in Fig. 1. Two emitter lengths were used, 1.5 and 3.5 mils. The collector bulk resistance of Fig. 1 is of a most complex form in the exact case, but it may be approximated as consisting of three terms: R_1, R_2, and R_3. R_1 is the resistance from the external collector contact to the buried n+ layer. It is determined primarily by physical dimensions and the epitaxial n-type layer, and

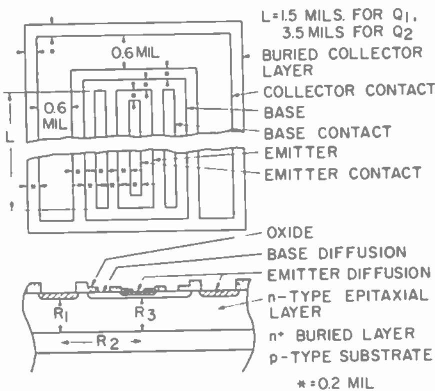

Fig. 1—Structure of transistors that were fabricated by an integrated-circuit process.

generally cannot be conductivity-modulated. R_2 is the resistance through the buried n+ layer and, like R_1, cannot be significantly conductivity-modulated. The third term, R_3, is the term that may be substantially modified by base-widening effects. It is formed from the epitaxial layer between the collector-depletion layer and the buried n+ layer. The emitter bulk resistance may be considered insignificant for this study.

If it is assumed that there is some spreading of current and approximately a 1-μm diffusion of the n+ collector contact diffusion, the value of R_1 is of the order of 15 ohms for the smaller transistor Q_1 and 10 ohms for Q_2. The lateral resistance through the buried n-type layer is about 3 ohms for Q_1 and 1.5 ohms for Q_2.

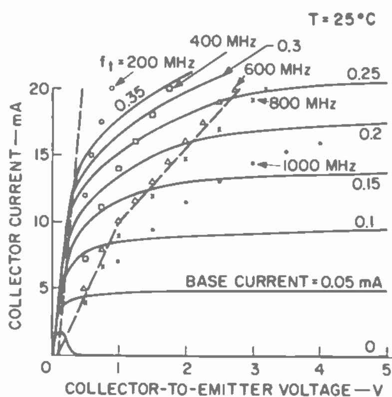

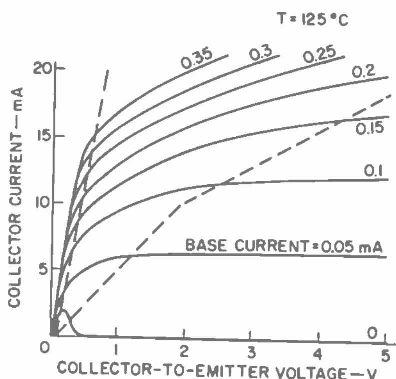

Fig. 2—(a) Collector characteristics of Q_1 at 25°C for constant steps of base current; (b) similar information for Q_1 at 125°C with the f_T data omitted.

The third component of collector bulk resistance is somewhat more difficult to evaluate. If the current level is sufficiently low, emitter injection is fairly uniform and the calculation is fairly simple and similar to that for the first component. The resulting values are 90 ohms for Q_1 and 40 ohms for Q_2. However, at current levels of the order of 10 and 20 milliamperes, respectively, edge crowding compounds the analysis. If radial current flow is assumed, and line injection from the emitter edges is further assumed as the worst case, it is reasonable to assume that collector current flow initiates from a semicylindrical boundary with a radius equal to the base width. This simplified model

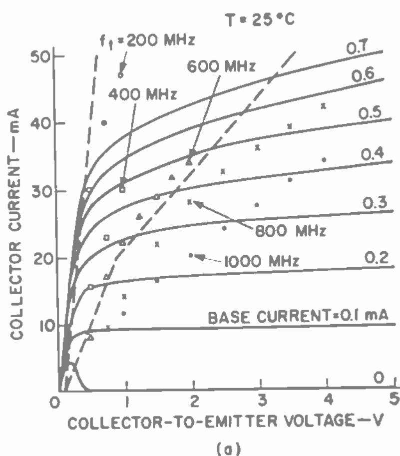

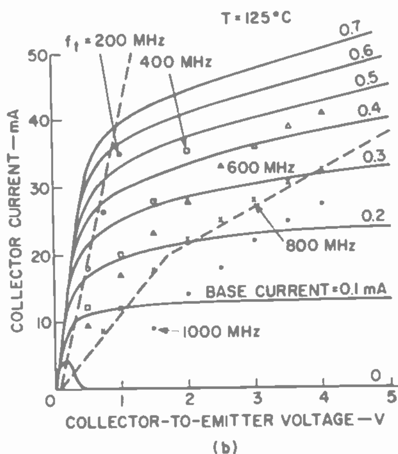

Fig. 3—Characteristic curves for the larger transistor Q_2: (a) at 25°C: (b) at 125°C.

results in maximum values of the third component of collector bulk resistance of 180 and 90 ohms, respectively, for Q_1 and Q_2.

If the temperature is increased from 25°C to 125°C, the resistances associated with the buried layer increase about 50%, while those associated with the epitaxial layer are approximately doubled. Edge crowding is not substantially altered by the elevated temperature.

Fig. 2(a) shows the collector characteristics of Q_1 at 25°C for constant steps of base current, with data points defining the f_T contour curves for Q_1 superimposed on the photo. The straight line with the steeper slope represents the ohmic effects of the first two components of collector saturation resistance. This line should correspond to the R_{SAT} of the heavily overdriven transistor. The double-sloped line represents the ohmic effects of all three components of collector saturation resistance, as calculated previously. Current gain and f_T characteristics below and to the right of this curve should be slightly dependent upon voltage and current, while the characteristics above and to the left of this curve should be quite variant with voltage and current.

Fig. 2(b) shows similar information for Q_1 at 125°C with the f_T data omitted. Figs. 3(a) and 3(b) show curves for the larger transistor Q_2 at 25°C and 125°C.

It can be seen that the initiation of f_T degradation associated with operation in the quasi-saturation region can be well understood and predicted from ohmic calculations or curve-tracer observations. Although distributed effects in power transistors are more difficult to predict, similar methods can provide some insight to these effects.

References:

[1] Whittier, R. J., and Tremere, D.A., "Current Gain and Cutoff Frequency Falloff at High Currents," **IEEE Trans., Electron Devices,** Vol. ED-16, p. 39, 1969.

[2] H. C. Poon, H. K. Gummel, and D. L. Scharfetter, "High Injection in Epitaxial Transistors," **IEEE Trans. Electron Devices,** Vol. ED-16, p. 455, 1969.

[3] L. A. Hahn, "The Effect of Collector Resistance Upon the High Current Capability of n-p-n Transistors," **IEEE Trans. Electron Devices,** Vol. ED-16, p. 654, 1969.

[4] R. B. Schilling, "A Regional Approach for Computer-Aided Transistor Design," **IEEE Trans. Electron Devices,** Vol. ED-12, p. 152, 1969.

[5] J. Olmstead, W. Einthoven, S. Ponczak, and P. J. Kannam, "High-Level Current Gain in Bipolar Power Transistors," **RCA Review,** Vol. 32, p. 221, June 1971.

Systems and Technologies for Solid-State Image Sensors*

Paul K. Weimer, RCA Laboratories, Princeton, N. J.

Abstract—An extended research program on self-scanned solid-state image sensors at RCA Laboratories has included scanning by charge transfer and by x-y addressing. Experimental arrays have been fabricated by thin-film techniques and by silicon technology. This paper compares and evaluates these contrasting approaches to the design and fabrication of two-dimensional sensors.

Introduction

Until very recently nearly all systems for solid-state scanning of image-sensor arrays have involved some form of *x-y* addressing. Integrated scan generators, such as parallel-output shift registers or decoders, have been located on the periphery of the sensor array, either on separate substrates or on the same substrate with the sensor. Within the past year the concept of charge transfer, as exemplified by the "bucket brigade" circuit of Sangster and Teer[1] or the "charge-coupling" principle of Boyle and Smith,[2] has made possible an entirely new approach to solid-state scanning. Instead of sampling the picture signal at each element by the coincidence of pulses from the two scan generators, the elemental charge pattern produced by the image can be transferred substantially intact to the edge of the array where it is converted into a video signal.

Because of its novelty, the charge-transfer approach, and in particular the charge-coupling version, has received much attention. Our investigation of bucket-brigade sensors has demonstrated that two-dimensional imaging by charge transfer is indeed possible, and may offer some advantages. However, the use of charge transfer introduces limitations as well, and its relative merits in comparison with the more advanced forms of *x-y* addressing must be carefully evaluated.

---

* This paper is based upon an invited talk which was presented at the 1971 IEEE International Convention, New York, N. Y., March 24, 1971.

Charge-Transfer Scanning

Fig. 1 shows a photomicrograph of a portion of a bucket-brigade sensor.[3] An array of 15 × 32 diffused silicon photodiodes covered with an insulated electrode pattern is scanned line by line by the transfer of the accumulated charge pattern along each horizontal row to the edge of the array. The clock voltage, which causes the pattern to be transferred out when a given line is scanned, is disconnected from all

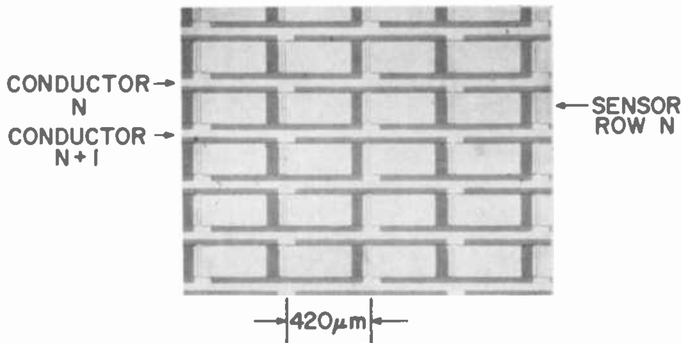

Fig. 1—Photomicrograph of a portion of a 15 × 16 element photodiode array employing internal bucket-brigade scanning. Each element comprises 2 photodiodes, 2 MOS transistors, and 2 capacitors.

lines except the one being scanned. The light from the scene is continuously absorbed in the depletion region surrounding each photodiode, causing the charge pattern to accumulate on the diffused islands under the gate electrodes. Although continuous illumination may introduce some smearing of the pattern during the transfer process, this effect would normally be negligible if the time to scan a single line is a small fraction of the total frame time. The ratio of line time to frame time is 1:500 for standard television scan rates.

Fig. 2 shows the equivalent circuit of the sensor of Fig. 1, with the addition of a bucket-brigade vertical register that gates the horizontal clock drive to each row in sequence. This circuit is simple to fabricate, since a single diffusion step forms the conducting regions that simultaneously serve as photodiodes, as sources and drains for the transistors, and as one plate of the elemental capacitors. Oxidation of the silicon and a final layer of metallization complete the structure.

The line-by-line method of scanning by charge transfer can be used equally well with a charge-coupled sensor. Charge-coupled sensors differ from bucket-brigade sensors in that the diffused elemental islands

are omitted in the charge-coupled array. Minority carriers released by the light are collected at the surface of the semiconductor and transferred along the surface by the application of clock voltages to the electrode structure. The line-by-line transfer method can be used with either sequential or interlaced scanning, and does not require additional space for storage external to the photosensitive area as required for some systems in which all columns are transferred out in parallel.[4]

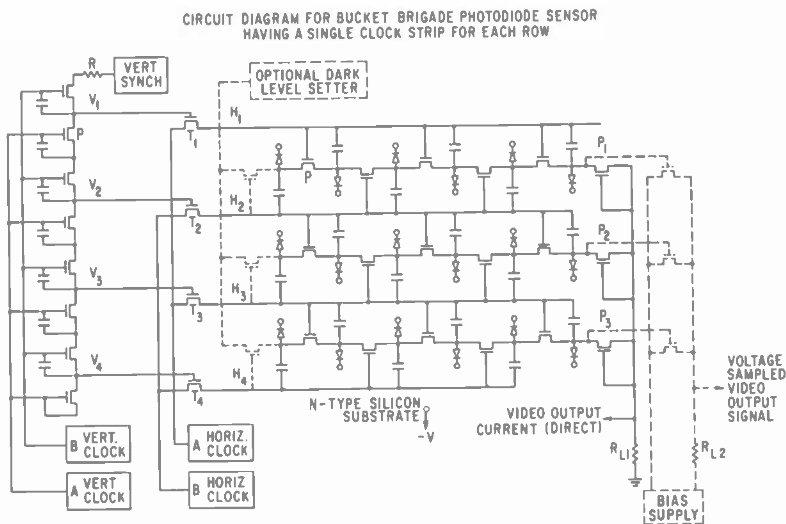

Fig. 2—Equivalent circuit of the bucket-brigade charge-transfer sensor illustrated in Fig. 1. A bucket-brigade scan generator gates on the horizontal clock to successive pairs of conductors.

An operational advantage of charge-transfer sensors over conventional *x-y* addressed sensors is expected to lie in improved sensitivity and uniformity. If the charges can be transferred with negligible loss from the array to a common external electrode, the signals from all elements will be treated alike and can be measured with minimum interference from spurious background signals. On the other hand, when the light pattern is measured directly at each element by means of conventional *x-y* address strips, switching transients from the horizontal scan generator may introduce a spurious background level that limits both sensitivity and uniformity.

The circuit of Fig. 2 illustrates two methods of extracting the signal from a charge-transfer sensor. The total charge arriving at a common electrode can provide the video output current directly. Alternatively, a high input impedance amplifier, such as an MOS tran-

sistor, near the end of each line can be used to convert the voltage fluctuations into a video signal.

The 15 × 16 element bucket-brigade sensor was operated successfully at 300 kHz clock frequency in both the current- and voltage-sampling modes. A 32 × 44 element bucket-brigade sensor incorporating a 32-stage bucket-brigade shift register for vertical scanning is now under construction.

The successful fabrication of high-resolution, two-dimensional arrays having 500 × 500 elements that are scanned by charge transfer will require transfer efficiencies exceeding 99.9% per stage. If the array is to be scanned at television rates, the horizontal clock frequency will approach 10 MHz. Transfer efficiencies of more than 99.9% at one MHz have been reported for both bucket-brigade[5] and charge-coupled[4] devices. There is a reasonable expectation that the necessary improvement in efficiency at higher frequencies will ultimately be obtained with either type of transfer. The charge-coupled devices might be expected to operate at higher frequencies than the MOS bucket-brigades, since transit times can be reduced more effectively by the use of fringing fields under the electrodes.[6] However, the effect of surface states[7] upon the high-frequency performance of charge-coupled devices has not yet been determined.

It is at present premature to compare the ease of fabrication of bucket-brigade and charge-coupled sensors with each other or with x-y addressed sensors. Each will require the development of a more advanced integrated-circuit technology to build sensors that approach the performance of camera tubes. Both bucket-brigade and charge-coupled sensor arrays of modest size can be produced in silicon with one diffusion and a single layer of metallization. The charge-coupled arrays can probably be made with smaller element sizes, yielding higher resolution for the sensor.

An advantage of the bucket-brigade circuit is its versatility in applications requiring multiple inputs or outputs. An example of this is the bucket-brigade scan generator[3] shown in Fig. 2. Such registers can be built with one MOS transistor and one capacitor per stage, whereas a normal MOS register requires 6 transistors and two capacitors. Bucket-brigade registers can also be used in conjunction with other types of sensor elements such as photoconductors and phototransistors, as well as photodiodes. Fig. 3 illustrates the use of two bucket-brigade scan generators for scanning a capacitor-driven phototransistor[8] array. Since no charge can be removed from the midpoints of a bucket-brigade register, it cannot drive electrodes that draw

current, but it is satisfactory for gating a row of MOS transistors such as are normally used in coupling to an array. With this sensor the video output can be derived from either the common collector substrate or from the transistor bus. The entire structure is a relatively simple one that can be fabricated with two diffusion steps and one layer of metallization. It may be noted that the transfer-efficiency requirements are easier to meet in a scan generator where a single high-level digital

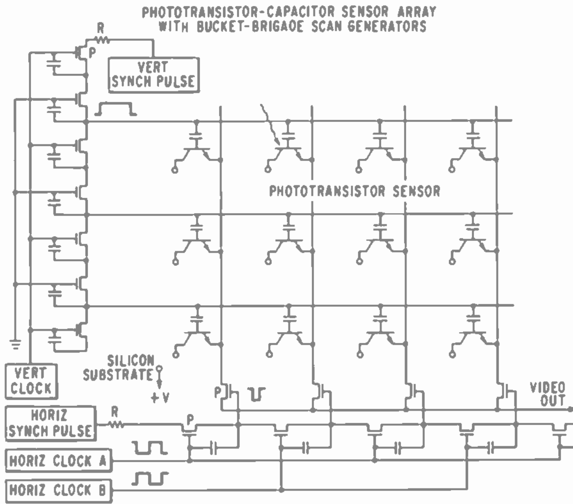

Fig. 3—A novel phototransistor array having a common collector output and scanned by means of two bucket-brigade scan generators.

pulse is being transferred than where analog signals are being transferred. Also, because the scan pulse advances one element on each half cycle of the clock, the clock frequency required for horizontal scanning is reduced by a factor of two and the total number of transfers is reduced by half. Thus for a 500 × 500 element x-y addressed sensor the horizontal clock frequency would be 5 MHz and the vertical clock 7.5-15 kHz. Very low leakage will be required for a bucket-brigade register to run as slowly as required for vertical scanning, since the capacitors must hold charge for the total scan period of 1/60 second. The leakage requirement is over 100 times more severe than for the conventional dynamic MOS register, but is no more severe than required for 1/60 second storage in the array itself.

Thin-Film Sensor Arrays

In spite of the advanced state of silicon integrated-circuit technology the fabrication of self-scanned sensors having unusually large areas or many picture elements is difficult and costly. An entirely different technology based upon thin-film deposition techniques is being explored. For a number of years RCA, with support of the Avionics Laboratory at Wright Field, has carried on a research program on thin-film image sensors. In spite of the purely experimental status of thin-film transistors, this work has been on the forefront of the image-sensor field from the standpoint of the total number of elements, spacing between elements, degree of integration of the scanning circuits, and elemental scan rates. Although single-line sensors were built for evaluation of scan generators, the investigation of two-dimensional arrays has remained the major research objective.

In 1966 we built a solid-state camera containing a 180 × 180 element photoconductor–diode sensor that was scanned by two 180-stage parallel-output thin-film shift registers[9] For many years, this array represented the largest number of elements to be scanned by integrated parallel-output shift registers. Fig. 4 is a photograph of the battery-operated camera and transmitter based upon the 180 × 180 element sensor.

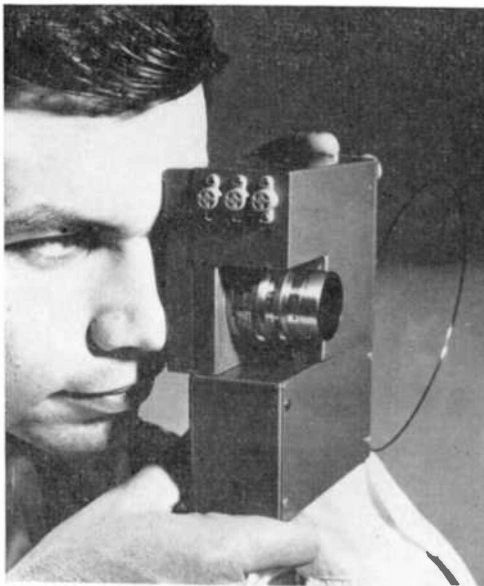

Fig. 4—A photograph of a battery operated solid-state sensor camera incorporating the 180 × 180 element array. The video signal is radiated directly from the camera to a nearby receiver via UHF.

In 1968, an improved 256 × 256 element camera[10] was built whose photoconductive sensor was scanned in 1/60 sec by two 256-stage thin-film decoders. Fig. 5 shows a circuit diagram of the thin-film sensor and the integrated decoders that provided vertical and horizontal scanning. Each decoder was driven by two 16-stage shift registers located external to the thin-film integrated circuit. The sensor and

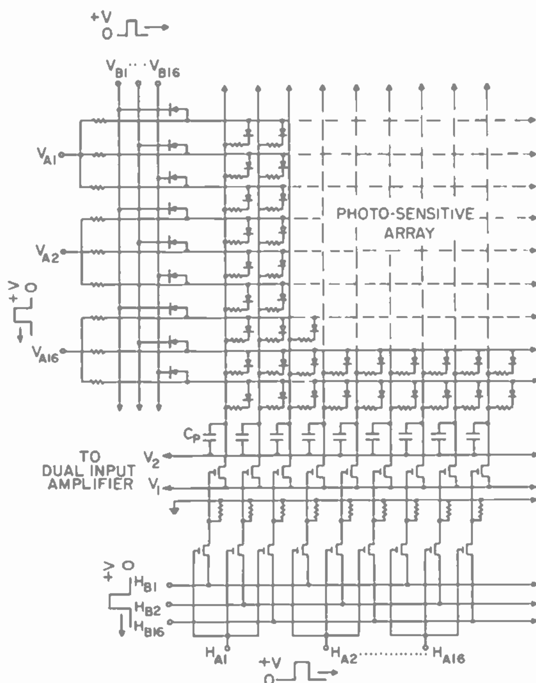

Fig. 5—Equivalent circuit for the 256 × 256 element integrated sensor, including a transistor decoder for horizontal scanning, a diode decoder for vertical scanning, and video coupling circuit for signal enhancement by line storage.

vertical decoder were deposited on one glass substrate, and the horizontal decoder and video multiplexer were deposited on a second substrate. These substrates were mounted on a printed-circuit card, as shown in Fig. 6, for convenient plugging into the camera.

The 256-output decoders were used instead of 256-stage parallel-output shift registers because they were somewhat easier to construct than shift registers and could be made to operate at the 4.8 MHz clock rate required for scanning the array in 1/60 second. However, decoders require more complex drive circuits than registers and may introduce periodic defects into the transmitted picture.

A more significant innovation in the 256 × 256 element sensor was the use of line storage to increase the output signal level by approximately 256 times. Simultaneous photocurrents from all the elements along a given row were passed down the column address strips to the thin-film multiplexer. Charge was accumulated on the column capacitors for a line-time and then discharged sequentially into the video output bus. The increase in output signal obtained by line storage combined with the high quantum gain of the photoconductor led to a significant improvement in operating sensitivity although it was still somewhat less than that of the antimony sulfide vidicon.

Work is now in progress on a solid-state camera employing a 512 × 512 element sensor[11] in which the sensor is to be scanned at 30

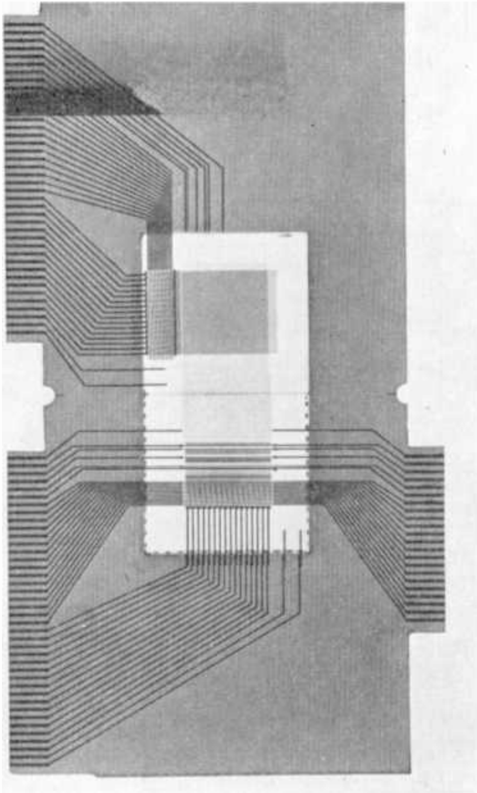

Fig. 6—The complete 256 × 256 element integrated thin-film image sensor deposited upon two glass substrates mounted on a printed-circuit board.

frames per second. This scanning rate requires a horizontal clock frequency of 9.6 MHz, or 100 nanoseconds for discharging each element. Since the capacitance of each address strip increases with array size, the ability of a decoder or shift register to discharge each strip in an element time is further reduced. One way of solving this problem is by the use of the integrated parallel output decoder shown in Fig. 7. The total video signal is brought out through 16 parallel

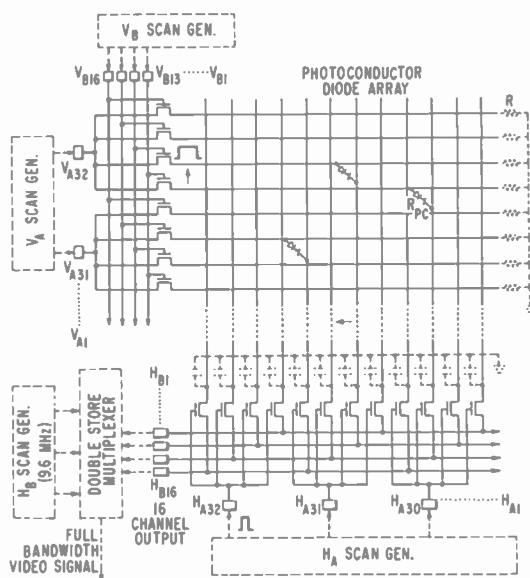

Fig. 7—System design of the parallel-output decoder and external double store multiplexer to be used for extracting the video signal from the 512 × 512 element sensor.

channels whose individual frequency response need be no greater than 300 kHz, or 1/16 of the total 4.8 MHz bandwidth. An external double store multiplexer (shown dotted) serially reassembles the information into a normal single-channel video signal of the original bandwidth. This system has been tested with a 256 × 256 element sensor and found to offer improved sensitivity over the earlier single-channel sensors. Fig. 8 shows a photomicrograph of the 512 × 512 element thin-film sensor with integrated scanning decoders on the same substrate with the sensor. The entire pattern was deposited in one pump-down of the vacuum system. Sensors having over 260,000 cross-overs have been produced entirely free of shorts. The glass substrate is

attached to a printed circuit card for convenient plugging into the camera. Each decoder consists of 32 groups of 16 each so that a total of 96 connections have to be made to the sensor.

The thin-film techniques have proved to be very convenient for experimental samples because test circuits can be varied without requiring new masks. Freedom from defects in samples produced in a single vacuum have been very encouraging. Our present wire-grill masking facilities would allow fabrication of integrated sensors having up to 1000 × 1000 elements on one-mil centers. Thin-film techniques have also been used in the fabrication of sensors that cover too large an area for conventional silicon technology. Fig. 9 shows a photograph of a sensor array containing 960 photoconductor–diode elements deposited on a glass plate 4 × 8 inches on a side.[12] This sensor was built for use in a static card reader for standard-size computer punched cards.

Thin-Film versus Silicon Technology

A comparison of the relative merits of thin-film versus silicon technology may be summarized as follows. For applications where the number of elements, physical dimensions, and spectral response can be obtained economically with standard silicon technology, this approach would be the logical one. The ability to fabricate silicon photodiodes with charge storage, phototransistors with gain, and bipolar and MOS integrated circuits that are stable and fast offers a tremendous capability that has not yet been fully exploited in image sensors. The thin-film approach has been found advantageous for sensors in which the requirements on total number of elements is very large or the physical size of the array must exceed the capability of the existing silicon techniques. The ability to fabricate complex circuits in one pump-down of a vacuum system offers significant advantages in the elimination of defects, one of the major problems in image sensor fabrication.

Acknowledgments

The development of the 512 × 512 element sensor was sponsored by the Air Force Avionics Laboratory, Air Force Systems Command, Wright Patterson Air Force Base, Ohio, D. J. Peacock, supervisor, under contract no. F33-615-70-C-1215, and by RCA Laboratories. The author wishes to thank F. G. Durfee, M. G. Kovac, L. Meray-Horvath, W. S. Pike, and F. V. Shallcross for helpful discussions.

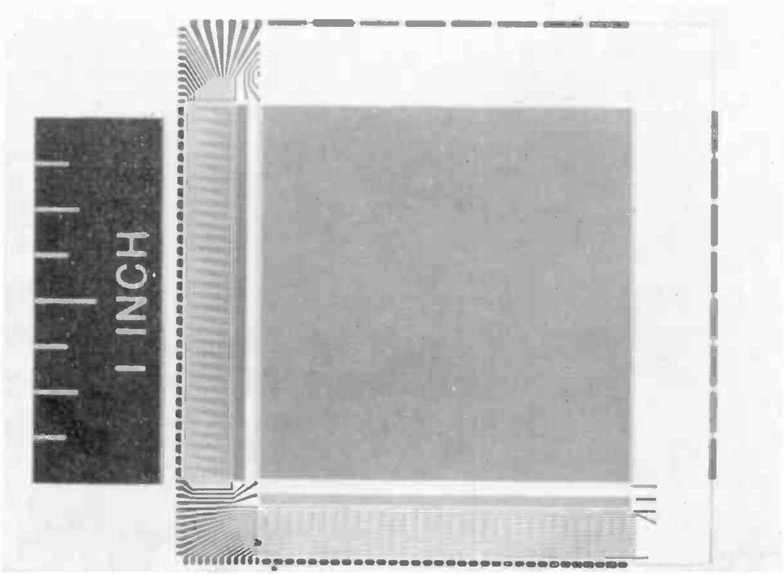

Fig. 8—Photograph of a 512 × 512 element photoconductor–diode thin-film sensor having integrated scanning decoders on the same substrate.

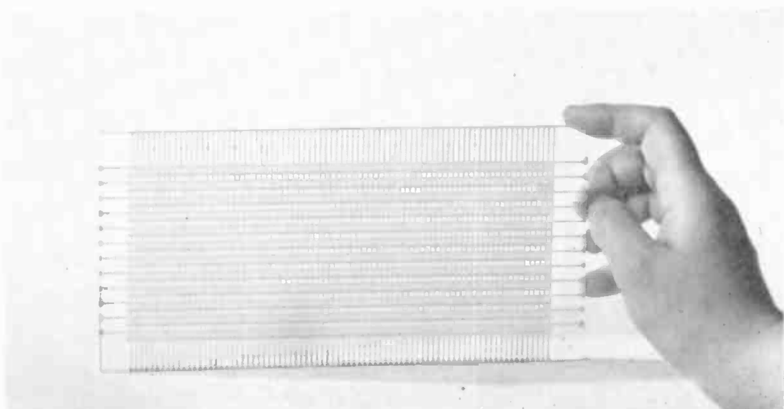

Fig. 9—Photograph of an 80 × 12 element photoconductor–diode sensor suitable for static reading of large-size computer punched cards. The sensor elements were deposited onto a 4 × 8 inch glass substrate by evaporation.

References:

[1] F. L. J. Sangster and K. Teer, "Bucket-Brigade Electronics—New Possibilities for Delay, Time Axes Conversion, and Scanning," **IEEE J. Solid State Circuits,** Vol. SC-4, No. 3, p. 131, June 1969.

[2] W. S. Boyle and G. E. Smith, "Charge Coupled Semiconductor Devices," **Bell System Tech. J.,** p. 587, April, 1970.

[3] M. G. Kovac, P. K. Weimer, F. V. Shallcross, and W. S. Pike, "Self-Scanned Image Sensors Based Upon Bucket-Brigade Scanning," Abstract of paper presented at IEEE Electron Devices Meeting, Wash., D. C., Oct. 29, 1970.

[4] W. J. Bertram, "Application of the Charge-Coupled Device Concept to Solid State Image Sensors," paper presented at 1971 IEEE International Convention, New York, N. Y., March 1971.

[5] C. N. Berglund and H. J. Boll, "Performance Limits of Bucket-Brigade Shift Registers," Paper presented at IEEE Electron Devices Meeting, Wash., D. C., Oct. 29, 1970.

[6] W. F. Kosonocky and J. G. Carnes, "Charge-Coupled Digital Circuits," Paper presented at 1971 International Solid State Circuits Conf., Philadelphia, Pa., Feb. 19, 1971.

[7] R. S. Strain, "Power and Surface State Loss Analysis of Charge-Coupled Devices," International Electron Devices Meeting, Washington, D. C., Oct. 1970.

[8] P. K. Weimer, F. V. Shallcross, and V. L. Frantz, "Phototransistor Arrays of Simplified Design," **IEEE J. Solid State Circuits,** Vol. SC6, p. 120,June 1971.

[9] P. K. Weimer, G. Sadasiv, J. E. Meyer, Jr., L. Meray-Horvath, and W. S. Pike, "A Self-Scanned Solid-State Image Sensor," **Proc. IEEE,** Vol. 55, p. 1591, Sept. 1967.

[10] P. K. Weimer, W. S. Pike, G. Sadasiv, F. V. Shallcross, and L. Meray-Horvath, "Multielement Self-Scanned Mosaic Sensors," **IEEE Spectrum,** Vol. 6, No. 3, p. 52, March 1969.

[11] P. K. Weimer, F. G. Durfee, L. Meray-Horvath, W. S. Pike, and F. V. Shallcross, "Solid State Digital Scanning of Mosaic Sensors (Phase V)," **Technical Report AFAL-TR-71-76,** March 1971.

[12] F. V. Shallcross, W. S. Pike, P. K. Weimer, and G. M. Fryszman, "A Photoconductive Sensor for Card Readers," **IEEE Trans. Electron Devices,** Vol. ED 17, No. 12, p. 1086, Dec. 1970.

Optical Techniques for Detecting Defects in Silicon-On-Insulator Devices

Richard A. Sunshine, RCA Laboratories, Princeton, N. J.

Abstract—Observation of light emitted by and transmitted through operating devices can quickly and easily provide information about the device structure that is not obtainable from electrical measurements alone. With this technique, it is possible to detect imperfections such as non-uniformities in the junction, diffusion spikes, sites of localized breakdown (especially at the edge of samples), inhomogeneities and defects in the film, peculiarities in the shape of the diffusion front, and regions of high thermal generation. The optical techniques should be very helpful in evaluating processing procedures for silicon-on-insulator devices, and in the development of protection diodes for SOS memory circuits.

1. Introduction

Devices made from silicon films heteroepitaxially grown on insulating substrates appear to be useful in high-speed switching circuits and in applications where radiation hardness is required. Consequently, the properties of these films, and of the junctions diffused into them, have been intensively investigated.[1] Most results reported to date have been derived from studies of the electrical properties of the films and devices as a function of film growth and processing parameters. These results are extremely encouraging. Substantial advances have been made in material quality,[2] and extremely high performance circuits have been demonstrated.[3] Nevertheless, continued work on the characterization of films and devices is needed both to perfect the processing techniques and to develop new materials, such as silicon-on-spinel, and new devices such as protection diodes for computer circuits. While the electrical evaluation techniques have proven quite useful, it is often difficult to relate electrical characteristics with specific problems in the device structure or processing procedure.

It has previously been observed that light can be emitted from plasmas in diodes in silicon on sapphire (SOS) without self-destruc-

iton,[4] and also that light can be absorbed in silicon-on-sapphire films when local heating occurs.[5] In this paper we discuss how these phenomena can quickly and easily be used to provide information that is not obtainable electrically about junction profiles, uniformity, and perfection. Each of the techniques discussed is illustrated with results from experiments using vertical junction silicon-on-sapphire diodes.

2. Experimental Considerations

The basic technique to be described involves observation of the light emitted by, or transmitted through, the electrically active region of the device while it is operating under various conditions of forward and reverse bias. To obtain useful spatial resolution, it is necessary to form the image of the operating device using a metallurgical microscope objective lens. These lenses usually have working distances of only a few mm. In the conventional arrangement, the microscope objective is positioned above the sample, and there is little or no room to make electrical contact to the devices using probes. This problem can be avoided by mounting the samples on headers and making contact to them using bonded wires. The light emitted from the sample can be photographed using this arrangement, providing the junction is not covered by metallization.

A more satisfactory experimental arrangement,[5] which is applicable to diode and transistor structures fabricated in semiconductor films grown on transparent substrates, is shown in Fig. 1. The sample rests on a transparent support above the microscope objective lens. Electrical contact for either dc or pulsed operation is made using mechanical probes positioned above the device. The image of the active region of the device is obtained by focusing the microscope objective through the transparent support and substrate. Consequently, the device must be fabricated on a substrate with a polished rather than lapped-bottom surface. For observation of emitted light using this arrangement, metallization covering the active region of the device does not cause any serious problem. For observation of thermally induced changes in the absorption of transmitted light, the illumination source is placed above the sample, and no metallization can be present over the region of the sample to be observed.

With the apparatus presently available, the image may be viewed directly or photographed using microscope eyepieces, or it may be focused on the target of a very sensitive Silicon Intensifier Target television camera[6] and viewed or photographed from the kinescope of the video monitor.

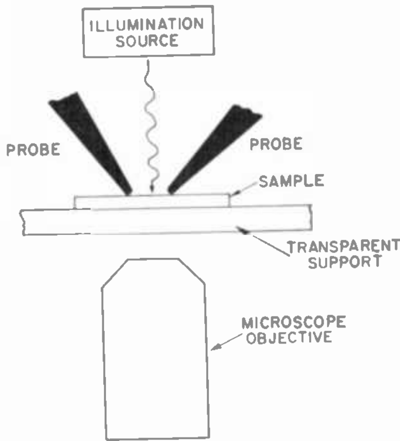

Fig. 1—Experimental arrangement for high-resolution optical observation of light absorption and emission by SOS sample operating under dc or pulse conditions.

The remainder of this paper discusses how observation of light emitted by the diode provides information. As an example, we use the results of a study of SOS vertical junction diodes fabricated in a manner similar to that discussed by Dumin and Silver.[7] A typical structure is illustrated in Fig. 2. The geometry was chosen so that the metallization does not cover the junction and the device may be viewed with transmitted light over its entire electrical length.

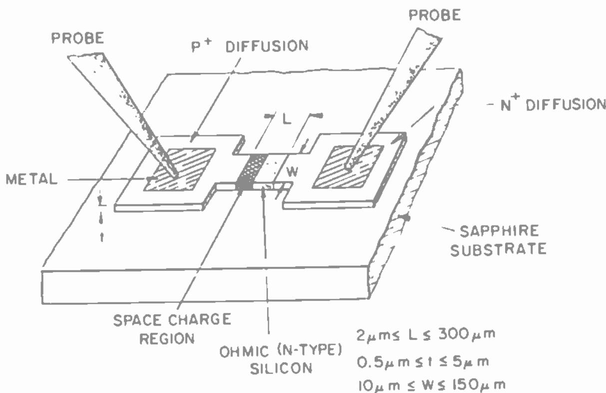

Fig. 2—Geometry of SOS vertical junction diode.

3. Light Emission Studies

Avalanche-Generated Light Emission

It has been known for many years that if an imperfect junction is reverse-biased into avalanche breakdown, the localized sites of high current generation, or microplasmas, often emit visible radiation of electronic origin.[8] Kressel[9] has reviewed this phenomenon and the role of imperfections on the electrical breakdown of p-n junctions. He has shown that microplasma sites result from the presence of lattice imperfections in the space-charge region. These imperfections include dislocations, nonuniformities in the impurity distribution, spikes in the diffusion fronts, precipitates, structural imperfections, and mechanical damage. He further points out that nonuniform breakdown can often be detected electrically by slope discontinuities in the *I-V* characteristics in the breakdown region, soft reverse bias *I-V* characteristics, or by large amplitude fluctuations of the current in the breakdown region. They usually can be detected optically by light emission in discrete spots while the junction is reverse biased into avalanche.

We have found that silicon-on-sapphire diodes do not give any electrical indication of nonuniform breakdown unless the junction is very poor. However, these diodes do emit visible light when and where avalanche current generation takes place. The intensity of the emitted light at any point in the junction is proportional to the avalanche-generated current density at that point. Consequently those inhomogeneities that result in localized high electric fields will avalanche and emit light at a lower diode voltage than will the surrounding regions. Thus, the uniformity of the avalanche emission is a measure of the uniformity of the junction.

Typical Light Emission from an SOS Diode

As an example, consider the SOS diode whose electrical characteristics are shown on different current and voltage scales in Fig. 3. These characteristics are stable and reproducible. The breakdown is sharp and free of discontinuities in slope and large amplitude fluctuations of current. Thus there is no electrical indication of nonuniform current generation at microplasma sites or surface effects. The light emission pattern for this diode at various biases is shown in Fig. 4. At currents up to 1 mA we see that the current is generated at only 4 or 5 microplasma sites, even though the multiplication is in excess of 10^4. As the current is increased the avalanche becomes more uniform due to space-

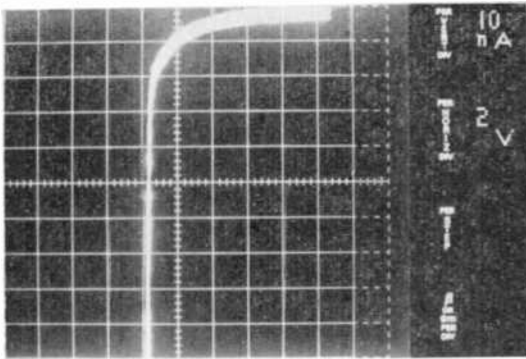

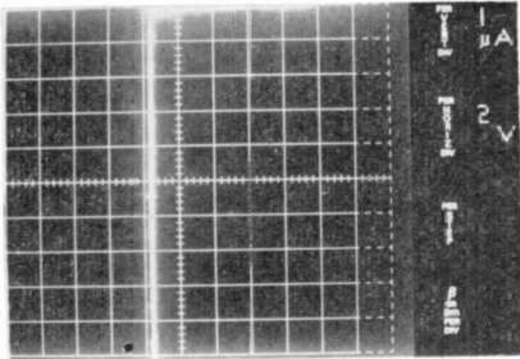

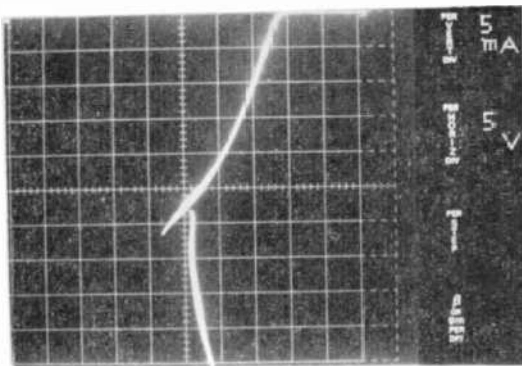

Fig. 3—Typical *I-V* characteristics of a reverse-biased SOS diode shown on different current and voltage scales.

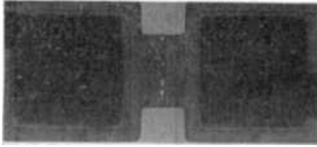

1 MA

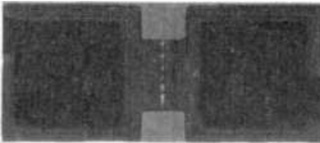

2.5 MA

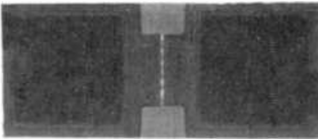

5 MA

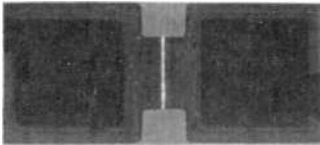

10 MA

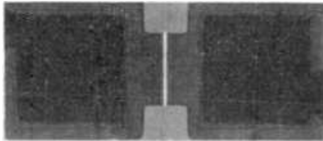

20 MA

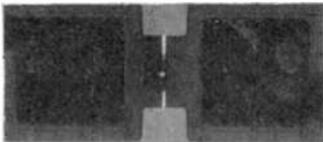

34 MA

Fig. 4—Light emission from dc-reverse-biased diode whose electrical characteristics are shown in Fig. 3.

charge-induced depletion-region widening and due to the decrease of the avalanche coefficients as the device heats.[5] At 20 mA, no nonuniformities in the avalanche emission can be detected. The 34 mA photograph was taken with the sample biased above the threshold for second breakdown, and will be discussed later. Thus we see that the avalanche emission pattern clearly shows the presence and location of nonuniformities in the junction that cannot be detected electrically. One measure of the uniformity of the junction is the current density at which the avalanche becomes uniform. Our better junctions have avalanched uniformly at a current density about two orders of magnitude lower than the diode shown in Fig. 4.

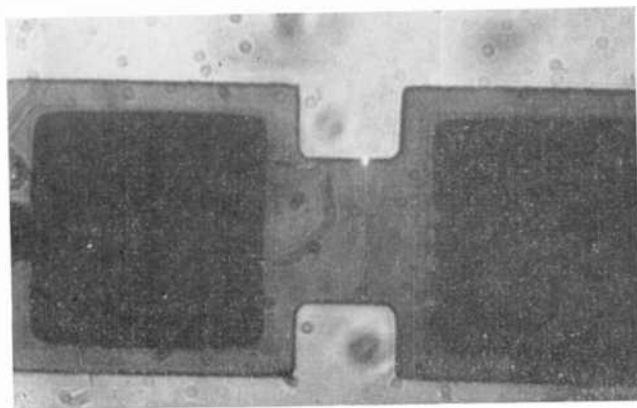

Fig. 5(a)—Avalanche emission from a diode in which avalanche breakdown is confined to the edge of the sample.

Breakdown at Edge of Sample

In Fig. 5a we show the avalanche emission pattern of a diode that avalanches strongly at the edges at several volts less bias than is required for avalanching in the rest of the junction. This localization of the avalanche at the edge of the sample cannot be detected electrically. The leakage currents are low, and the breakdown is stable, sharp, free of noise and "walkout" effects, and insensitive to moisture in the ambient. These electrical results strongly imply that the localization of the avalanche is not due to surface effects, such as inversion layer formation or ionic motion, at the edge of the sample. We observe this preferential breakdown at the edges in nearly all samples where

the silicon is etched prior to the diffusions, and rarely in samples where the silicon is etched after the diffusion. Consequently, we conclude that the avalanche probably occurs at the high-field region associated with diffusion spikes at the edges of the samples. This edge problem can have three effects on the device characteristics. First, the breakdown voltage of the junction is reduced. Second, if a diode with preferential breakdown at the edges is reverse-biased with a large current, the avalanching region becomes hot enough for the doping impurity to migrate along the edge of the sample and short the elec-

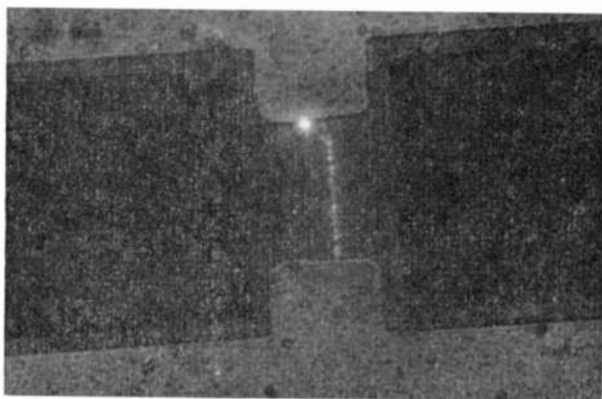

Fig. 5(b)—Avalanche emission from a diode which has failed due to migration of the dopant along the edge of the sample.

trically active region. Fig. 5b shows the avalanche emission pattern of a diode that had failed in this manner. While this failure mode does not cause problems with low-voltage, low-current MOS transistors for computer circuits, it is of critical importance to avoid this effect in the diodes used to protect these circuits from static-charge build up. Finally, these edge problems often increase the reverse leakage current of the diode.

Diffusion Profile

Observation of the avalanche emission pattern can provide qualitative information about the diffusion profile in these devices. An example is shown in Fig. 6. As has been shown by Burns and Scott[10] the diffusion constant for doping impurity atoms can be very much higher near the silicon–sapphire interface than it is in the remainder of the film. Con-

sequently, when the diffusion front reaches this disordered region of high defect density, the dopant atoms can rapidly diffuse in the lateral direction. The resulting diffusion profile is shown schematically in Fig. 6. Avalanching takes place at the top and bottom of the film, where the fields are highest. The avalanche emission pattern in this

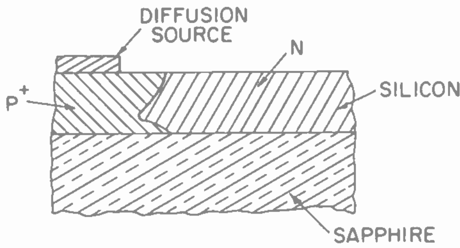

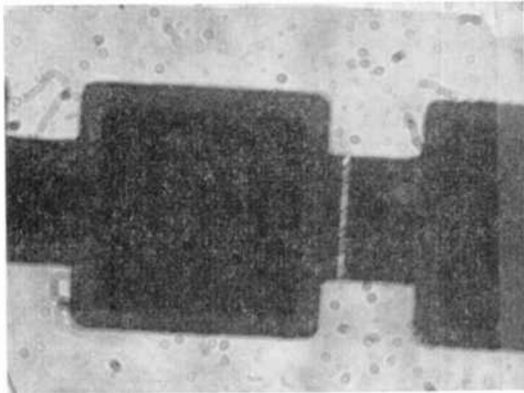

Fig. 6—Schematic representation of doping profile, and measured avalanche emission for SOS diode in which rapid diffusion has taken place at the silicon-sapphire interface.

case is a double line, as shown in Fig. 6, with the spacing between the avalanche emission lines being about 1.5 microns. Avalanche emission can be used to detect other gross features of the diffusion profile. For example, in cases where the time and temperature of the diffusion are so low that the diffusion front does not reach the sapphire interface, avalanche emission is observed from the junction curvature. This emission from the curvature is easily distinguished from that emitted by a through-diffused vertical junction, because it is faint and diffuse, and often extends under the metallization in our structure.

Defects in Parent SOS Films

Even more information about defects in the device structure can be obtained by driving the diode into second breakdown under controlled conditions. The precautions that must be taken to avoid catastrophic failure (e.g., vaporization of the device) during these measurements is discussed elsewhere.[5] When a device is driven into second breakdown, it will fail at its weakest point unless the device is sufficiently well fabricated that the breakdown results from the properties of the silicon. Consequently, we can learn about the defect structure of the device by observing how the devices on a given wafer fail when subjected to extremely high current densities. It is especially helpful to examine the avalanche emission from a device in which the failure mechanism has damaged, but not destroyed, the device. An example is shown in Fig. 7. The diodes on this wafer failed due to the formation

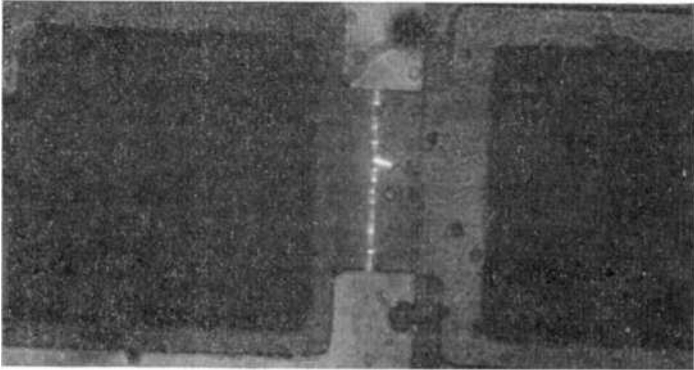

Fig. 7—Avalanche emission pattern of a diode that failed because of doping impurity migration.

of diffusion spikes that short out the electrically active region of the device under high current conditions. No diffusion spikes could be detected before the diodes were biased into second breakdown. This diode was operated in the second-breakdown mode for approximately one half of a second. During this time the diffusion spike formed and extended approximately 10 microns into the sample. Although the physical nature of the second-breakdown process results in intense local heating at the constriction site, the time and temperature involved in this experiment were grossly inadequate to cause a 10-micron diffusion in a normal SOS film. We therefore conclude that the film on

this wafer contained some form of defect that allowed the rapid local diffusion of impurity atoms under second-breakdown conditions. Again we emphasize that this conclusion could not be reached on the basis of the usual electrical characterization of the device.

Sites of High Thermal Generation

Dumin[4] has shown that properly fabricated SOS diodes can withstand being reverse biased into second breakdown for many hours without appreciable degradation. Sunshine[5] has shown that the avalanche process tends to maintain the uniformity of the current flow prior to second breakdown. Consequently, the junction temperature is rather uniform, but is slightly higher in the center of the sample than at the edges due to heat-flow considerations. Second breakdown occurs when some region of the junction becomes hot enough so that the thermally generated reverse current can take over the conduction process from avalanche generation. At this point, the avalanche becomes thermally quenched, the uniform current distribution collapses, and the current flows through a constriction in the junction. The thermal quenching of the avalanche will occur at that point in the junction where the thermal generation rate of carriers is highest. The position of the thermal quenching is experimentally determined by observing where the avalanche emission is extinguished.

For most devices, the distribution of generation centers is uniform across the width of the junction, and the thermal quenching takes place in the center of the junction, where the temperature is highest. The 34-mA photomicrograph shown in Fig. 4 is an example of this behavior. The light emission in the center of the junction of this sample is due to incandescence. However, we have seen cases where the quenching takes place at the edges of the sample, even though doping irregularities at the edges could not be detected from the avalanche emission pattern. We concluded that the edges of these diodes contain a high density of defects that serve as thermal generation centers. The detection of such defects is important in the fabrication of protection diodes, since these defects invariably reduce the power handling capability of the diode.

4. Light-Absorption Measurements

Use of Thermally Induced Changes in Light Absorption

The absorption of light by a semiconductor increases as the temperature increases. Consequently if a thin SOS device is illuminated

with transmitted light, it will appear more opaque when and where it becomes hot. This effect can be used to study the buildup of local heating in operating devices.[5] Since local heating is several orders of magnitude higher at a point of avalanche generation—where both j and E are high—than in the surrounding regions, observation of thermally induced changes in optical absorption can be used to study junction perfection in a way very similar to avalanche emission. The absorption technique can also be used in high-resistivity material, where the avalanche emission is too faint to be useful.

There is one important difference between the absorption and emission techniques. Local defect sites where significant heating takes place cannot be distinguished from their surroundings using dc biasing because of temperature diffusion. However, these sites of local thermal generation are readily observed using pulse techniques. The sample is biased with a pulse that is much shorter than the appropriate thermal diffusion relaxation time. The time development of the heating is determined by photographing the sample illuminated with an extremely short laser flash during the bias pulse. In addition to being useful for investigating junction uniformity, this pulse technique is also quite valuable in studying the time and spatial development of a second breakdown filament. We expect it to be useful for evaluating the ability of protection diodes to withstand excursions into second breakdown.

Pulse Bias Waveforms

The bias waveforms for a typical pulse experiment are illustrated schematically in Fig. 8. A reverse-bias constant-current pulse is applied to the device, and the resulting voltage is monitored. Three regions are evident in the voltage characteristic. First of all, from the application of the pulse at $t = 0$ until the delay time τ_D, the voltage increases with time. This delay time is a strong function of the applied current for any diode structure. Next, from $t = \tau_D$ until $t = \tau_D + \tau_F$, where τ_F is the formation time, the voltage decreases as the current constriction and negative resistance form. Finally, from $t = \tau_D + \tau_F$ until the end of the current pulse, the voltage remains nearly saturated at its sustaining level. Each of these three time domains corresponds to a different physical situation, and each can provide useful information about the device structure. For this discussion we will consider only the first two time regions.

Avalanche Generation Region

During the time between initiation of the pulse and the delay time,

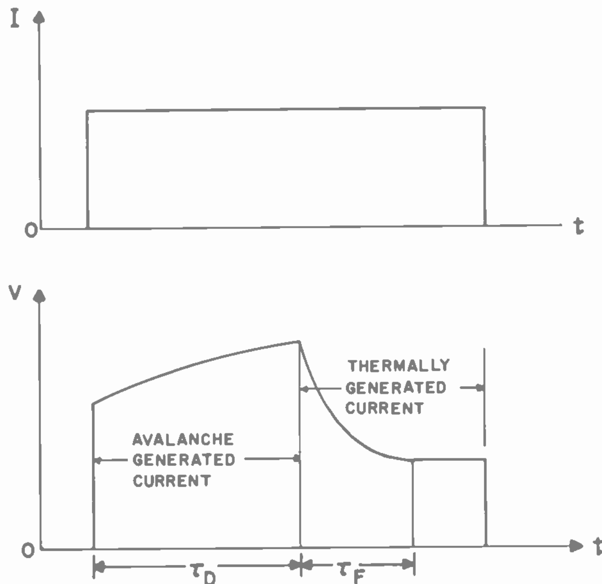

Fig. 8—Bias waveforms for typical pulse experiment.

the current is generated more or less uniformly in the junction by the avalanche process. Since both the current density and the electric field are extremely high at avalanche generation sites, heating builds up much more rapidly at these sites than in the surrounding regions. If the bias is high enough, the delay time is less than the time required for any significant thermal diffusion to take place, and the local temperature buildup remains confined to the regions of avalanche generation. By stroboscopically illuminating the diode with transmitted light, the local heating can be observed as an apparent darkening of the sample. Thus, examining the diode in this fashion provides much the same information as the dc avalanche-emission measurements. Examples are shown in Figs. 9 and 10. In Fig. 9 the delay time is about 30 microseconds, and in Fig. 10 it is about 40 microseconds. Notice that the avalanche is substantially more uniform in the diode shown in Fig. 10 than in that shown in Fig. 9.

Constriction Formation Region

At time τ_D, the current generation switches in typically less than 100 nanoseconds from an avalanche mechanism to a thermal mechanism.

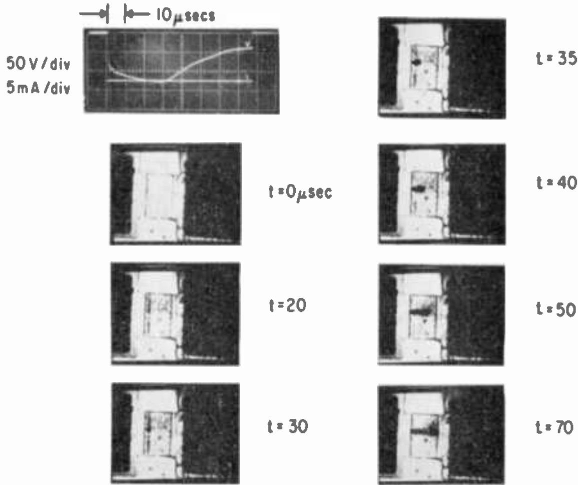

Fig. 9—Stroboscopic photographs and bias waveform of medium-length diode undergoing reverse-bias thermal switching at a junction temperature greater than the intrinsic temperature.

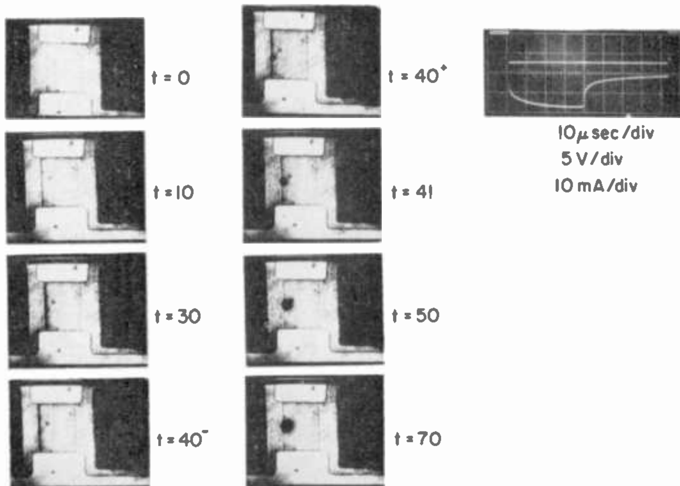

Fig. 10—Stroboscopic photographs and bias waveform of a medium-length diode undergoing reverse-bias thermal switching at a junction temperature less than the intrinsic temperature.

The thermal generation process is intrinsically unstable, and current constrictions develop. Therefore, for times greater than τ_D, the current is generated thermally in a narrow region of the junction.

The time and spatial development of the constriction also provides information about the perfection of the diode structure. Typical behavior is shown in Fig. 9. First of all, note that the filament forms at a weak spot in the junction, where intense heating occurs even prior to second breakdown. In many wafers, the constriction forms at the edge of the sample, and the sample burns out prematurely. This defect, when discovered, can be corrected by properly modifying the processing. Next note that the constriction elongates into the ohmic region of the sample until it reaches the N^+ contact. This elongation process continues only as long as the power density at the top of the constriction is sufficient to heat the material above its intrinsic temperature.[5] As soon as the power density at the constriction is insufficient for the material to reach its intrinsic temperature, the current spreads to uniform ohmic conduction. The velocity of the propagating high-temperature edge of the constriction is determined by how rapidly the material in the path of the constriction can be turned intrinsic. Nonuniformities in this material are detected by observing the constriction front speeding up or slowing down as it traverses ohmic region.

In addition, a rough comparison between the constriction temperature and the intrinsic temperature of the series material can be made by observing how much and how fast the filament elongates. Figs. 9 and 10 show two extremes. In Fig. 9 the constriction temperature is much higher than the intrinsic temperature, and the current remains tightly constricted as it elongates into the ohmic region. For the diode in Fig. 10, on the other hand, the constriction temperature is less than or comparable to the intrinsic temperature, and no elongation of the constriction into the ohmic region can occur. In this case, the low constriction temperature most likely results from a uniform but high density of defects at the silicon-sapphire interface. Thus, the way that the constriction develops provides additional information about thermal generation centers in the junction.

Homogeneity of Parent Semiconductor Material

Finally we point out that the uniformity of the parent semiconducting film can be investigated using the pulsed-light absorption technique. In this case, ohmic contacts are supplied to a strip of material usually about 3 mils wide and 6 mils long. A high current pulse is passed

through the sample, and the uniformity of the darkening is observed. It is very often found that the heating is not completely uniform across the resistive structure, indicating that the conductivity of the parent silicon is not uniform.

Conclusions

A variety of optical techniques for investigating the perfection of silicon devices on insulating substrates has been discussed. These techniques provide a means to quickly and nondestructively investigate microscopic imperfections in device structures with optical resolution. Imperfections that can be investigated include nonuniformities in the junction, diffusion spikes, sites of localized breakdown (especially at the edges of the sample), nonuniformities in the diffusion profile, inhomogeneities in the parent silicon film, and regions of high thermal generation. In general, these defects are insensitive to detection by electrical means. The optical techniques should be very valuable in evaluating processing procedures for silicon-on-insulator devices, and in the development of protection diodes for SOS memory circuits.

References:

[1] J. F. Allison, D. J. Dumin, F. P. Heiman, C. W. Mueller, and P. H. Robinson, "Thin-Film Silicon: Preparation, Properties and Device Applications," **Proc. IEEE,** Vol. 57, p. 1490 (1969).

[2] G. W. Cullen, "Preparation and Properties of Chemically Vapor Deposited Silicon-on-Sapphire and Spinel," to be published, **J. Crystal Growth.**

[3] J. E. Meyer, Jr., J. R. Burns, and J. H. Scott, Jr., "High Speed Silicon-on-Sapphire 50 Stage Shift Register," **1970 International Solid-State Circuits Conf. Digest,** p. 200 (1970).

[4] D. J. Dumin, "Emission of Visible Radiation from Extended Plasmas in Silicon Diodes During Second Breakdown," **IEEE Trans. Electron Devices,** Vol. ED-16, p. 479 (1969).

[5] R. A. Sunshine, **Avalanching and Second Breakdown in Silicon-on-Sapphire Diodes,** Doctoral Thesis, Princeton University, Princeton, N. J., 1970.

[6] R. L. Rogers, G. S. Briggs, W. N. Henry, R. E. Simon, R. L. Van Asselt, E. Cave, F. C. Duigon, A. D. Cope, and G. A. Morton, "Silicon Intensifier Target Camera Tube," **1970 IEEE International Solid State Circuits Conf. Digest,** p. 176 (1970).

[7] D. J. Dumin and R. S. Silver, "Diffused Diodes in Silicon-on-Sapphire," **Solid. St. Electronics,** Vol. 11, p. 353 (1968).

[8] R. Newman, W. C. Dash, R. N. Hall, and W. E. Bursh, "Visible Light From a p-n Junction," **Phys. Rev.,** Vol. 98, p. 1536 (1955).

[9] H. Kressel, "A Review of the Effect of Imperfections on the Electrical Breakdown of p-n Junctions," **RCA Review,** Vol. 28, p. 175 (1967).

[10] J. R. Burns and J. H. Scott, Jr., "Silicon-on-Sapphire Complementary MOS Circuits for High Speed Associative Memory," **AFIPS Conf. Proc.,** Vol. 35, p. 469 (1969).

Symmetrical Trough Waveguide Nonresonant Ferrite Isolators and Steerable Antenna

C. P. Wen, RCA Laboratories, Princeton, N. J.

Abstract—A Novel symmetrical trough waveguide narrow-band isolator whose operation is based on mode coupling and wave-interference principles has been demonstrated at X-band frequencies. A substantial reduction in the bias magnetic field requirement compared to that of conventional ferrimagnetic resonant isolator has been achieved. The field-reduction techniques have important potential applications at mm-wave frequencies where the bias field requirement for ferrite resonant isolators is beyond the capability of normal permanent magnets. The configuration of an electronically steerable trough waveguide antenna is also proposed.

Introduction

Symmetrical trough waveguides[1] were found to be practical transmission lines over a decade ago. The operation of symmetrical trough waveguide nonreciprocal ferrite devices was recently demonstrated, and the unconventional open-waveguide system was suggested for mm-wave hybrid integrated circuits.[2] It has long been recognized that any asymmetry introduced in a trough waveguide will cause power conversion from the dominant symmetrical mode to high-order asymmetrical modes, which will in turn radiate through the open side into space.

This paper describes a novel symmetrical trough waveguide narrow-band isolator whose operation is based on mode coupling and wave-interference principles. Partial trade-off between the operating frequency bandwidth and the isolation characteristics is shown to be feasible. Nearly complete isolation conditions can be achieved with relatively weak coupling between modes at certain discrete frequencies of circuit resonance. The interference effect observed is found to be analogous to that of optical interferometers. The reduction in dc applied magnetic field in this type of isolator, compared to the requirement imposed by ferrimagnetic resonance in conventional isolators, becomes a distinct advantage in high-frequency microwave devices. In

addition, the feasibility of using a symmetrical trough waveguide as a radiating element is demonstrated. An electronically-steerable symmetrical trough waveguide antenna for mm-wave radars is proposed.

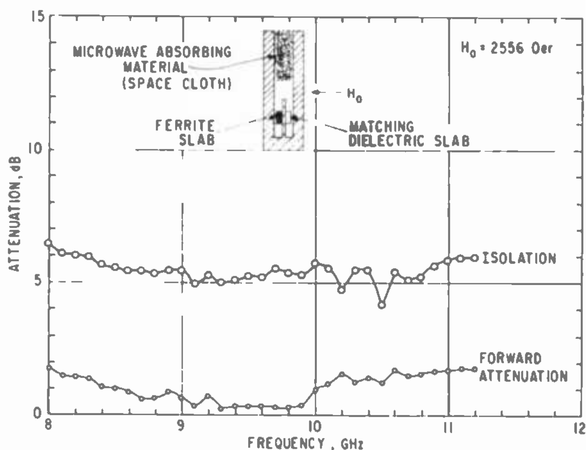

Fig. 1—A symmetrical trough waveguide nonresonant isolator and its performance with the odd mode terminated.

Experiments

A basic symmetrical trough waveguide isolator (antenna) is shown in Fig. 1, together with curves of its performance. A slab of gyromagnetic material (Trans Tech G-113 YIG, $0.191 \times 0.382 \times 10.16$ cm) and a matching slab of low-loss dielectric (STYCAST K-15) of the same dimensions are placed in the opposite troughs of a symmetrical trough waveguide 0.127 cm from the bottom. (The center ridge is 1.143 cm high, 0.127 cm wide, the slots are 0.254 cm wide and the side walls are 1.60 cm high.) The trough waveguide section is terminated at both ends with OSM coaxial connectors. Symmetry of the system is destroyed by the application of a magnetic field H_o, which causes a differential phase retardation of signals propagating in the ferrite-loaded and dielectric-loaded troughs in the isolation direction. The signals traveling in the forward direction do not experience the differential phase retardation because of the nonreciprocal characteristics of the ferrite slab. When the side walls of the trough waveguide are extended upward and the opening is terminated with a good microwave absorber (space cloth), the application of a bias field of 2556 Oe results in approximately 5.5 dB isolation and less than 2 dB forward attenuation between 8.0 and 11.2 GHz. This magnetic field is small compared

to the 5140 Oe required for ferrimagnetic resonance at 10.32 GHz in this system.

When the extension of the side walls and the microwave absorber are removed, the forward attenuation characteristic of the isolator remains practically unchanged (Fig. 2). With an applied field of

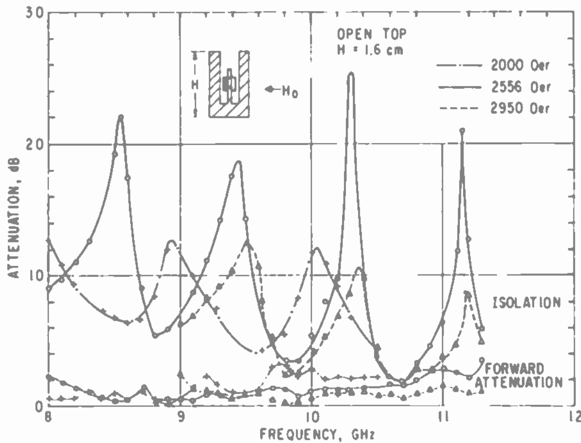

Fig. 2—Performance of a symmetrical trough waveguide isolator with open top at different magnetic-bias conditions.

2556 Oe, isolation is found to increase by 15 dB or more at discrete frequencies over that shown in the previous figure. The periodic structure persists in all three isolation-versus-frequency curves for applied fields of 2000, 2556, and 2950 Oe. The frequency intervals between the absorption peaks are observed to decrease with increasing magnetic field bias, while the absorption peaks are at a maximum at the intermediate bias field of 2556 Oe. Coupling between the even mode and the odd mode is found to increase with the applied magnetic field H_o. These results suggest the existence of strong circuit resonances, or wave-interference effects, in the waveguide system when the radiating odd mode is not terminated.

The dependence of the wave-interference effects on the nature of the discontinuity experienced by the odd mode can be further examined by changing the boundary conditions at the open side of the waveguide. A metallic cover plate with a 0.127-cm-wide slit cut lengthwise is employed. The performance of the symmetrical trough waveguide isolator with the cover plate is shown in Fig. 3 as a function of frequency. Besides the three nearly equally spaced absorption peaks, two

other isolation maxima are observed at 8.48 and 10.55 GHz. The appearance of the additional peaks on the isolation-versus-frequency curve suggests that two different types of interference effects are responsible for these absorption maxima.

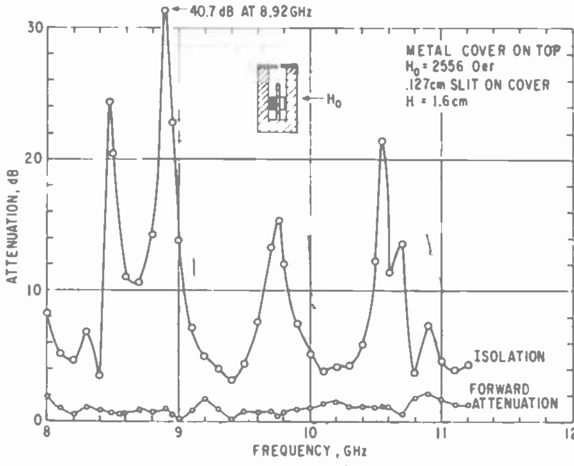

Fig. 3—Performance of a symmetrical trough waveguide isolator covered by a metal plate with a 0.127-cm slit.

Nature of Radiating Odd Mode

Before any attempt is made to identify the interference effects responsible for the absorption peaks, the nature of the radiating odd mode in the unbalanced symmetrical trough waveguide section loaded with ferrite and dielectric slabs has to be clarified. The field configuration of the odd mode in the dielectric loaded trough waveguide[4], is similar to one half of the TE_{20} mode in a dielectric-loaded parallel-plane waveguide. The electric field rises from the bottom of the troughs to a maximum and then decays exponentially toward the opened top, as shown in Fig. 4. The rf signal propagating in the odd mode leaks out gradually from the top, because of the evanescent nature of field configuration and the finite height of the side walls.

Information about the propagation characteristics of the odd mode may be obtained by measuring the far-field radiation pattern of the waveguide section using a standard horn. The direction of radiation shown in the sketch included with Table 1 is evaluated by drawing a line passing through the centroid of the lobes and the midpoint of the

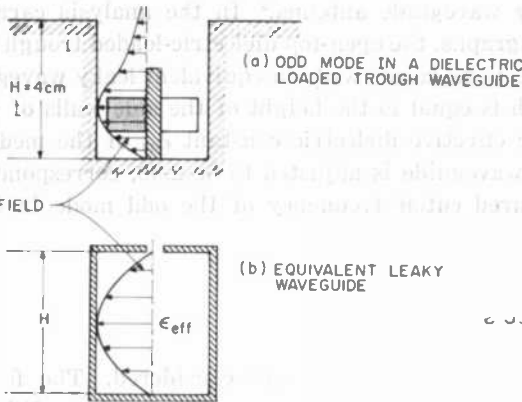

Fig. 4—Field configuration of the odd mode in a dielectric-loaded trough waveguide and the equivalent leaky waveguide.

trough waveguide section. The angle θ between the normal of the trough waveguide antenna and the radiating direction is given in Table 1, along with the calculated values. The calculations were carried out based on the formula[5] $\theta = \cos^{-1} (f_c/f)$ where $f_c = 6.06$ GHz is the cut-off frequency determined using the angle θ measured at 8.57 GHz. The good agreement shown in Table 1 indicates that a symmetrical trough waveguide may be converted into an antenna if the even-mode symmetry is destroyed.

The propagation characteristics of the odd mode can be closely approximated by the simple relationship governing the behavior of an

Table 1—Radiation Direction of a Symmetrical Trough Waveguide Antenna

Frequency, GHz	8.57	9.45	10.32	11.16
Angle, Degrees (Measured)	45°	51°	54°	57°
Angle $\theta = \cos^{-1} \frac{f_c}{f}$	45°	50.1°	54.1°	57.1°
$f_c = 6.06$ GHz, Evaluated at 8.57 GHz				

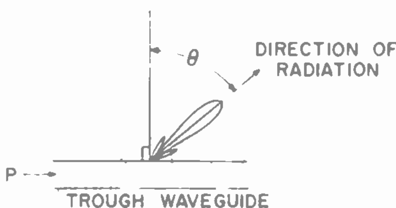

equivalent leaky waveguide antenna.[5] In the analysis carried out in subsequent paragraphs, the open-top dielectric-loaded trough waveguide shown in Fig. 4a is replaced* with an equivalent leaky waveguide (Fig. 4b) whose width is equal to the height of the side walls of the trough waveguide. The effective dielectric constant ϵ_{eff} of the medium filling this equivalent waveguide is adjusted to be 2.39, corresponding to the 6.06 GHz measured cutoff frequency of the odd mode in the trough waveguide.

Interference Effects

Two types of interference effects are considered. The first type is analogous to that of the optical Lummer Gercke plate. Whenever the signal from the odd mode undergoes a multiple of 2 π phase shift as it impinges on the top plane, as shown in Fig. 5, constructive inter-

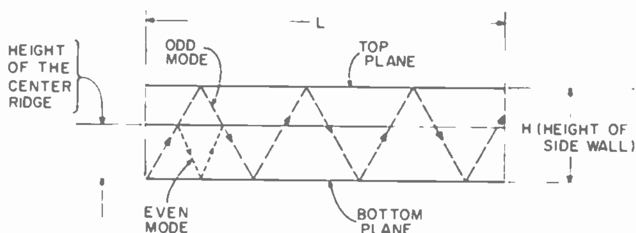

Fig. 5—Side view of a symmetrical trough waveguide showing the propagation of the even and the odd modes.

ference results, and there will be a maximum transfer of power from the dominating even mode through the radiating odd mode into free space. Nearly complete transfer of power is possible if the coupling between the even and odd modes is identical to the coupling between the odd mode and free space. This type of interference effect occurs when

$$\frac{H_{eff}}{\cos\theta} = \frac{n\lambda_o}{2}, \qquad [1]$$

* The replacement is justified because of the similarity in the field configurations in both waveguides and the excellent agreement between the measured far-field radiation pattern of the trough waveguide and the predictions based on the leaky waveguide antenna theory.

where n is an integer and H_{eff} is the effective width of the equivalent leaky waveguide

$$H_{eff} = H\epsilon_{eff}^{1/2} = \lambda_c/2.$$

Since $\cos\theta = f_c/f$, [2]

$$f_n^2 = nf_c^2 \qquad [3]$$

where f_n is the frequency corresponding to the integer n in Eq. [1]. Based on the value of f_c evaluated using the radiation pattern measurements, maximum absorption is predicted to take place at $f = 6.06$ GHz, 8.56 GHz and 10.52 GHz, corresponding to $n = 1, 2, 3$ respectively. The predictions seem to fit the absorption peaks observed at 8.48 GHz and 10.55 GHz in Fig. 3 where the top of the trough waveguide is covered with a plate with a lengthwise slit. That these two peaks are missing in Fig. 2, where the odd mode couples strongly to free space, strengthens the notion that they are similar in origin to the optical Lummer Gercke plate (which arises from a circuit discontinuity in the transverse direction alone and requires relatively small loss per pass). The origin of the other absorption peaks at 8.90 GHz, 9.77 GHz and 10.72 GHz in Fig. 3 are not predicted by these calculations.

The phase velocity of the odd mode may be perturbed by increasing the height of the side walls of the trough-waveguide section. In Fig. 6, the performance of the isolator at 2556 Oe bias field is shown as a function of frequency, with the height of the side walls as a parameter. The frequency intervals between absorption peaks are found to remain relatively independent of the given bias condition, but they tend to increase with the height of the side walls. An attempt was made to relate these and the other absorption peaks in Fig. 3 with circuit resonances of the odd mode introduced by the longitudinal discontinuity of the trough waveguide section, the second type of interference effect considered here. Assuming that the guided wagelength of the asymmetrical mode at a frequency f is λ_g, resonance occurs at

$$\frac{L_{eff}}{\lambda_g} = \frac{m}{2}, \qquad [4]$$

where L_{eff} is the effective length of the trough waveguide section between the two OSM connectors and m is an integer. The resonance frequency f_m is simply

$$f_m^2 = \left(\frac{m}{2L_{eff}}\right)^2 c^2 + f_c^2. \qquad [5]$$

Table 2 shows a number of expected resonant frequencies f_m and the cutoff frequency f_c for the odd mode with the side wall of the symmetrical trough waveguide as a parameter. The frequencies corresponding to the absorption peaks in Fig. 3 and Fig. 6 are also included for comparison purposes. The cutoff frequency of the open-top trough waveguide with $H = 1.6$ cm is taken to be 6.06 GHz based on the results from the radiation pattern measurements. The effective length L_{eff} and the resonant frequencies are determined using the best fit of experimental data points (designated with an asterisk in Table 2). The cutoff frequency for the case with the cover plate is obtained from Eq. [5], assuming the effective length is unchanged with the introduction of the cover. The cutoff frequencies corresponding to the waveguide with extended side walls are calculated assuming that the effective dielectric constant ϵ_{eff} of the medium filling the equivalent leaky waveguide remains 2.39 with the small addition in the width of the waveguide. The effective lengths of the resonators are found to be slightly longer than the actual length, because the signals propagating in the forward direction do not suffer the additional negative phase retardation caused by the negative effective permeability of the ferrite below the ferrimagnetic resonance.[6] The resonant frequencies predicted using Eq. [5] show remarkably good agreement with the frequencies corresponding to the absorption peaks.

Conclusions

It is concluded that the absorption peaks observed in the isolation direction of a symmetrical trough waveguide nonresonant isolator are caused by circuit resonances of the radiating asymmetrical mode. The first type of interference is caused by the discontinuity in the transverse dimension alone, similar to the phenomenon observed in an optical Lummer Gercke interferometer. The second type of interference is a result of discontinuity in both the length and the height of the trough waveguide.

From the practical standpoint, a trade-off between the operating frequency bandwidth and the isolation characteristics in a symmetrical trough waveguide nonresonant isolator has been demonstrated experimentally. The reduction in the bias magnetic field requirement compared to that of conventional ferrimagnetic resonant isolator becomes

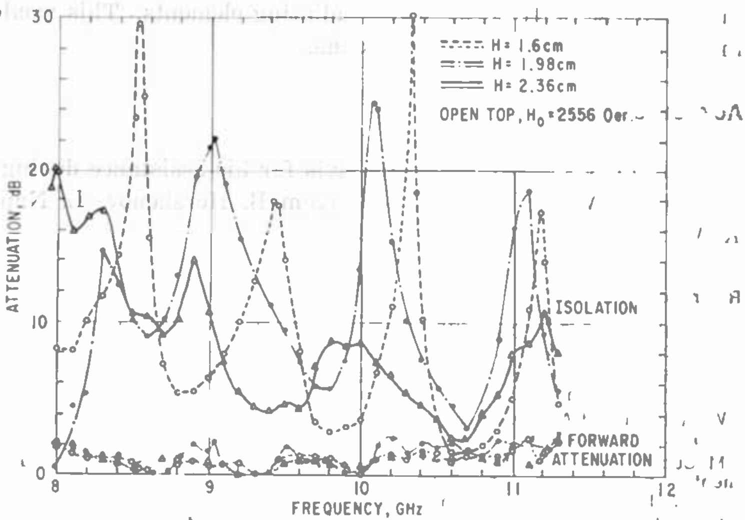

Fig. 6—Performance of a symmetrical trough waveguide isolator with open top (the height of the side walls is a parameter).

a distinct advantage for this novel device configuration. In addition, if many of these electronically controlled radiating elements are connected alternately in series with sections of ferrimagnetic differential phase shifters, the radiation pattern may be altered by selectively vary-

Table 2—Theoretical and Experimental Expected Resonant Frequencies Corresponding to the Absorption Peaks

H (cm)	1.6		1.6		1.981		2.362	
f_c (GHz)	6.06		6.77		4.90		4.11	
	Open Top		Cover Plate (0.127cm Slit)		Open Top		Open Top	
m	f_m (GHz)	$f_m{}^1$ (GHz)	f_m (GHz)	$f_m{}^1$ (GHz)	f_m (GHz)	$f_m{}^1$ (GHz)	f_m (GHz)	$f_m{}^1$ (GHz)
5	8.53	8.52	8.93	8.90				
6	9.41	9.43	9.77	9.77*	9.00	9.00	8.83	8.90
7	10.33	10.33*	10.72	10.70	10.07	10.07*	10.0	10.0*
8	11.32	11.17			11.19	11.10	11.20	11.15
L_{eff}	12.6 cm		12.6 cm		11.91 cm		11.5 cm	

Length of section = 10.16 cm

$f_m{}^1$ Frequency corresponding to measured absorption peaks

f_m Calculated resonance

* Datum point employed for the computation of f_m

ing the phase shift between the radiating elements. This would result in an electronically steerable antenna.

Acknowledgment

The author wishes to thank H. Davis for his assistance during experimentation. Valuable suggestions from B. Hershenov, L. Napoli, and K. Weller are also acknowledged.

References

[1] K. S. Packard, "The Cutoff Wavelength of Trough Waveguides," **IEEE Trans. PGMTT**, Vol. 6, No. 4, p. 455, Oct. 1958.

[2] C. P. Wen, "Integrated-Circuit Metalized Plastic Symmetrical Millimeter Trough Waveguide System with Nonreciprocal Elements," **RCA Rev.**, Vol. 30, No. 4, Dec. 1969.

[3] W. Rutman and A. A. Oliner, "Asymmetrical Trough Waveguide Antenna," **IEEE Trans. PGAP**, Vol. 7, No. 2, p. 153, April 1959.

[4] M. Sucher and J. Fox, **Microwave Research Institute Handbook of Microwave Measurements**, Vol. II, Third Edition, Polytechnic Press of the Polytechnic Institute of Brooklyn, John Weiley & Sons, Inc.; New York, 1963.

[5] R. C. Honey, "Line Sources and Linear Arrays for Millimeter Wavelengths," **Proc. Symp. on Millimeter Waves**, p. 563, Polytechnic Press, 1959.

[6] B. Lax, K. J. Button, **Microwave Ferrites and Ferrimagnetics**, McGraw-Hill Book Company, Inc., New York, 1962.

RF Sputtered Transparent Conductors The System In_2O_3–SnO_2

John L. Vossen, RCA Laboratories, Princeton, N.J.

Abstract—An rf sputtering technique for the deposition of tin-doped indium oxide transparent conductors has been developed. The technique employs the creation of anion vacancies in the films in addition to donor doping by tin oxide. Films as deposited exhibit transmission in the visible, averaging 90% or higher for sheet resistivities greater than 15 ohms/square. Upon annealing at 550°C in air for two hours, the resistivity increases by a factor of 2–7, depending upon the initial resistivity, but the average transmission remains unchanged. The resistivity change is a result of surface oxidation that eliminates some of the anion vacancies created during deposition. The films are fine grained, smooth polycrystals. Dopants other than Sn yield higher resistivity and lower optical transmission.

Introduction

Previously, rf sputtered transparent conductors in the system SnO_2-Sb_2O_3 were reported[1] to yield transmission greater than 80% in the visible range of wavelengths for films having sheet resistivities greater than 500 ohms per square. Conductivity was induced in the films by donor doping rather than by creating anion vacancies, because the latter was found to be less controllable.

For certain applications, the conductivity that can be achieved for a given transmission was found to be inadequate. Accordingly, a search was made to find a material system that provides greater conductivity than the SnO_2-Sb_2O_3 system for equivalent transmission in the visible. Based on a variety of considerations, the material system selected for this investigation was In_2O_3-SnO_2.

Pure In_2O_3 films prepared by reactive dc sputtering[2] from an indium target yielded transmission of only 75% at a sheet resistivity of 1500 ohms/square. Sinclair, et al[3] used In_2O_3 as an acceptor dopant in SnO_2 films and found the resistivity to be higher than for pure SnO_2. However, their investigation included only small In_2O_3 additions

(up to 7 mole %). This paper covers the compositional range 10 to 50 mole % SnO_2 in In_2O_3. In the present case, SnO_2 is a donor impurity in the In_2O_3.

The oxidation is self-limiting[4] in thickness at any given temperature. This effect suggests that anion vacancies can be created and maintained stably with this material, i.e., subsequent oxidation processes should tend to form a passivation layer on the top surface of the film, limiting further oxidation at lower temperatures.

Experimental Techniques

Sputtering targets were prepared by dry mixing reagent grade In_2O_3 and SnO_2 powders, pressing the powder into shallow nickel dishes that were pre-coated with a thick film of rhodium, which acts as a reaction barrier. The powders were then lightly sintered in air at 900°C for one hour. This method of target preparation has proven very useful when a wide range of compositions are to be investigated. It should be noted, however, that targets prepared in this fashion are extremely porous and require careful outgassing before each sputtering run to ensure that stable conditions prevail. These and other precautions to be observed with these targets have been described.[1]

The sputtering equipment has been described previously.[5] In operation, shields are placed close to the target to prevent sputtering any exposed rhodium or nickel from the dish.

To determine the optimum target composition, films were deposited to a thickness of 1200 Å in pure oxygen. These runs yielded films with a minimum of anion vacancies and are taken to be the stable condition of the material. All films were deposited under the following sputtering conditions:

Oxygen Pressure: 40 millitorr
Peak-to-Peak rf Voltage: 4300 volts
Average Sheath Potential: −800 volts
Magnetic Flux Density: 25 gauss
Target-Substrate Separation: 2.7 cm

Under these conditions, the deposition rate was 40 ± 2 Å/min. Fig. 1 shows the variation of sheet resistivity as a function of target composition for these films. At the minimum in the resistivity curve (20 mole % SnO_2), the sheet resistivity of 3,000 ohms/square is higher than an equivalently thick 90 SnO_2-10 Sb_2O_3 by a factor of two.[1] From the data in Fig. 1, the composition selected for further study was 80 mole % In_2O_3-20 mole % SnO_2. All data following are for that composition.

To produce anion vacancies in the films, pure argon was used as the sputtering gas. It is known that both In_2O_3 and SnO_2 are chemically reduced partially when sputtered in argon.[5] Unless otherwise indicated, all sputtering runs in argon were conducted under the following conditions:

Argon Pressure: 30 millitorr
Peak-to-Peak rf Voltage: 4300 volts
Average Sheath Potential: −850 volts
Magnetic Flux Density: 25 gauss
Target-Substrate Separation: 2.7 cm

The deposition rate was 150 ± 5 Å/min. These conditions were used for convenience only. It was found possible to deposit this material at rates up to about 700-750 Å/min without recrystallization or excessive grain growth.

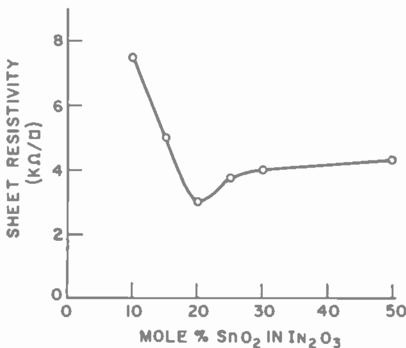

Fig. 1—Sheet resistivity versus target composition for 1000-Å-thick films deposited in pure oxygen.

Results and Discussion

Resistivity and Transmission

Fig. 2 illustrates the variation in transmission with wavelength and sheet resistivity of films as deposited. Figs. 3 and 4 show the effect on resistivity and transmission of annealing the films at 550°C for two hours in air. In all cases, the effect on transmission is to shift the peaks in Fig. 2 to lower wavelengths, but the average transmission over the visible range of wavelengths remains essentially unchanged. The curves are essentially interference patterns, and the wavelength

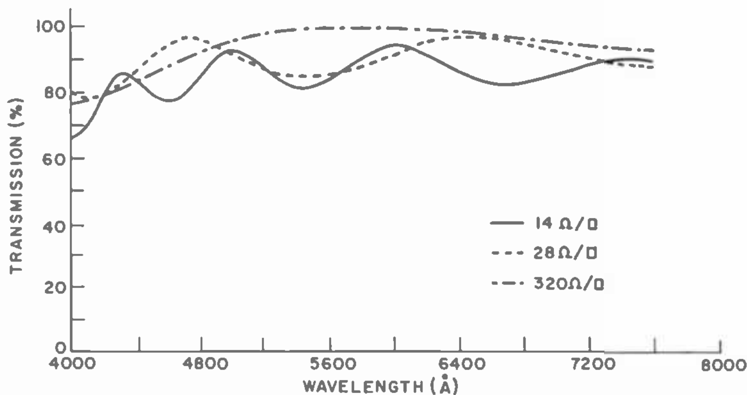

Fig. 2—Transmission versus wavelength for In_2O_3-SnO_2 films deposited in argon to different thicknesses.

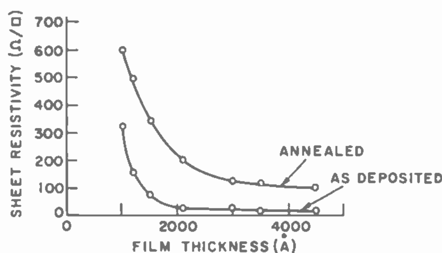

Fig. 3—Sheet resistivity versus film thickness for as-deposited and annealed In_2O_3-SnO_2 films.

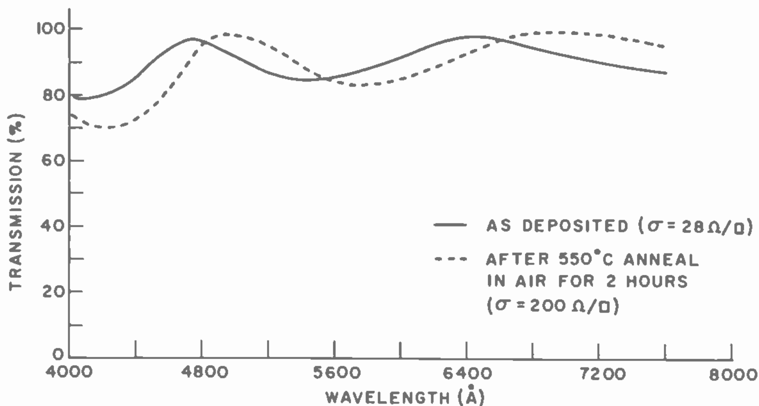

Fig. 4—Transmission versus wavelength for as-deposited and annealed In_2O_3-SnO_2 films.

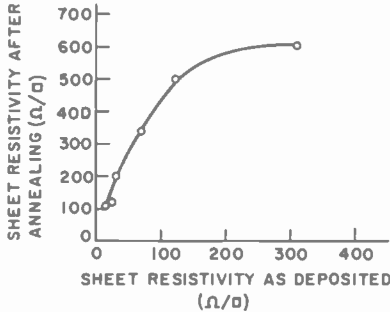

Fig. 5—Sheet resistivity after annealing versus sheet resistivity before annealing for In_2O_3-SnO_2.

shift implies a change in refractive index. For convenience, the annealed resistivity is plotted as a function of resistivity before annealing in Fig. 5.

For thickness greater than 2,000 Å, the bulk resistivity is constant (625 ± 5 μohm-cm as deposited; $4,600 \pm 100$ μohm-cm after annealing). SnO_2-Sb_2O_3 films of comparable thickness exhibit resistivities 3 to 4 times higher than these values. Thinner films exhibit much higher bulk resistivities (Fig. 6). The thickness at which this departure from constant resistivity occurs is far greater than that for metal films. It should be noted that annealing these films does not cause their resistivity to increase to the values for films deposited in pure oxygen. This tends to support the view that a passivating surface oxide is grown on the film surface.

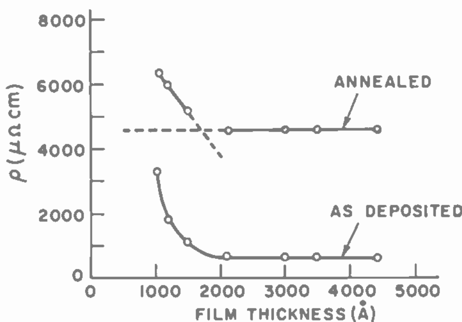

Fig. 6—Bulk resistivity versus film thickness for In_2O_3-SnO_2 as deposited and after annealing at 550°C for 2 hours.

Surface Morphology

The surface of the films produced by this technique are smooth when viewed in the scanning electron microscope (Fig. 7). There is no change in surface morphology after annealing at 550°C for two hours in air.

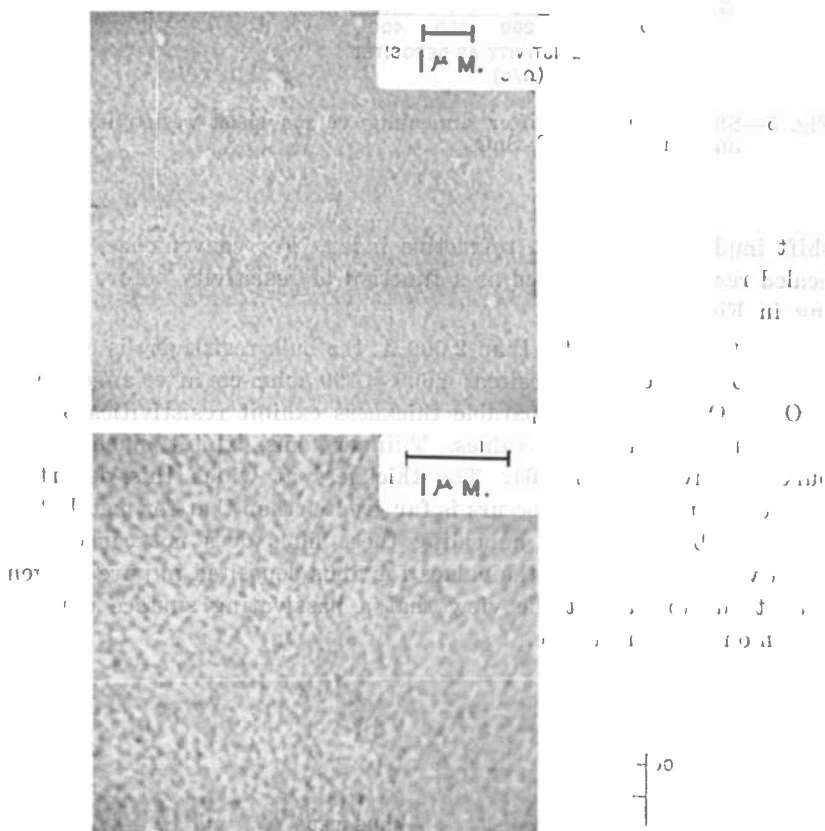

Fig. 7—Scanning electron micrographs of In_2O_3-SnO_2 ($t = 4000$ Å).

Crystal Structure

Electron diffraction analysis of films as deposited and after annealing reveal that the films are polycrystalline with a considerable amount of {100} preferred orientation (Fig. 8). The structure is cubic with a lattice parameter $a_o = 10.31$ Å as compared to bulk In_2O_3 (a_o

= 10.118).[6] No SnO_2 phases were detected, implying that the dopant replaces indium substitutionally in the In_2O_3 structure.

No difference between the annealed and as-deposited films was detected by electron diffraction.

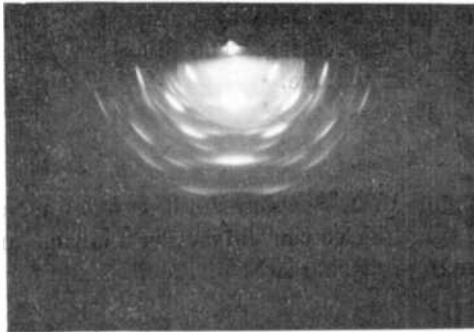

Fig. 8—Reflection electron-diffraction pattern of In_2O_3-SnO_2 film.

Other Dopants in In_2O_3

Several other dopants were tried in In_2O_3. None was found as effective as SnO_2. Table 1 lists these dopants and the results obtained. Annealing these films again produced increases in resistivity with little or no change in transmission.

Table 1—Characteristics of Donor-Doped, Anion-Deficient In_2O_3 Films (Film Thickness = 2500 Å)

Dopant	Concentration (Mole %)	Resistivity (ohm-cm)	Average Transmission (%)
SnO_2	20	6.25×10^{-4}	93
Sb_2O_3	10	2×10^{-2}	88
Sb_2O_3	20	1.7×10^{-2}	85
Bi_2O_3	10	2×10^{-1}	5
PbO_2	20	4.5	23
TiO_2	20	7.5×10^{-1}	96

Conclusions

Transparent conductors in the material system In_2O_3-SnO_2 exhibit minimum resistivity for equivalent transmission at a composition consisting of 80 mole % In_2O_3–20 mole % SnO_2. When rf sputtered in pure argon to produce anion vacancies, the films exhibit greater than

80% transmission in the visible for film resistivities greater than 15 ohms/square. Upon annealing the films in air at 550°C for two hours, the resistivity increases by a factor of 2 to 7 depending upon the initial resistivity; but the average transmission in the visible remains unchanged. The resistivity change is probably a result of surface oxidation that eliminates anion vacancies. Further annealing at or below 550°C produces no change in resistivity, leading to the conclusion that the oxide grown is self-passivating. The films are fine grained polycrystals and are smooth in texture.

Acknowledgments

The author wishes to thank B. J. Seabury for the scanning electron micrograph, W. C. Roth for the electron diffraction analysis, and J. J. O'Neill, Jr. for assistance in preparing some of the films and for several helpful discussions.

References:

[1] J. L. Vossen, **Proc. Third Symp. on Deposition of Thin Films by Sputtering**, University of Rochester, Rochester, N. Y., p. 80 (1969).

[2] L. Holland and G. Siddall, "The Properties of Some Reactively Sputtered Metal Oxide Films," **Vacuum**, Vol. 3, p. 375 (1953).

[3] W. R. Sinclair, F. G. Peters, D. W. Stillinger, and S. E. Koonce, "Devitrification of Tin Oxide Films (Doped and Undoped) Prepared by Reactive Sputtering," **J. Electrochem. Soc.**, Vol. 112, p. 1096 (1965).

[4] A. U. Seybolt, "Oxidation of Metals," **Adv. in Phys.**, Vol. 12, p. 1 (1963).

[5] J. L. Vossen and J. J. O'Neill, Jr., "RF Sputtering Processes," **RCA Review**, Vol. 29, p. 149 (1968).

[5] R. W. G. Wyckoff, **Crystal Structures**, Vol. II, 2nd Ed., p. 5, Interscience Publishers N.Y., N.Y. (1964).

Contrast Thresholds of Image-Intensifier-Aided Eye at Low Field-Luminance Levels

Illes P. Csorba, RCA Electronic Components, Lancaster, Pa.

Abstract—The contrast sensitivity of image-intensifier systems as a function of field luminance and spatial frequency is calculated. Limitations of resolution related to glass optics and the eye response are also considered.

Introduction

The ability of the human eye to see fine details of an object at low field-luminance levels may be improved by the use of an image-intensifier system such as shown in Fig. 1. In Fig. 1 the objective lens focuses a sharp image of the scene on the photocathode of the image-intensifier tube. The eye observes the intensified image through an ocular. Improved visibility is obtained because the light-gathering power of the objective lens is greater than that of the unaided eye and because the quantum efficiency of the photocathode is greater than

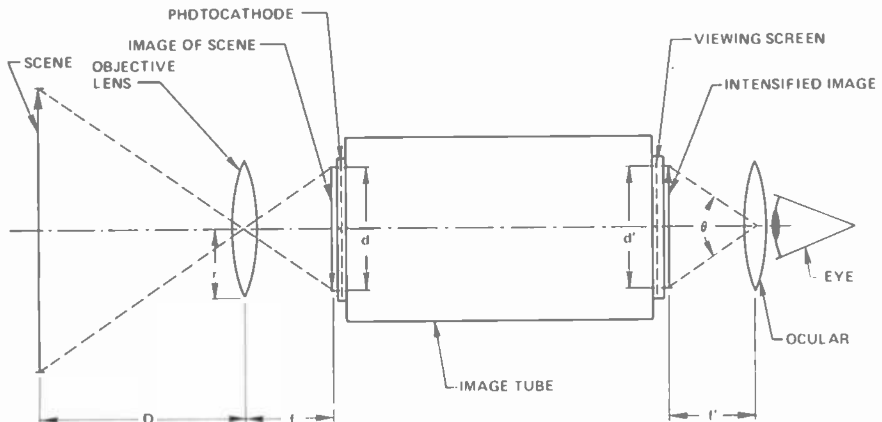

Fig. 1—Image-intensifier system.

that of the eye. Fundamental limitations of visibility occuring with the use of image intensifier are the statistical variation of photocathode current, the contrast transfer of the image intensifier, and the contrast sensitivity of the eye in the useful spatial-frequency domain.

Effect of Photocathode Current Fluctuation on Resolution

At very low photocathode illumination levels, the statistical variation of the photoelectron current limits the resolution R to the following value in line-pairs per millimeter:[1]

$$R = \frac{2.79 \times 10^{8}}{K} \frac{\sqrt{2}C}{\sqrt{1+C}} \sqrt{E_w' S t} \qquad [1]$$

where C is the contrast of a line pattern at the photocathode defined by

$$C = \frac{E_w' - E_b'}{E_w' + E_b'} \qquad [2]$$

In Eqs. [1] and [2], E_b' and E_w' are the photocathode illumination (in lumens per square centimeter) of the black and white lines, respectively, S is the photocathode sensitivity (amperes per lumen), t is the storage time (seconds) and K is the signal-to-noise ratio having a value of about 3.1 for a line length-to-width ratio of 5:1.

Usually the photocathode resolution is observed at the output screen of the image-intensifier tube. At the output screen the input contrast is modified by the contrast transfer of the image tube. In this case, therefore, the output image contrast must be used for the value of C in Eq. [1].

When a square-wave grating is viewed through an image intensifier, the field resolution as a function of field luminance and field contrast may be obtained by multiplication of Eq. [1] with the magnification of the objective lens ($f D^{-1}$), by replacement of the cathode contrast C with the product of the field contrast C_f and the contrast-transfer function of the image intensifier C_i (see Appendix), and by replacement of the photocathode illumination E_w' by the field luminance $E = E_w' r^{-2} f^2$. The field resolution R_f in line-pairs per meter then becomes

$$R_f = \frac{2.79 \times 10^{11}}{K} \frac{r}{D} \frac{\sqrt{2} C_f C_i}{\sqrt{1 + C_f C_i}} \sqrt{E S t} \qquad [3]$$

In Eq. [3], D is the object distance and E is the field luminance in lamberts.

Figs. 2(a) through (d) show the field resolution as a function of field contrast for four different objective lenses and a 100-meter object

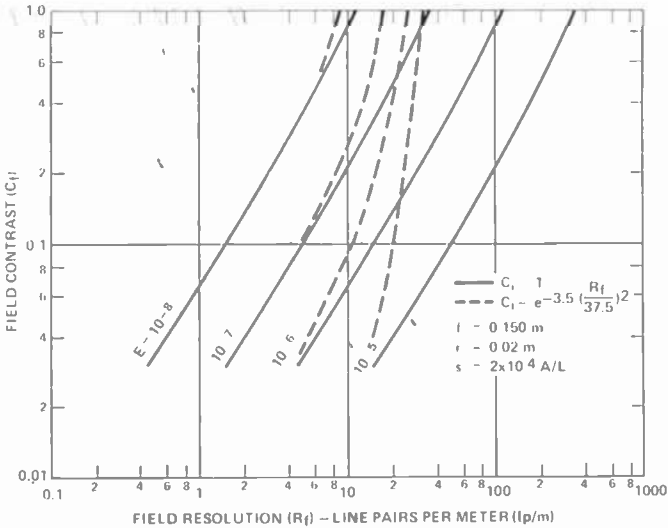

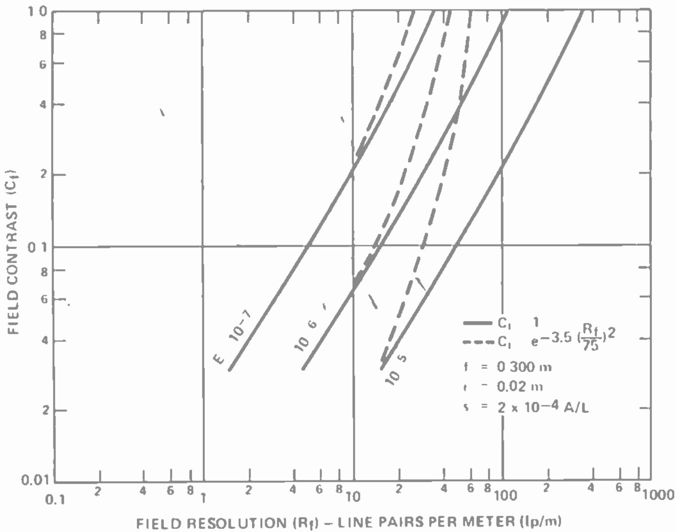

Fig. 2(a, b)—Field resolution as a function of field contrast C_f and field luminance for two different objective lenses. $D = 100$ m, $t = 0.2$ s, $K = 3.1$, and $R_i = 25$ line-pairs/mm.

distance. The solid lines represent the contrast thresholds for a C_t of unity (constant-contrast transfer in the useful spatial-frequency domain). The broken lines represent the contrast thresholds of image-intensifier systems having a Gaussian contrast-transfer function C_t

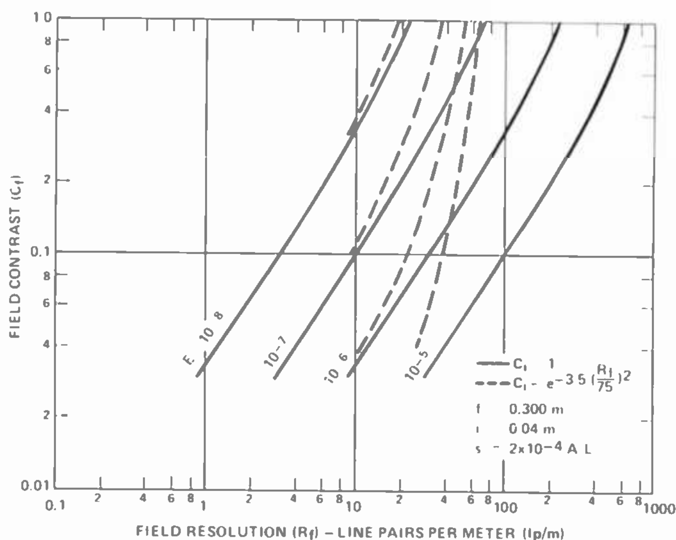

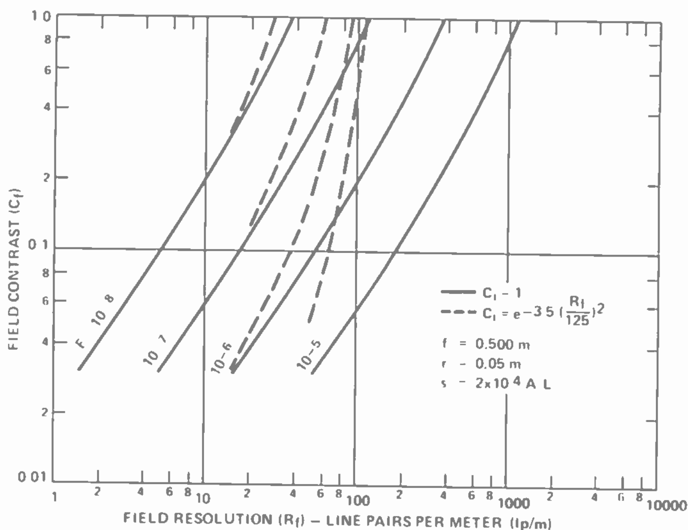

Fig. 2 (c, d)—Field resolution as a function of field contrast C_f and field luminance for two different objective lenses. Values for D, t, K and R_t are as for Fig. 2 (a, b).

given by

$$C_i = \exp\left[-3.5\left(\frac{R_f}{R_i M}\right)^2\right],$$

where M is the magnification of the objective lens and R_i is the limiting resolution of the image tube having a value of 25 line-pairs per millimeter. The broken lines were plotted by dividing the contrast values read at the solid line by the corresponding $C_i(R_f)$ values. For an object distance D other than 100 meters, the field-resolution values may be obtained by multiplying the abscissa by a factor of $100D^{-1}$

As may be concluded from Eq. [3], the resolution of an ideal image intensifier (C_i equal to unity) is independent of the focal length of the objective lens. However, the resolution of a practical image intensifier having a gradually descending contrast transfer function depends on the focal length, as indicated by Figs. 2(a) through (d).

The focal length also sets the magnification of the objective lens and consequently the field of view. Fig. 3 shows the relationship of the diameter of the photocathode of the image tube, the focal length of the objective lens, and the field of view. The field of view, together with the field resolution, determines the total amount of image detail transmitted through an image intensifier.

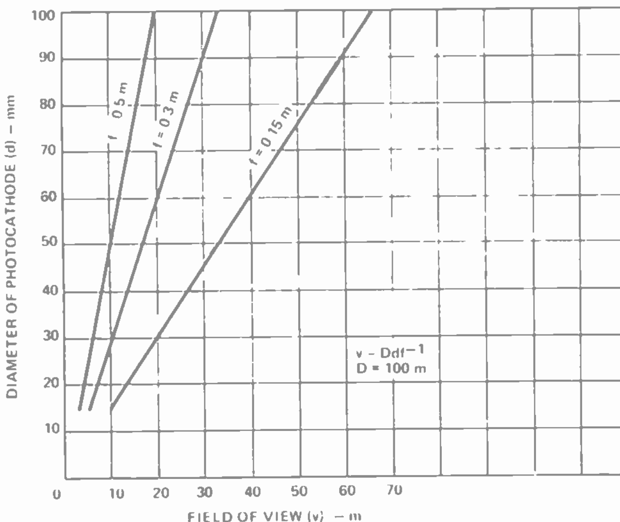

Fig. 3—Relationships of diameter of image-tube photocathode, focal length of objective lens, and field of view.

The Ocular and Eye Response

The function of the ocular is to magnify the intensified image so that the contrast loss caused by the eye response is minimized. Fig. 4 shows the response of the eye to square-wave gratings with a line length-to-width ratio of 10:1. The response curve was obtained by measuring the contrast thresholds of the eye as a function of spatial

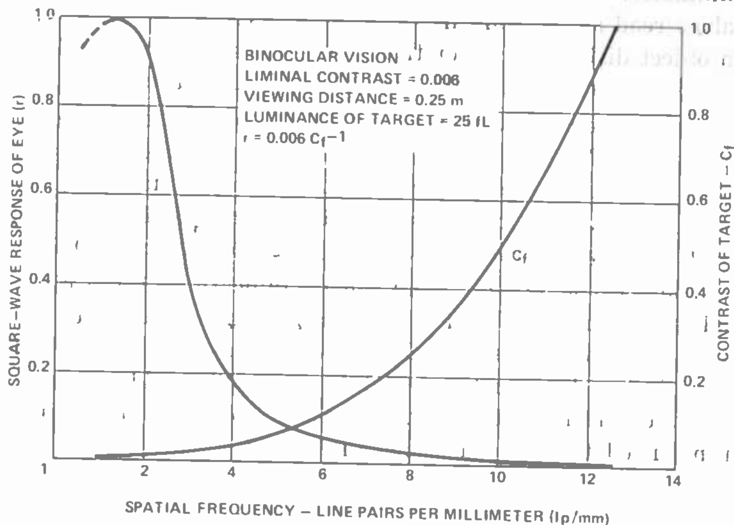

Fig. 4—Response of the eye to square-wave gratings.

frequency. The eye response r was obtained from the threshold contrast values C_f by the relationship (see Appendix):

$$r = 0.006\, C_f^{-1}, \quad [4]$$

where 0.006 is the liminal contrast that an average observer can detect. By use of a 10× ocular the contrast loss resulting from the eye response is at a moderate level up to 20 line-pairs per millimeter at the output screen. It appears that a further increase of magnification may completely eliminate the contrast loss caused by the eye at high spatial frequencies. However, in addition to the eye response, the field of view of the ocular must be considered. Fig. 5 shows the magnification M of a number of oculars as a function of viewing-screen diameter d' and angular field of view θ. The human eye, with motion of the eye

ball, can accept an angular field of view of about 60° to 70°. Therefore, if the requirements were to view a 40-millimeter output screen, the ocular magnification, as shown in Fig. 5, would have to be in the range of 7.2 to 8.7.

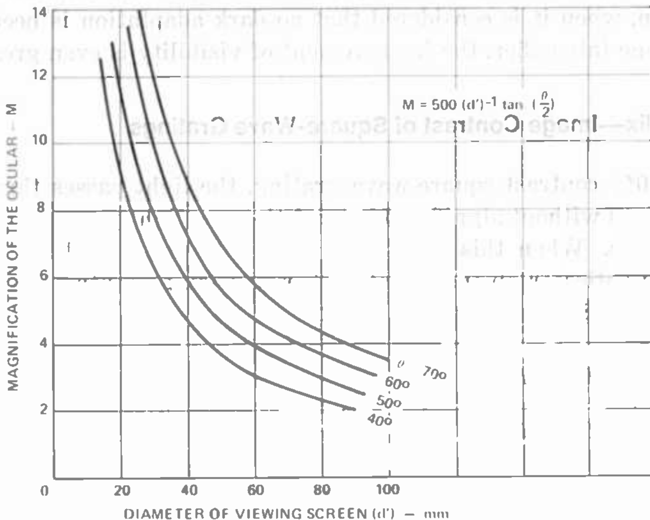

Fig. 5—Magnification of a number of oculars as a function of viewing-screen diameter and angular field of view.

Conclusion

Figs. 2(a) through (d) show that at field-luminance values lower than 10^{-7} lambert, and at low contrast values where visibility is most difficult, there is little difference between the performance of an ideal image intensifier having a constant contrast transfer in the useful spatial-frequency domain and a practical image intensifier. However, at higher field-lumance values, the contrast loss introduced by the contrast-transfer function of a practical image intensifier is appreciable. It is also important to recall that the contrast thresholds were obtained for a square-wave grating with a line length-to-width ratio of 5:1. It is easier to resolve longer lines. Experiments indicate that within the field of distinct vision of the motionless eye, the resolution is proportional to the square root of the length of the line.[1]

The improvement of visibility with the image intensifier over the unaided eye may be estimated to some degree by comparison of contrast

thresholds of Fig. 2 with the published contrast thresholds of the unaided eye.[2] At a field luminance of 10^{-7} lambert, and a contrast of 0.3, the resolution of the unaided eye is about 40 minutes of arc, or 0.86 line-pair per meter, at an object distance of 100 meters. Fig. 2(d) shows, however, that the image-intensifier-aided eye can resolve 35 line-pairs per meter, a 40.7-fold increase over the unaided eye. In addition, when it is considered that no dark adaptation is needed with the image intensifier, the improvement of visibility is even greater.

Appendix—Image Contrast of Square-Wave Gratings

In a 100% contrast square-wave grating, the light passes through the white lines without significant attenuation; no light passes through the black lines. When this pattern is imaged by an optical system, such as glass optics or an image intensifier, the image contrast or contrast transfer C_i is given by

$$C_i = \frac{B_w - B_b}{B_w + B_b}, \qquad [5]$$

where B_w and B_b are the luminance of the image of white and black lines, respectively.

The sum of B_w plus B_b, the denominator of Eq. [5], is essentially constant for all spatial frequencies because the contrast loss is caused by the light spread from the white lines into the black lines. If B_w and B_b are expressed as a fraction of the luminance of the white line at zero spatial frequency and the luminance of the white line at zero spatial frequency is unity, the following equation holds for all spatial frequencies:

$$B_w + B_b = 1, \text{ or } B_b = 1 - B_w. \qquad [6]$$

In the image of a less than 100-percent contrast pattern light diffuses from both the white lines and the black lines into adjacent lines. If the fraction of light transmission of a black line is denoted by x, Eq. [6] can be modified to give the partial luminance of the image of a white line resulting from light diffusion from a black line as $x(1 - B_w) = xB_b$. The partial luminance of the image of the white line is B_w. The total luminance of the image of a white line is the sum of the partial luminance, namely $B_w + xB_b$. Similarly, the luminance of the image of the black line is $B_b + xB_w$. The image contrast C then becomes:

$$C = \frac{B_w + xB - (B_b + xB_w)}{B_w + xB + B_b + xB_w} = \frac{B_w - B_b}{B_w + B_b} \frac{1-x}{1+x} = C_i C_f \qquad [7]$$

where C_f is the contrast of the square-wave gratings (field contrast).

References:

[1] I. P. Csorba, "Resolution Limitations of Electromagnetically Focused Image-Intensifier Tubes," **RCA Review,** Vol. 30, No. 1, p. 36, 1969.

[2] H. R. Blackwell, "Contrast Thresholds of the Human Eye," **J. Optical Soc. America,** Vol. 36, No. 11, Nov. 1946.

[3] Albert Rose, "The Sensitivity Performance of the Human Eye on an Absolute Scale," **J. Optical Soc. America,** Vol. 38, No. 2, Feb. 1948.

[4] O. H. Schade, Sr., "Optical and Photoelectric Analog of the Eye," **J. Optical Soc. America,** Vol. 46, No. 9, Sept. 1956.

[5] H. A. W. Schober and R. Hilz, "Contrast Sensitivity of the Human Eye for Square-Wave Gratings," **J. Optical Soc. America,** Vol. 55, No. 9, Sept. 1965.

[6] G. A. Morton, "Image Intensifiers and the Scotoscope," **Applied Optics,** Vol. 3, No. 6, June 1964.

[7] P. Schagen, "Electronic Aids to Night Vision," **Televison Sociey J.,** Vol. 10, No. 7, 1963.

[8] E. A. Richards, "Fundamental Limitations in the Low Light-Level Performance of Direct-View Image-Intensifier Systems," **Infrared Physics,** Pergamon Press, London, U.K., Vol. 8, p. 101, 1968.

A Technique for Selective Electroless Plating

N. Feldstein and T. S. Lancsek, RCA Laboratories, Princeton, N. J.

Abstract—A technique for the selective electroless plating of metals and their alloys on dielectric substrates is described. The deposited metal film is confined to the exposed surface of the substrate. This newly developed technique is based upon the selective deactivation of the adsorbed stannous layer above specially patterned films. The deactivation is achieved through chemical oxidation of the tin (II) to the tin (IV) state.

Introduction

Selective electroless plating of metals may be defined as the deposition of metals on preselected areas of a given substrate. There is a growing need for such processes, especially in the electronic industry, since they lead to inexpensive techniques for the fabrication of semiconductor devices, metal arrays, and printed circuitry. Selective electroless plating also lends itself to the forming of precision metal parts and thus eliminates typical problems of undercutting commonly observed in etch-down processes. Furthermore, through selective plating, problems of metal reclamation and etch disposal are greatly minimized.

To electrolessly plate on dielectric substrates, it is generally necessary to provide a catalytic surface capable of initiating deposition. Although there are several possible methods[1] for providing the requisite catalyst, the following two-step sequence is by far the most commonly employed. The substrate to be plated is immersed in an acidic stannous chloride solution, rinsed in water, dipped into an acidic palladium chloride solution and then rinsed again.

The following are believed to be the main physical and chemical reactions taking place during the sequence:

1. Sensitization through stannous adsorption

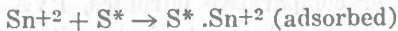

$$Sn^{+2} + S^* \rightarrow S^*.Sn^{+2} \text{ (adsorbed)}$$

2. Activation through a chemical replacement

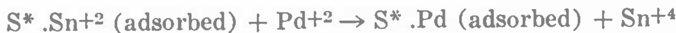

$$S^*.Sn^{+2} \text{ (adsorbed)} + Pd^{+2} \rightarrow S^*.Pd \text{ (adsorbed)} + Sn^{+4}$$

where S* is the surface site on dielectric surfaces. Although the detailed structure of the adsorbed stannous layer is not well understood, evidence exists that freshly deposited layers consist of a hydrated stannous oxide[2,3] phase (which forms in alkaline media) as well as a stannic oxide phase.[3]

The net result of this sequence[4] is the formation of finely divided (approximately 50 Å in diameter) catalytic palladium nuclei giving a surface with an island-type structure. The average "thickness" of the palladium layer is less than that for a monatomic surface layer. It is the physical presence and chemical activity of the palladium that is a prerequisite for the initiation of the electroless plating process.

To achieve selectivity in the subsequent deposition of a metal layer by electroless plating, various methods for providing patterns of catalytic nuclei are used. Although several techniques[5] for selective electroless plating have been recently surveyed, the one described in this paper provides for selective plating by the use of specially prepared films which deactivate the adsorbed sensitizing layer.

Experimental Procedures

Fig. 1 shows the main steps used in the current process. Typical 2 × 2 inch glass slides (E. Leitz, Inc., No. 19821) were used as substrates. At the conclusion of Step 1 (Fig. 1), an organic film pattern is present on the surface. Typical patterning materials used were dichromate sensitized PVA photoresists. This choice of photoresist was made because of the low cost, its ability to be developed in aqueous media, and its compatibility with the fillers used.

The composition of the resist was standard except for the added oxidizing agent. A typical formulation contains 95 cc of 4% PVA resist (DuPont Evanol PVA 50-42), 7 cc of 5% $Na_2Cr_2O_7$, and 2.7 cc saturated $KMnO_4$ solution. Methyl orange[6] was another oxidizing agent successfully used. The methyl orange was first dissolved in methanol then added to the resist to a final concentration of 0.015M.

After application of the resist it was found that a pre-exposure baking step (100°C) rendered the film insensitive to standard exposure and development techniques; however, by omitting this baking step it was found that normal processing could be carried out in order to produce the desired pattern. For comparative purposes, PVA resist without the above filler was used, as well as a typical positive resist, Shipley AZ-1350.

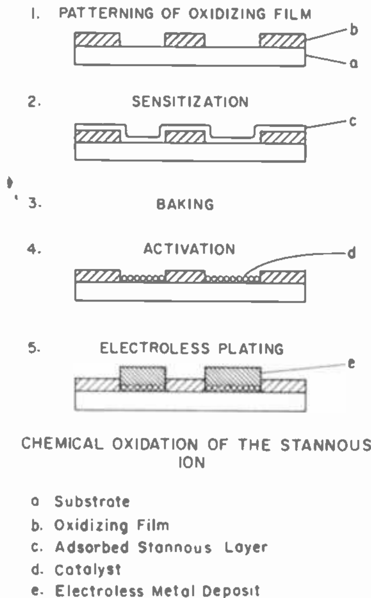

Fig. 1—Steps used in electroless plating process described here.

After patterning, a sensitization step is carried out (Fig. 1, Step 2). A typical sensitizing solution consisted of 14M HCl and 1.25M Sn^{+2}. After a ten-second immersion and rinsing in D.I. water, the substrate was spun dry, and then baked.

The baking procedure was generally varied depending on line-width requirements. Following a brief baking step, a standard activation in acidic palladium chloride is carried out (Fig. 1, Step 4). Electroless plating on the active regions takes place next. For convenience, a room temperature Ni-P[7] bath was selected. In contrast to most selective electroless plating techniques, the success of the current technique is attained by the selective chemical deactivation of the adsorbed stannous film following the sensitization step. Depending upon the resolution

requirement, a wide variety of films and methods of application may be used. The choice of photoresist type material was based primarily on microelectronic requirements. Although the baking temperature was kept constant at 165°C (this temperature corresponds to the surface temperature of the hotplate used for baking), the baking time had to be varied depending upon the line-width requirements. A typical trend in baking time and line width is shown in Table 1.

Table 1—Line Width and Baking Time

Line Width (mils)	Baking Time (min)
2-10	~1
~20	1.5-2
⋝40	3.0-5

Although the baking temperature in Table 1 was 165°C, it should be realized that a longer bake time at lower baking temperatures can give equivalent results. This alternative may be of practical significance in providing a more controllable baking cycle. Due to the relationship between line width and baking time, the present technique is not applicable where lines of different widths are present.

When a positive resist, AZ-1350, was used without fillers, even though good wetting was achieved, no inhibition of plating was obtained. Use of PVA dichromate resist without a filler proved to be borderline; that is, a pattern was apparent but the definition was poor. This is an expected result in that the dichromatic sensitizer of the photoresist is a good oxidizing agent for the stannous ion) and any free dichromate ion can produce the same results as a permanganate ion, that is oxidize the sensitized layer. The relatively poor definition is also explainable because of the small amount of dichromate on the surface of the resist following exposure compared to the much larger amount of permanganate in the earlier resist mixture.

The current process, however, offers certain advantages over other selective plating techniques.[5]

1. The electroless plating step follows immediately after the palladium activator step. This ensures the maintenance of a fresh catalytic layer and no possible contamination or removal of the catalytic sites by contact with organic films.
2. The current method is reproducible in comparison with a selective process that utilizes a differential wetting characteristic. In

the latter technique, because of a combination of effects, such as aging and impurities, nonwettable substrates may become wettable.

3. In the current method, inexpensive water soluble photoresists are employed successfully.

4. If the substrate is improperly processed, e.g., baked for too long or too short a time, the nickel plating may be etched away in a 50% HNO_3 solution. The sensitization process may then be repeated as for an unplated pattern. This sequence may be repeated several times before the photoresist begins to degrade and become plateable everywhere.

References:

[1] W. Goldie, **Metallic Coating of Plastics**, Electrochemical Publication, Ltd., 1968, Middlesex, England, Vol. I, Chap. 5.

[2] J. D. Donaldson and W. Moser, "Hydrous Tin (II) Oxide," **Jour. Chem. Soc.**, Vol. 117, p. 835, 1961.

[3] R. Sard, **Jour. Electrochem. Soc.**, Vol. 117, p. 864, 1970.

[4] J. P. Morton and M. Schlesinger, "The Nucleation, Growth, and Structure of Thin Ni-P Films," **Jour. Electrochem. Soc.**, Vol. 115, p. 16, 1968.

[5] N. Feldstein, "Selective Electroless Plating Techniques: A Survey," **Plating**, Vol. 57, No. 8, p. 803, 1970.

[6] G. P. Haight, Jr., "The Tin(II)-methyl Orange Reaction," **Jour. Chem. Ed.**, Vol. 22, p. 478, 1965.

[7] N. Feldstein, "Two Room-Temperature Electroless Nickel Plating Baths," **RCA Review**, Vol. 31, p. 317, June 1970.

The Ad-Conductor Cathode

Karl G. Hernqvist, RCA Laboratories, Princeton, N.J.

Abstract—A novel type of cathode construction suitable for an electron emitter in a glow or arc discharge is described. The cathode consists of a thick coating of alumina particles made conductive by adsorbed alkali metal atoms. A metallic conductor is embedded in the coating and attached to the cathode terminal. This cathode retains the sputter resistive properties of oxidized aluminum without the need for critical processing procedures. The alkali metal is continuously transportable within the coating and gives it a characteristic self-healing feature.

The "ad-conductor effect," by which adsorbed alkali metal atoms cause surface conductance in insulator substrates is reviewed, and an expression is derived for the conductance of a coating of alumina particles activated by cesium. Experimental studies of the electrical conduction through such a coating are described. Studies of the ad-conductor cathode in a neon glow discharge indicated a cathode fall of about 100 volts. The construction of ad-conductor cathodes suitable for gas lasers is described, together with tests using the cathode in helium-neon lasers and in pulsed argon lasers.

Introduction

For normal glow discharges, the most important electron emission mechanism is that due to ion bombardment of the cathode.[1] For pure metal cathodes, ion energies of the order of a hundred or hundreds of volts are required for substantial electron emission. Associated with this type of ion bombardment is release of atoms from the cathode (sputtering) causing several undesirable effects—gas clean-up, contamination of nearby structures, and, in severe cases, complete disintegration of the cathode itself. One method to relieve this problem is to use oxidized metal cathodes, as, for instance, oxidized aluminum[2] or tantalum,[3] because some oxides have lower sputtering yield than metals. Since most oxides are insulators, it is essential that the oxide layer be very thin and uniform, which generally requires rather laborious processing methods.[2] This paper describes a type of oxide

cathode consisting of a very thick porous coating of oxide deposited on a metal surface. The oxide is made conductive by the action of an alkali metal.[4] The alkali metal is subject to sputtering, but, due to the cataphoretic effects in the discharge, metal atoms return to the cathode. The conduction of the oxide is achieved by the adsorption of the alkali metal atoms on individual oxide particles of the coating. Hence, the term "ad-conductor cathode" will be used for this system.

This paper describes (1) the electrical properties of the ad-conductor cathode (2) studies of the ad-conductor cathode in a glow discharge, and (3) applications to gas lasers.

The Ad-Conductor Effect

It is well known that insulators such as, e.g., aluminum oxide, become conductive in the presence of alkali metal vapors such as cesium.[4,5] Their conductivity depends on the fractional coverage of adsorbed metal atoms on the oxide.[6] In equilibrium, this coverage is determined by the balance between arrival rate and desorption rate of metal atoms. Hence, it depends on the metal vapor density as well as on the temperature of the substrate (T_s). When a large supply of metal vapor atoms is present (pool) it is customary to express the vapor density in terms of the coldest temperature (T_p) of the enclosure (pool temperature). For each substrate material the fractional coverage of adsorbed metal atoms is a function of both T_s and T_p.

It has been proposed[4] that the conductivity caused by cesium on insulators is caused by electrons donated by the adsorbed atoms to the substrate. These electrons may contribute to the conductivity of the insulator in a layer adjacent to the surface. The experimental results for the surface conductivity are well represented by the relation[4]

$$\log_{10} g_{\square} = A - \frac{B}{T_s} + \frac{C}{T_p}, \qquad [1]$$

where $g_{\square}$ is the conductivity per square (in units of mhos) and A, B, and C are constants that depend on the kind of alkali-metal–substrate combination used. The constants A, B, and C are also affected by the contaminants present.

Conduction Through a Porous Coating

Assume an experimental arrangement where a porous coating of spherical alumina particles is positioned between two metal contacts,

of length a, width b, and separation L. It will be assumed that a binder is present in the coating to assure a substantial contact area between the particles, but that each particle surface communicates freely with the alkali metal vapor assumed to surround the coating. In this case, the coating may be approximately treated as a collection of closely packed cylindrical rods bridging the two metal contacts as shown in Fig. 1. If the diameter d of the particles is small compared to the

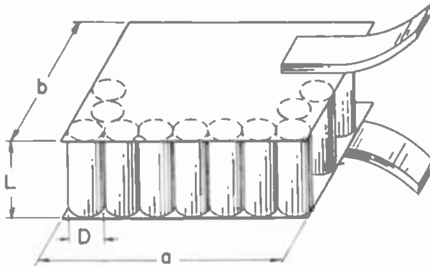

Fig. 1—Diagram showing closely packed insulating rods between two conducting planes.

extent of the electrodes ($d \ll a$ or b), the conductance between the two electrodes becomes

$$g = g_{\square} \frac{2\pi}{\sqrt{3}} \frac{ab}{Ld} \text{ mhos} \qquad [2]$$

For example, for cesium on aluminum oxide under "unclean" conditions[4] (sealed-off glass envelope), $A = -4.5$, $B = 2400$, and $C = 2700$. For the case where both the coating and the cesium pool are at room temperature ($T_p = T_s = 300°K$), $g = 11.5$ mhos for $ab = 1$ cm^2, $L = 1$ mm, and the particle size $d = 10$ microns. Thus, it is seen that the ad-conductor effect may provide a low conductance to a relatively thick insulator coating.

Since, according to Eq. [1], the conductivity per square is dependent on the temperature of the substrate, the conductance of the porous coating will be significantly affected by the joule heat developed at higher current densities. It can be shown theoretically that there exists a current density above which a run-away process takes place and most of the alkali metal is driven off the coating. This critical current density depends strongly on the experimental conditions prevailing.

Experimental studies of an ad-conductor coating were made using the test tube shown in Fig. 2. A coating of alumina particles 5 to 15 microns in diameter was deposited between two electrodes, one being a mesh allowing rapid communication with the vapor phase of cesium metal introduced into the tube. The coating covered a 1 cm^2 area and was 1 mm thick. The particles were suspended in a solution of aluminum nitrate, methanol, and water.

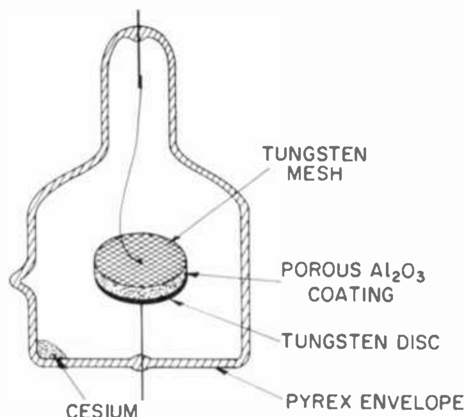

Fig. 2—Tube for testing porous ad-conductor.

After evacuation, the test vessel was baked at 400°C for five hours. Before exposure to cesium vapor, the alumina coating was white and exhibited a very high resistance. After introduction of cesium to the evacuated chamber, the color of the coating changed gradually from white to purple, to light blue, and finally to dark blue. Simultaneously, the conductance increased reaching a value of about 3 mhos after about 24 hrs. This value is in reasonable agreement with the value of 11.5 mhos for the idealized coating of Fig. 1. If sufficient heat is applied to the coating or if the cesium pool temperature is lowered by refrigeration, the color and conductance changes are reversed.

The current-carrying capability of the coating was demonstrated by applying constant currents of different magnitude to the coating. Fig. 3 shows recorder traces of voltage across the coating versus time for different currents. At low current, very little change occurs in the conductance over several hours. At intermediate currents, a noticeable change in conductance takes place, but a stable value is eventually reached. Finally, for currents in excess of about 1 A, a run-away condition takes place. In Fig. 3, the recovery towards equilibrium conductance is demonstrated by suddenly lowering the current to a value much lower than the critical current.

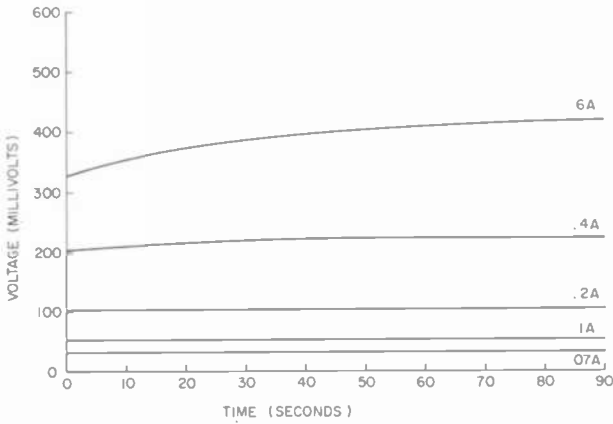

(a)

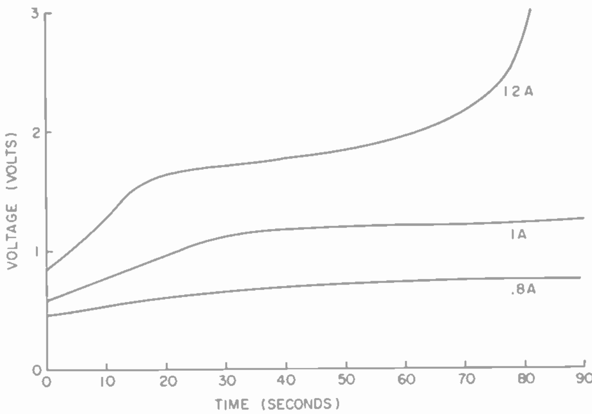

(b)

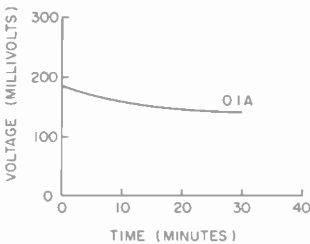

(c)

Fig. 3—Voltage across ad-conductor as a function of time for applied constant current: (a) steady-state conditions, (b) run-away effects at currents in excess of about 1 A and (c) recovery after severe joule-heating of ad-conductor. Parameter is the value of applied constant current.

Studies of the Ad-Conductor Cathode in a Glow Discharge

A test diode was made in order to study the properties of the porous ad-conductor coating as an emitter in a glow discharge. The cathode electrode was completely covered with 1 mm thick coating and activated by cesium, as described in the previous section. The cathode area was 4 cm^2 and the vessel was filled with neon at a pressure of 9 Torr. The *V-I* characteristic is shown in Fig. 4. The tube drop (mainly cathode fall) was about 100 volt, intermediate between that reported for aluminum and for alkali metals in neon vapor.[7]

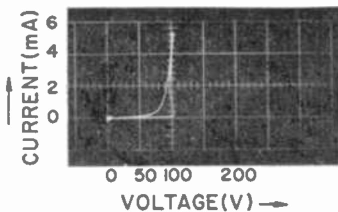

Fig. 4—V-I characteristic of glow discharge using ad-conductor cathode.

Stable long-time operation was demonstrated at normal current density ($j/p^2 \cong 6$ $\mu A/(cm^2 \times Torr^2)$). At higher current densities, overheating of the cathode would drive off the cesium making the cathode inoperative. After removal of the anode voltage for about ½ hour, self-healing took place and normal cathode operation could commence. No signs of sputtering were visible in the tube after 100 hours of operation at normal current densities.

For some applications, the presence of alkali metal may create a problem by causing a leakage path between electrodes (due to the ad-conductor effect, most insulators become conductive). This can be avoided by providing heating for the insulator surrounding the lead to the electrode that must be electrically isolated. This is automatically achieved in applications such as laser tubes where the anode is separated from the cathode by the capillary discharge, which heats up the capillary wall. Cataphoresis in the discharge tends to transport any alkali metal that may accidently have accumulated in capillary back to the cathode.

Fig. 5 shows the practical application of an ad-conductor cathode to a small He-Ne laser tube. The alumina coating is directly applied to the glass of the cathode bulb. The current-gathering tungsten wire is completely embedded in the coating, ensuring that no metal parts

are directly exposed to the discharge. The ceramic insert is heated up by the discharge and assures electrical isolation of the cathode from the glass tubes leading to the main laser bore. Since the cathode is heated by the discharge, it has been found advantageous to use potassium as an activator, since it has a somewhat lower vapor pressure than cesium. Processing and activation proceeded as for the glow discharge test tube described above, but the gas filling was that appropriate for a 1.5-mm-bore He-Ne laser (2 Torr He + 0.4 Torr Ne). No change in laser performance was noted after 1000 hours of operation at a cathode current density of 200 $\mu A/cm^2$. Shelf life of several years has been demonstrated. Lasers using the ad-conductor cathode have been shown to be particularly stable and free of noise.[8]

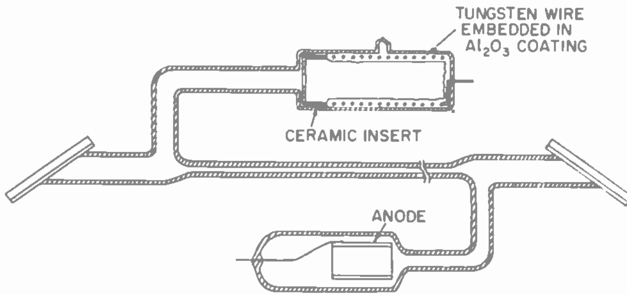

Fig. 5—Drawing showing laser tube using ad-conductor cathode.

Application of Ad-Conductor Cathode to a Pulsed Arc Discharge

It is well known that small emission centers may form on BaO-coated thermionic cathodes operating in gas discharge tubes. Such spots yield high-emission current densities but eventually lead to the permanent destruction of the cathode. It has been found that such emission centers may form on the cold ad-conductor cathode, but, due to the self-healing effect, no permanent cathode destruction occurs. The performance under such operating conditions has been studied in a pulsed argon laser, where pulse currents of the order of tens of amperes are required.

The construction and processing of the ad-conductor cathode for a pulsed argon laser is analogous to that of Fig. 5. The gas filling is that typical for argon lasers (~0.13 Torr for a 1-mm-diameter bore tube). To create cathode spots, the tube must be ignited by a fast rising high voltage pulse (typically 5 to 10 kV with ½ μsec rise time) preceding the main discharge pulse. Such pulse operation has been

demonstrated using pulse lengths from a few microseconds up to a few milliseconds,[8] at repetition rates from 1 to 60 Hz, and at pulse currents ranging from a few amperes up to a few hundred amperes with no signs of permanent cathode deterioration.

Details of the emission process are not known, but it may be due to local heating and resulting thermionic emission. A new emission center (bright yellow in appearance) appears to form for each pulse.

Conclusion

The ad-conductor cathode is a versatile electron emitter for gas discharge devices. The self-healing feature gives it a ruggedness and reliability suitable for lasers using noble gases.

Acknowledgment

The author wishes to express his appreciation to Dr. Jules D. Levine for many helpful discussions.

References:

[1] J. D. Cobine, **Gaseous Conductors,** pp. 113-115, Dover Press, New York, N.Y., 1958.

[2] U. Hochuli, P. Haldemann, and D. Hardwick, "Cold Cathodes for He-Ne Lasers," **IEEE J. Quantum Electronics,** Vol. QE-3, p. 612, Nov. 1967. See also R. E. Stark, "Progress on the Production Line," **Laser Focus,** Vol. 6, No. 8, p. 38, Aug. 1970.

[3] W. B. Bridges, and W. P. Kolb, "A Space Qualified He-Ne Laser," **IEEE J. Quantum Electronics,** Vol. QE-5, p. 363, June 1969.

[4] J. D. Levine. "Adsorption of Cesium on Insulators," NASA Report CR-349, Washington, D.C., Dec. 1965.

[5] T. I. Kamins, "Electrical Properties of Cesium Adsorbed on Insulating Substrates," **J. Appl. Phys.,** Vol. 39, p. 4536, Sept. 1968.

[6] J. D. Levine, "Electrical Conductivity of 0-2 Monolayers of Cesium on Sapphire at 77°K," **J. Appl. Phys.,** Vol. 37, p. 2175, April 1966.

[7] Ref. [1], pp. 217-218.

[8] K. G. Hernqvist, "Low Radiation Noise He-Ne Laser," **RCA Rev.,** Vol. 30, p. 429, Sept. 1969.

[9] K. G. Hernqvist, "Long Pulse Operation of Argon Lasers," **Applied Optics,** Vol. 9, p. 2247, Oct. 1970.

Permanent Holograms in Glass by RF Sputter Etching

J. J. Hanak, RCA Laboratories, Princeton, N. J.
J. P. Russell, Laboratories RCA, Ltd., Zurich, Switzerland

Abstract—Holograms have been reproduced for the first time in glass by the use of the rf sputter-etching technique. The procedure consists of first developing a hologram in Shipley photoresist coated on glass and then etching off the photoresist by rf sputtering. Because of the relatively constant rate of removal of the photoresist over the entire surface, followed by similar etching of the glass, the details of the hologram pattern can be transferred into the glass. Hologram efficiencies of 10-15% have been obtained. Holograms have been also etched into metals; however, dense, amorphous substances appear to be definitely superior media. The intended use of such holograms is for replicating them into plastic media, which has been satisfactorily accomplished.

Introduction

Holograms recorded in permanent media such as metals are desirable for replicating such holograms into softer media such as plastics. Such holograms are normally made by plating metals onto the surface of developed photoresist holograms and then peeling off the plated metal.

This paper deals with recording of holograms into glasses and a variety of other desirable hard durable materials. Glasses are dimensionally more stable than metals from the standpoint of hardness, plastic deformation, thermal expansion coefficient, and corrosion; in addition, they are transparent. This new development has been realized through the application of an rf sputter etching technique, which is known to be useful in controlled etching of almost any solid substance, including metals, glasses, ceramics, and plastics. In the usual sputter-etching procedure, a mask, usually photoresist, is placed over the object to be etched; the desired pattern is etched in the object through the opening in the mask to approximately the same depth everywhere. A hologram is, however, very different from such a pat-

tern in that it is a much more complicated pattern and is three dimensional rather than two dimensional. In addition, the detail of the pattern of a hologram (one micron or less everywhere) is much finer than that of any other pattern previously etched. The detail and its smooth variation must be preserved during the etching procedure.

Fabrication Procedure

Selected hard objects (such as glasses) in which it is desired to record the hologram are first coated with a uniform thickness of photoresist film which should be as thin as possible. In this case, Shipley photoresist having a thickness of 3000 to 5000 Å was used. The resist was baked for 10 min at 80°C prior to the exposure of the hologram by means of laser light.

Several exposures were made with varying exposure times (from 20 to 240 seconds) so that, upon the development of the resist, the holographic record would be imprinted into the resist to various depths. For the shortest exposures, the holograms in the resist were barely discernible, whereas for the longest exposures, removal of the resist down to the glass surface was evident. After the development, the resist was normally baked again for 10 min at 80°C. At this point, the photoresist hologram was ready for rf etching. A schematic diagram of a cross section of such a hologram is shown in Fig. 1.

RF etching was accomplished by placing the glass (or other) substrate onto the rf cathode and then bombarding the photoresist surface with argon ions at 0.8 W/cm^2, argon gas pressure of 5 millitorr and for periods from 15 to 40 minutes. Since etching of the resist surface proceeds at a relatively constant rate at each point of the surface, the glass under the valleys in the hologram image (Fig. 1) is exposed first, whereupon it begins to be etched. By the time the crests of the resist image are removed, the hologram image has been etched into the glass; significantly, the three-dimensional definition has been preserved. The progression of the etching process is illustrated in Fig. 2. At the onset of glass etching a yellow orange glow appeared (apparently due to sodium) over the hologram surface. Etching was terminated either after no further changes in the glow appearance took place or after about 500 to 1000 Å of the glass was removed (as estimated from previously determined glass-etching rate).

The amplitude of the hologram image in the glass was smaller than that in the resist, because the etching rate of the glass is somewhat slower than that of the resist. Because the efficiency of a hologram

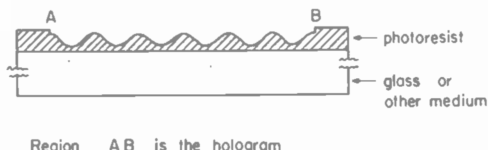

Fig. 1—Schematic diagram of a photoresist hologram ready for etching.

depends on the amplitude, it is desirable for the two rates to be equal or for the etching rate of the substrate to be greater than that of the resist. Since the sputtering rates of various glasses do not differ significantly (except for fused quartz, which etches about twice as fast as glasses), one must look at the possibility of varying the sputtering rate of resist. Qualitative results indicate that an increase in the baking time of the resist after development decreases its sputter etch rate until it nearly matches the etching rate of the glass. In this manner, an increase in the efficiency of the glass holograms can be obtained.

Discussion

The best glass holograms were obtained with long-exposure resist images where the resist image is only a few hundred Angströms thick. The thicker the resist image, the poorer the efficiency of the final glass hologram. Another factor is the depth to which the glass is etched. It would appear that the optimum end point for stopping the glass

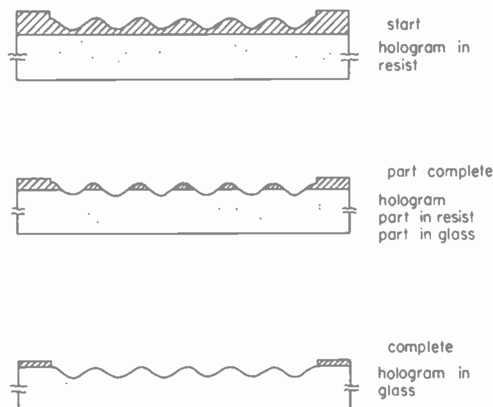

Fig. 2—The progression of the etching progress.

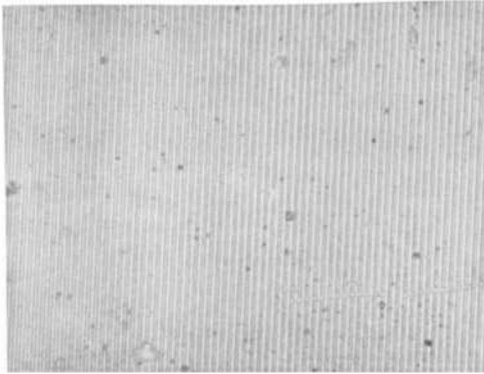

Fig. 3—Microphotograph of the resists hologram.

etching is just after the disappearance of the resist image. By terminating at this point, maximum hologram efficiency of 10-15% is realized in the glass as compared to the efficiency of 15-20% of the original resist hologram. Since the glass holograms were normally slightly overetched, the effect of overetching was examined. After etching an additional 2500 Å of glass from a hologram, a loss of less than half in efficiency was qualitatively observed; after 12,000 Å additional etching, the hologram retained about one tenth of its original efficiency. The remaining resist around the hologram was conveniently removed by rf etching in oxygen gas for two to three minutes.

In most of these experiments, ordinary slide glass was used, but any glass or ceramic material can be used, provided it is smooth and dense, (e.g., borosilicate glasses, silicate glasses, fused quartz, magnesium

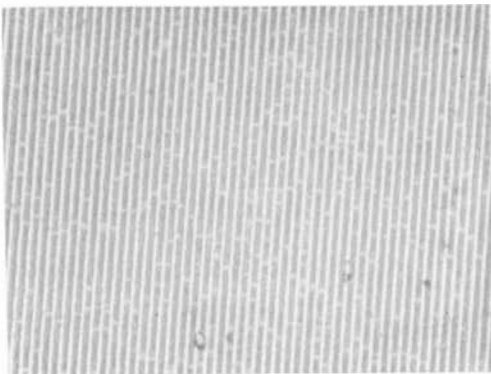

Fig. 4—Microphotograph of the glass hologram.

Fig. 5—Microphotograph of nickel hologram.

oxide, sapphire, or silicon). It was found that glasses, because of their amorphous and dense structure, reproduce very true images of the original resist. This can be seen by comparing the photomicrograph of the resist hologram image (Fig. 3) with that of the glass hologram image (Fig. 4).

Similar etching was attempted with smooth, sputtered nickel film deposited on glass. Although a pronounced hologram was obtained, the result was disappointing because the image was grainy due to small nickel crystallites in the film (Fig. 5). A hologram etched into bulk stainless steel was, in selected areas, better than that in the sputtered nickel; however, it contained many defects, such as pores, grain, and boundaries (see Fig. 6).

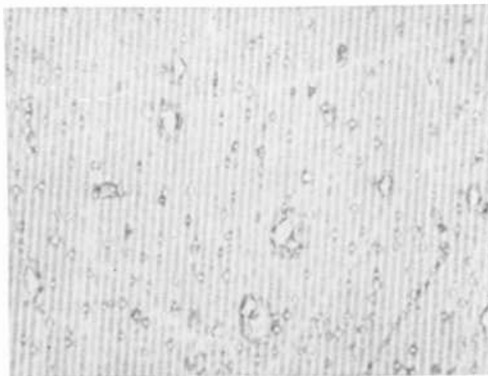

Fig. 6—Microphotograph of stainless steel hologram.

The holograms in glass, as well as the ones in metal, could be easily replicated into plastics such as Vinar or plastic adhesive tape, indicating their usefulness.

In summary, the preceding experiments on rf etching of holograms into glasses, although preliminary and qualitative in nature, yielded novel and surprisingly good holograms with efficiencies of 10 to 15%. This technique could be easily perfected by varying the treatment of the resist. It provides a completely permanent hologram in transparent media such as glass or in reflecting media such as metals.

The method is not restricted to holograms recorded in photoresist; any light-sensitive etchable medium that produces "relief" holograms or "thin" phase holograms, in which the regions of different refractive indices have different etching rates, can be used.

Acknowledgments

The authors wish to acknowledge H. Schutz and R. Widmer for their technical assistance.

RCA Technical Papers First Quarter, 1971

January

"Complex Indicated Angles Applied to Unresolved Radar Targets and Multipath," S. M. Sherman, **IEEE Trans. GAES**
"Fluctuating Target Detection in Clutter Using Sidelobe Blanking Logic," R. S. Johnson and Coauthors, **IEEE Trans. GAES**
"Phased-Array Radar Perspective," A. S. Robinson, **Microwave Jour.** (Guest Editorial)
"Radar Performance with Multipath Using the Complex Angle," L. Goldman, Jr. and Coauthor, **IEEE Trans. GAES**
"Signature Variations with Mirror Separation for Small Sealed CO_2 Lasers," A. L. Waksberg, J. C. Boag, and S. Sizgoric, **IEEE Jour. Quantum Electronics**
"Surface States of Electrons on Liquid Helium," R. Williams, R. S. Crandall, and A. H. Willis, **Phys. Rev. Letters** (4 January)
"EPR Studies of Photochromic CaF_2," C. H. Anderson and E. S. Sabisky, **Phys. Rev. B** (15 January)
"Theory of Photochromic Centers in CaF_2," R. C. Alig, **Phys. Rev. B** (15 January)
"Holographic Mass Memory's Promise: Megabits Accessible in Microseconds," R. D. Lohman, R. S. Mezrich, and W. C. Stewart, **Electronics** (January 18)

February

"Design Considerations of Hyperabrupt Varactor Diodes," P. J. Kannam, S. Ponczak, and J. A. Olmstead, **IEEE Trans. GED**
"Television Hum-Buckers," J. L. Hathaway, **Jour. SMPTE**
"Evidence for a First-Order Structural Transformation in Nb_3Sn," L. J. Vieland, R. W. Cohen, and W. Rehwald, **Phys. Rev. Letters** (15 February)
"Series Limiter Tracks Signal, Finds Symmetry," R. J. Turner, **Electronics** (Designer's Casebook) (February 15)

March

"Accurate Measurements of Isolation in Three-Port Circulators," R. L. Ernst, **RCA Review** (March)
"Analysis and Optimization of a Field-Emitter Array," J. D. Levine, **RCA Review**
"Anti-Parallel Pair of High-Efficiency Avalanche Diodes," H. Kawamoto and S. G. Liu, **Proc. IEEE** (Letters)
"A Comparative Analytical Study of the Performance of Argon Laser Amplifiers and Oscillators," I. Gorog, **RCA Review**
"Computer Calculation of Electron Trajectories in Television Camera Tubes," O. H. Schade, Sr., **RCA Review**
"Contrast Characteristics of X-Ray Images," I. P. Csorba, **RCA Review**
"Electromagnetic Reflection from an Extended Turbulent Medium: Cumulative Forward-Scatter Single-Backscatter Approximation," D. A. De Wolf, **IEEE Trans. GAP**
"Linear Distortion of the NTSC Color Television Signal," J. P. Bingham, **IEEE Trans. GBC**

"Low-Field Acoustoelectric Interaction and Thermal Brillouin Scattering," R. W. Smith, **Jour. Acous. Soc. Amer.** (Part 3)
"Microwave Amplification Using Transferred-Electron Devices in Prototype Filter Equalization Networks," B. S. Perlman, **RCA Review**
"MOS Models and Circuit Stimulation," J. E. Meyer, **RCA Review**
"A New Type of Gallium Arsenide Field-Effect Phototransistor," G. A. Swartz, A. Gonzalez, and A. Dreeben, **RCA Review**
"Noise in Laser Recording," R. F. Kenville, **IEEE Spectrum**
"Performance Comparison of TV Transmitter RF Demodulators and the Home Receivers," W. L. Behrend, **IEEE Trans. GBC**
"Radiochemical Study of Semiconductor Surface Contamination III. Deposition of Trace Impurities on Germanium and Gallium Arsenide," W. Kern, **RCA Review**
"A Refined Step-Recovery Technique for Measuring Minority Carrier Lifetimes and Related Parameters in Asymmetric p-n Junction Diodes," R. H. Dean and C. J. Nuese, **IEEE Trans. GED**
"A Simplified Electrohydrodynamic Treatment of Threshold Effects in Nematic Liquid Crystals," G. H. Heilmeier, **Proc. IEEE** (Letters)
"Photoconductivity in Photochromic Strontium Titanate," R. Williams, **Jour. Appl. Phys.** (1 March)
"Dispersion Effects in Magnetostrictive Films," H. Kurlansik and L. Onyshkevych, **Jour. Appl. Phys.** (15 March)
"Excited State Exchange in MnF_2," S. Freeman, **Jour. Appl. Phys.** (15 March)
"NMR of $CuC_{2-x}V_xS_4$ Spinels," S. B. Berger, L. Darcy, and Coauthors, **Jour. Appl. Phys** (15 March)
"Spectral Dependence of the Photoconductance in $CdCr_2Se_4$," A. Amith and S. B. Berger, **Jour. Appl. Phys.** (15 March)
"X-Ray Study of the Debye-Waller Factor of Nb_3Sn," L. J. Vieland, **Phys. Rev. B** (15 March)
"Theory of Exponential Absorption Edges in Ionic and Covalent Solids," D. Redfield and Coauthor, **Phys. Rev. Letters** (29 March)

Patents Issued to RCA Inventors First Quarter 1971

JANUARY

R. W. Ahrons Self-Correcting Shift Counter (3,555,249)
J. K. Allen Automatic Degaussing Circuit for TV Having Half-Wave Voltage Doubler Power Supply (3,555,343)
D. R. Andrews Picture Projection with Sound (3,554,637)
A. J. Banks Video Signal Switching Step Suppressor (3,558,815)
D. C. Bussard Pulse Width Modulated Solid State Regulated Power Supply (3,559,-030)
P. S. Carnt Switching Mode Control Circuits (3,553,357)
M. Caulton, R. D. DeStefano, and S. P. Knight Process for Manufacturing Micro-miniature Electrical Component Mounting Assemblies (3,554,821)
J. E. Croy Bi-Directional Shift Register (3,555,433)
F. C. Easter Microsensing Network (3,553,500)
R. W. Etter Methods for Electroless Plating and for Brazing (3,551,997)
A. Fischer, Jr. Process for Handling and Mounting Semiconductor Dice (3,554,832)
G. W. Gray Vehicle Road Guidance System (3,556,244)
D. F. Griepentrog Kinescope Bias Tracking Circuits (3,555,175)
D. F. Griepentrog Plural Operating Mode Automatic Gain Control System (3,555,182)
J. R. Hall and P. B. Korda Agitation Sensitive Alarm Circuit (3,559,203)
F. C. Hassett RFI-Protected Flip-Flop (3,553,485)
F. P. Heiman and P. H. Robinson Method of Treating Semiconductor Devices to Improve Lifetime (3,556,880)
W. A. Helbig and W. L. Ross Multiple Channel Display System (3,555,520)
R. C. Heuner and J. Litus, Jr. Integrated Circuit Having Bonding Pads Over Unused Active Area Components (3,558,992)
K. C. Hudson Optical Compensating Filter with Selective Radial Absorption Distribution (3,558,208)
J. B. Jones De-Soldering Apparatus (3,557,430)
Z. J. Kiss Photochromic Light Valve (3,552,824)
N. R. Landry Elimination of Mode Spikes in Microwave Ferrite Phase Shifters (3,555,460)
W. H. Liederbach and L. Pessel Metallization of Titanate Wafers (3,554,796)
C. E. Lilley Color Tube Having Ground Plane Between Focus Electrodes and Screen Grids (3,558,954)
A. L. Limberg Electrical Circuits (3,555,309)
S. G. Liu and K. K. N. Chang Bulk Semiconductor Light Radiating Device (3,558,-889)
C. L. Lundvall, II Method of Mounting a Heater in a Tubular Cathode (3,555,640)
E. E. Mayaud Method for Producing a Graphic Image (3,558,310)
A. Mayer Method of Treating Semiconductor Devices (3,556,879)
R. A. Minet Beam Landing Error Control Apparatus for Magnetically Focussed Cathode Ray Tubes (3,558,953)
J. F. Monahan and R. A. Dischert Matrixing Apparatus (3,558,806)
J. M. S. Neilson Semiconductor Rectifiers Having Controlled Storage and Recovery Characteristics (3,553,536)
E. L. Nelson Recording Transducer Selection Limiter (3,555,518)
H. J. Prager, S. Weisbrod, and K. K. N. Chang High Power, High Efficiency Silicon Avalanche Diode UHF and L Band Oscillator (3,559,097)
J. C. Rester and C. D. Brudos Multiplex Synchronizing Circuit (3,555,195)
S. A. Riciti Electro-Optical Composition System (3,553,676)
H. C. Schindler Superconductive Magnet Construction (3,559,127)
E. W. Schlieben Sailing Vessel (3,556,035)
E. R. Schrader Superconductive Magnet and Method of Constructing Same (3,559,-130)
S. L. Starger Lead Assembly Structure for Semiconductor Devices (3,553,828)
T. Szirtes Antenna Comprising Restraining Means for Resilient Support Members (3,553,731)
A. Waxman and K. H. Zaininger Plasma Anodizing Aluminum Coatings on a Semiconductor (3,556,966)

FEBRUARY

R. W. Ahrons Memory Protecting Circuit (3,562,555)
J. Avins Television Integrated I. F. Amplifier Circuits (3,564,125)
R. A. Bonnette and N. L. Lindburg Display Device Including a Point Image (3,564,-325)
M. G. Brown, Jr. Adhesive Mounting Means for a Cathode Ray Tube-Yoke Combination (3,566,321)
F. Caprari Solid State Regulated Power Supply for Intermittent Loads with Plural Charging Paths for a Capacitor (3,560,842)
H. N. Crooks and R. L. Hallows, Jr. Electronic Photocopy System (3,564,130)
P. Foldes Feed System (3,560,976)
D. W. Hall, II Feedback Type Oscillator with Input Stabilizing Means (3,562,669)
D. W. Hall, II Servo System Including Differential and Unbalance Amplifiers (3,566,-295)
G. D. Hanchett Integral Pulse Switching Systems (RE 27072)
J. R. Harford Direct Coupled AM Detector (3,560,865)
K. G. Hernqvist and J. R. Fendley, Jr. Gaseous Electric Discharge Tube Including a Plurality of Puncturable Gas Storage Cells (3,560,789)
E. W. Herold and K. H. Fishbeck Spatially Modulated Halftone Dot Image Generation System (3,564,131)
C. R. Horton Tape Lifter (3,564,158)
R. N. Hurst Sync Regenerator (3,564,141)
S. L. Knanishu High Input Impedance Amplifier (3,564,436)
H. Kressel and F. Z. Hawrylo Fabricating Semiconductor Devices (3,560,275)
R. D. Larrabee Microwave Oscillator Including Two Bulk Negative Resistance Devices in a Three-Terminal Cavity (3,562,665)
A. L. Limberg Signal Translating Circuit Having First and Second Pairs of Semiconductor Devices with Matching Conduction Characteristics (3,564,438)
A. T. Ling Multi-Processor/Multi-Programmed Computer System (3,566,357)
A. Macovski Optical Reduction of Luminance to Chrominance Crosstalk in Color Television Cameras (3,566,013)
A. Macovski Color Television Camera Encoding System (3,566,016)
A. Macovski Television Color Difference Signal Encoding System (3,566,017)
A. Macovski Color Television Signal Generating System (3,566,018)
H. L. May Shadow Mask Type Color Picture Tube with a Fine Mesh Flexible Particle Shield Between the Gun and Target Portions (3,560,779)
H. S. Miiller and R. J. Linhardt Transcendental Function Generator (3,562,714)
L. S. Napoli and J. J. Hughes Directional Filter Comprising a Resonant Loop Coupled to a Transmission Line Pair (3,560,887)
H. Nelson Depositing Successive Epitaxial Semiconductive Layers from the Liquid Phase (3,565,702)
R. G. Olden and H. C. Gillespie Electrostatic Charging Appartus with Means to Blow Electrostatic Charge onto a Photoconductive Surface from a Remotely Located Corona Generator (3,566,110)
M. H. Polhemus Television Receiver or Similar Article (D219886)
A. K. Rapp P-MOS Multivibrator (3,562,559)
R. J. Satriano Semiconductor Device (3,562,404)
A. N. Schmitz Coaxial Transmission Line (3,564,108)
H. G. Seer, Jr. Current Regulator Utilizing a Floating Reference Voltage Supply (3,566,246)
J. M. Shaw Electroetching of a Conductive Film on an Insulating Substrate (3,560,-357)
C. V. Srinivasan Correction of Block Errors in a Transmission of Data (3,562,709)
G. W. Taylor and A. R. Sass Light Deflection System (3,566,172)
J. P. Watson Discontinuity Detector (3,566,084)
P. K. Weimer Integrated Display Panel Utilizing Field-Effect Transistors (3,564,135)
C. P. Wen Surface Strip Transmission Line and Microwave Devices Using Same (3,560,893)

MARCH

R. Amantea, H. W. Becke, and P. J. Del Priore Double Heat Sink Semiconductor Device (3,569,798)
J. D. Ammerman Corner Edge Connector for Printed Circuit Boards (3,567,998)
J. Avins Signal Translating System Providing Amplification and Limiting (3,569,740)
L. J. Baun Automatic Video Signal Gain Controlling Apparatus (3,569,620)
R. S. Berger Semiconductor Mounting Adapter (3,568,761)
P. S. Carnt and T. E. Bart Monitoring of PAL Signal Wafeforms (3,567,862)
G. F. Carroll Automatic Return-to-Center Deflection Circuit (3,569,773)
R. F. Day Electronic Photocomposition System (3,568,178)
R. L. Ernst Temperature-Compensated Frequency-Voltage Linearizing Circuit (3,-569,867)
H. Esten Gas Environment for Recorder-Reproducer Systems (3,569,637)
P. Foldes Feed System (3,569,870)
H. C. Gillespie, R. Herman, and M. M. Sowiak Apparatus for Monitoring and Controlling the Concentration of Toner in a Developer Mix (3,572,551)
W. E. Harbaugh Heat Pipe (3,568,762)
A. Harel Vacuum Evaporation Apparatus (3,572,672)
G. V. Jacoby and J. D. Gleitman Compensation Readback Circuit (3,568,174)
Z. J. Kiss Photochromic Device Based upon Photon Absorption (3,572,941)
J. M. Kresock Color Subcarrier Oscillators (3,569,613)
W. H. Laznovsky Selective Anodization Apparatus and Process (3,573,176)
E. D. Menkes Phase Lock Loop (3,571,743)
R. G. Olden Apparatus for Developing Electrostatic Images (3,572,922)
K. Suzuki and R. Hirota Nonreciprocal Microwave Devices Using a Semiconductor Element (3,569,868)
J. P. Watson Reduction of Tape Stiction (3,568,907)
D. A. Wisner Speed Control for Motor Vehicles (3,570,622)

Juan J. Amodei received his B.S. degree in Electrical Engineering from Case Institute of Technology in 1956 and his M.S.E.E. from the University of Pennsylvania in 1961. In 1965, he returned to the University of Pennsylvania for further study and received his Ph.D. degree from that institution in 1968. Dr. Amodei began his career in 1956 with the Philco Corporation, where he worked on transistor radio developments. In 1957, he joined the Advanced Development Department of RCA's Industrial Electronic Products Division in Camden, N.J. Here he had responsibility for the development of a high-accuracy analog-to-digital converter, the development of a novel pressure telemetering system for medical applications, and a sampling oscilloscope system with 1/3-ns rise time that later became a product. He transferred to RCA Laboratories, Princeton, N.J., in 1959, working on the development of high-speed computer circuits and subsystems. The results of this work included the realization of shift registers capable of 100 and 200 megabits/second information transfer rates and binary full adder systems with fraction-of-a-nanosecond state delays. He later became engaged in research and development of integrated circuits. Since 1966, he has been engaged in research and development of materials and devices for optical information storage. The work included research on the optical storage properties of doped and pure $SrTiO_3$ crystals, leading to quantitative models that explained the thermal and optical coloring behavior of these materials. This work also led to the discovery and understanding of two-photon induced coloration effects. Later he was actively engaged in research and development in the field of optical recording in magneto-optic and metallic thin films as well as other approaches to optical information storage. In 1967, he studied and developed a model for electron migration effects in photochromic materials that led to the proposal of an electro-optic holographic storage device. He is presently the project scientist in a program aimed at developing better materials and techniques for high sensitivity, erasure resistant electro-optic storage systems.

Since 1962, Dr. Amodei has been a lecturer at LaSalle College in Philadelphia, where he has been Chairman of the Electronic Physics Department of the Evening Division since 1967. Dr. Amodei is a member of the American Physical Society, the IEEE, and Eta Kappa Nu.

I. P. Csorba graduated from the Electrical Engineering Fundamentals at the Electrical Engineering Faculty of the Technical University of Budapest in 1952. In the same year he was admitted to the Communication Engineering Faculty, specializing in communication and electronics. In October, 1954, he received the Diplom Ingenieur Degree in Electrical and Communication Engineering. From 1955 to 1956 he worked as a research engineer at the War Technical Institute, Budapest. In December of 1956 he joined the research group of Rauland Corporation, Chicago, where he worked on electrostatic-type image converter tubes, television picture tubes, scan-converter tubes. From 1959 to 1961 he was with Motorola, Inc., Chicago, working primarily on electrostatic-type scan magnification. In November of 1961, he joined RCA as a member of the Photo and Image Tube Engineering Activity. Mr. Csorba has been active in the design and development of magnetic and electrostatic-type image tubes and photomultiplier tubes.

William G. Einthoven studied at the T. H. of Delft (Delft Technical University) in the Netherlands, and passed his propodeuse examination in 1950. He prepared the scientific material for the expedition of Prof. A. C. S. van Heel to the Isle of Gotland in Sweden for the eclipse of the sun in 1954 for his candidate work and accompanied his tutor on the expedition to this eclipse. In 1955 he received his degree in physical engineering on the subject "Striae of the Suneclipse of 1954". Mr. Einthoven joined the N. V. Werkspoor in Amsterdam in 1957 where he worked in the laboratory for physical and dynamical research. He built and ran a test set for oil bearings for fast turbines and solved practical problems on heat transfer, thermodynamics of the diesel process, and on vibrations of crank shafts in diesel engines. In 1959, Mr. Einthoven joined the semiconductor development laboratory of N. V. Philips in Nymegan, the Netherlands. He developed the first local series of SCR's. He discovered a method to develop high-voltage transistors operating at up to 2,000 V. He headed several development groups, ranging from 2 to 12 people. In 1967, Mr. Einthoven joined the RCA Laboratories in Somerville, N. J. He is currently working on the development of high-current-density transistors.

Mr. Einthoven is a member of the IEEE and the Dutch "Koninklyk Institunt van Ingenieurs".

Nathan Feldstein attended The City College of New York where he received a Bachelor of Chemical Engineering degree. Following graduation, he was employed by Corning Glass Works in Corning, New York, as a development engineer in the Ceramic Division. While in the Army, he served as an instructor in the School of Chemical, Biological, and Radiological Warfare in the Panama Canal Zone. While pursuing graduate work in Physical Chemistry at New York University, Dr. Feldstein was a teaching fellow at the same school, and later a lecturer in the Department of Chemistry of Brooklyn College. He joined the staff of RCA Laboratories in January 1966. His research activity has been primarily concerned with research and development of electrolytic and electroless plating solutions for applications in the electronics industry.

Dr. Feldstein is a current member of A.C.S., E.C.S., A.E.S., Phi Lambda Upsilon, and Sigma Xi.

Edward C. Giaimo, Jr. received his B.S.E. degree with Honors in Engineering from Princeton University and an M.S.E. from the same University. He subsequently studied Solid State Electronics at Princeton. From 1943-46 he served with the United States Navy, completed the United States Navy Radio Material Program and was assigned to the Naval Research Laboratory, Washington, D.C. In 1951 he joined RCA Laboratories where he made contributions to ruggedization of precision traveling-wave-tube helix structures, developed apparatus for the purification and testing of early semiconductor materials used for transistors, has made original contributions in many aspects of the Electrofax process and materials and related electrophotographic systems. From 1957 to 1959 he was a member of the technical staff of C-Stellarator Associates, an organization of RCA and Allis Chalmers engineers, charged with the task of designing and building a thermonuclear research reactor for fusion research at the Matterhorn Project, Princeton University. His staff engineering duties with this organization included system specification and coordination.

Mr. Giaimo is a member of the American Association for the Advancement of Science, Sigma Xi and a Senior Member of the IEEE.

Joseph J. Hanak received his B.S. in Chemistry at Manhattan College in 1953, his M.S. in Physical Chemistry at the University of Detroit in 1956 and his Ph.D. in Physical Chemistry at the Iowa State University in 1959. He was a Teaching Fellow in Chemistry at the University of Detroit in 1953 and 1954, worked for the Ethyl Corporation as a Chemist in 1955, and was a research assistant at the AEC Institute for Atomic Research (Ames, Iowa) from 1955 to 1959. He has been a Member of The Technical Staff at RCA Laboratories since 1959. Dr. Hanak has been active in the field of chemistry, metallurgy, and crystallography of the rare-earth elements. He had done research on superconducting materials and ferrites as well as on the processes of chemical vapor deposition and sputtering. He is the inventor of the RCA vapor-deposition process of Nb_3Sn, and of stable, permanent, high-field superconducting magnets. For the past three years he has worked in the field of rf sputtering of superconductors and dielectrics. He introduced novel co-sputtering compositional analysis and testing methods applicable to a large variety of materials, thereby greatly increasing productivity in materials research. In 1969-70, he spent a year at RCA Laboratories, Ltd., Zurich, Switzerland on a European Research Fellowship.

Dr. Hanak is a member of the American Chemical Society, Phi Lambda Upsilon, and Sigma Xi.

Karl G. Hernqvist graduated in Electrical Engineering at the Royal Institute of Technology, Stockholm, Sweden, in 1945. He received the Licentiate of Technology degree in 1951 and the Doctor of Technology degree in 1959. From 1946 to 1952 he was employed by the Research Institute of National Defense in Stockholm, working in the field of microwave electronics. From 1948 to 1949, Dr. Hernqvist was a trainee of the American-Scandinavian Foundation at RCA Laboratories, to which he returned in 1952; he is presently working on gas lasers. Dr. Hernqvist is a Member of the Institute of Eletcrical and Electronics Engineers and Sigma Xi.

Peter Kannam received the B.S. and M.S. Degrees in physics from Madras University, India, in 1955 and the Ph.D. degree in phsics from Pennsylvania State University, University Park, in 1961. From 1956 to 1960 he worked on nuclear spectroscopy at Pennsylvania State University. In 1960 he joined Westinghouse Testing Reactor where he was engaged in nuclear reactor design. From 1962 to 1969 he worked on the design and the development of high-power and high-frequency semiconductor devices at Westinghouse Semiconductor Division, Youngwood, Pa. Some of the major projects undertaken during this period were on peak-power capability of high-speed transistors, current-crowding in high-frequency power transistors, effects of free carriers on collector multiplication, and stress distribution silicon power devices. He was also on the faculty of Seton Hill College, Greensburg, Pa., as Associate Professor of Physics and Mathematics from 1961-1969. In 1969, he joined RCA Electronic Components, Somerville, N. J., where he engaged in the design and development of microwave devices. His present activity includes the development of power integrated circuits, investigation of burst noise in integrated circuits, and computer-aided device design.

Dr. Kannam is a member of the American Physical Society and the American Association of Physics Teachers.

Thomas S. Lancsek attended Moravian College in Bethlehem, Pennsylvania, where he received a B.S. in Chemistry in 1969. He joined RCA Laboratories in June 1969 and has been primarily involved with research and development of electrolytic and electroless plating solutions for applications in the electronics industry.

John Olmstead received the B.S. degree in electrical engineering from the University of Buffalo, Buffalo, N. Y., in 1952, and the M.S. degree in electrical engineering from Newark College of Engineering, Newark, N. J., in 1957. He has taken graduate courses in mathematics and physics at the University of Buffalo. Mr. Olmstead joined RCA in 1952, working on gaseous discharge devices at the Princeton, N. J., Laboratories. He joined the Electron Tube Division, Harrison, N. J., in 1954, where he worked on design and development of gas-filled and other specialized industrial tubes. Between 1950 and 1960 he alternated assignments at RCA and the University of Buffalo, where he was an Assistant Professor of Electrical Engineering. He returned to RCA on a full-time basis in 1960, joining the Solid-State Division, where he worked on GaAs solar cells, p-n junction field-effect devices, high-frequency power bipolar transistors, and MOS field-effect transistors. He is responsible for the multiple-gate "cascade" MOS configuration and the multi-emitter concept basic to the RCA "overlay" transistor technique. In 1965 he undertook the development of high-voltage power transistors for horizontal-deflection applications. In this area, he analyzed and demonstrated that the degradation in the saturation characteristics of such devices is due to base widening. Since 1967 he has been engaged in device passivation studies (Si_3N_4, Al_2O_3) and the development of p-i-n and varactor diodes. Presently he is an Engineering Leader in the Technology Center at RCA, Somerville, N. J. Mr. Olmstead is a member of Sigma Xi.

Samuel Ponczak received his B.S. degree in Electrical Engineering from the University of Maryland in 1957. After graduation he joined RCA in Somerville, N. J., where he has been engaged in computer-aided transistor design. He has also been involved in research work on p-i-n and varactor diodes. He is presently working towards the M.S. degree in Electronics at the Stevens Institute of Technology.

Mr. Ponczak is a member of IEEE, Eta Kappa Nu, and Tau Beta Pi.

J. P. Russell received the B.Sc. degree in Physics from Queens University Belfast in 1958, and the degree of D.Phil from Oxford University in 1962. In 1963 he joined the Royal Radar Establishment in England where he worked for four years on light scattering with lasers. He joined Laboratories RCA Zurich in 1967 and has since been engaged in research on holography.

Richard A. Sunshine received the B.S. degree (with Honor) in Physics from Stevens Institute of Technology in 1964, the M.A. degree from Princeton University in 1967, and the Ph.D. degree in Solid State Device Physics from Princeton University in January 1971. In 1964 he joined RCA Laboratories where he investigated ionic motion in thermally grown silicon-dioxide films. He received an RCA Laboratories Graduate Study Award for part-time study of Physics at Rutgers University from 1964-1966, and a Doctoral Study Award for full time study of Device Physics at Princeton in 1967. His Doctoral dissertation was primarily concerned with the development of new optical techniques for studying failure mechanisms in semiconductor devices, and the application of these techniques to the study of second breakdown in avalanching silicon-on-sapphire diodes. In addition, he has done theoretical work on Gunn domains, and on space-charge effects in avalanching junctions.

Dr. Sunshine is a member of Tau Beta Pi.

J. L. Vossen joined RCA in 1958 after receiving a B.S. in physics from St. Joseph's College. He was first associated with the Microelectronics Department of the RCA Solid-State Division in Somerville, N. J. There, his work centered on thick- and thin-film passive component processes. In 1962, Mr. Vossen transferred to the Advanced Communications Laboratory of the Defense Communications Systems Division in New York City, where he led a group conducting research on precision thin film resistors and capacitors. In 1965 he joined the Process Research and Development Laboratory of the RCA Laboratories in Princeton, N. J., where he has been engaged in research on sputtering processes and other physical methods of film deposition.

Mr. Vossen is a member of the American Physical Society, the American Vacuum Society, the Electrochemical Society and Sigma Xi.

Paul K. Weimer received his A.B. degree from Manchester College in 1936, his M.A. degree in physics from the University of Kansas in 1938, and his Ph.D. degree in physics from Ohio State University in 1942. From 1937 to 1939, he taught physics and mathematics at Tabor College, Hillsboro, Kansas. Since 1942, Dr. Weimer has been engaged in research at RCA Laboratories, Princeton, N. J., where he is a Fellow, Technical Staff, and Head of Solid-State-Scanned Device Research. At RCA Laboratories he has participated in the basic development of various types of television tubes and solid-state devices. From 1959 to 1960, Dr. Weimer was granted an RCA fellowship for study abroad, which was spent at the Laboratoire de Physique, Ecole Normale Superieure, Paris, France, working in the field of semiconductors. He was recipient of a Television Broadcasters' Award in 1946, the IRE Vladimir K. Zworykin Television Prize in 1959, and the 1966 IEEE Morris N. Liebmann Prize Award. In 1968, Dr. Weimer was awarded an honorary degree of Doctor of Science by Manchester College. He is a Fellow of the Institute of Electrical Engineers and a member of the American Physical Society.

Cheng P. Wen received the B.S. and M.S. degrees in electrical engineering from the University of Michigan, Ann Arbor, Michigan, in 1956 and 1957 respectively. From 1956 to 1963, he was employed in the Electron Physics Laboratory of the University and received the Ph.D. degree in electrical engineering in 1963. In March 1963, he joined the RCA Laboratories at Princeton, New Jersey, where he has worked on ultra-low-noise microwave tubes, gas lasers, microwave integrated circuits.

Dr. Wen is a member of Eta Kappa Nu, Tau Beta Pi and Sigma Xi.

C. Frank Wheatley started work on point-contact transistors with RCA immediately after receiving his BSEE from the University of Maryland in 1951. At RCA, he has worked on the design, production, application, and development of germanium and silicon semiconductor devices. A large portion of his time has also been directed toward high-voltage and high-power devices. Mr. Wheatley has made extensive contributions in the design of transistor auto radios, solid-state high-fidelity circuits, and solid-state television deflection circuits. Mr. Wheatley is a Senior Member of IEEE.

Harry Wielicki, a chemistry graduate of the Philadelphia College of Pharmacy and Science, is a Member of the Technical Staff at RCA Laboratories, David Sarnoff Research Center, Princeton, N. J. Throughout most of his career at RCA, he has been engaged in research and development of electrophotographic coatings and developers for the conventional applications of the process as well as special uses, such as photoengraved printing plates and color Electrofax. He is a member of the American Chemical Society.